Doctoral theses at NTNU, 2024:78

Ask Lysne

# Steam reforming of biomass gasification tar impurities with Ni-Co/Mg(Al)O catalysts

## Experimental studies using model tar components

Doctoral thesis

NTNU
Norwegian University of Science and Technology
Thesis for the Degree of
Philosophiae Doctor
Faculty of Natural Sciences
Department of Chemical Engineering

NTNU
Norwegian University of
Science and Technology

Ask Lysne

# Steam reforming of biomass gasification tar impurities with Ni-Co/Mg(Al)O catalysts

## Experimental studies using model tar components

Thesis for the Degree of Philosophiae Doctor

Trondheim, March 2024

Norwegian University of Science and Technology
Faculty of Natural Sciences
Department of Chemical Engineering

NTNU
Norwegian University of
Science and Technology

**NTNU**
Norwegian University of Science and Technology

Thesis for the Degree of Philosophiae Doctor

Faculty of Natural Sciences
Department of Chemical Engineering



ISBN 978-82-326-7750-4 (printed ver.)
ISBN 978-82-326-7749-8 (electronic ver.)
ISSN 1503-8181 (printed ver.)
ISSN 2703-8084 (online ver.)

Doctoral theses at NTNU, 2024:78

Printed by NTNU Grafisk senter

# Abstract

Hydrotalcite-derived Ni-Co/Mg(Al)O catalysts with a range of different Ni-Co ratios, Ni+Co loading, calcination temperatures and noble metal promotion (Pt/Pd/Rh) were prepared, targeting low-coking steam reforming of biomass gasification tar impurities. Fresh catalysts were characterised by XRD, ICP-MS, XRF, $N_2$-physisorption, $H_2$-chemisorption and TPR. All catalysts were tested through experimental studies with model tar components. The effects of key operating parameters, including temperature, steam concentration, tar loading and model tar composition, were additionally investigated. The benefits of the bi-metallic Ni-Co/Mg(Al)O catalyst was demonstrated, with intermediate Ni-Co ratios providing a suitable compromise between coke formation resistance associated with low Ni-Co ratios and the higher initial activity of high Ni-Co ratio catalysts. Post-run coke characterisation by TGA-TPO-MS, Raman spectroscopy and STEM/EDS contribute to the understanding of the highly attractive resistance towards deactivation by coke formation associated with Ni-Co catalysts.

A coke classification system (based on characteristic TPO-MS coke combustion temperatures) was proposed, including soft coke A (undeveloped surface carbon), hard coke B1.1 (initial scattered carbon filaments), B1.2 (strongly deactivating metal particle encapsulating coke), B2 (carbon filament clusters and fused filaments) and B3 (strongly deactivating bulk encapsulating coke). Critical low-temperature (around 650 °C) and tar loading limits (below 20 g/$Nm^3$) were identified, below/above which rapid deactivation by coke formation was observed (20-20 wt% Ni-Co sample). Noble metal promotion was shown to enhance bio-syngas *in situ* activation performance (with Rh > Pt > Pd), but did not considerably affect deactivation by coke formation. A critical Ni+Co loading limit was found (above 30 wt% Ni+Co), below which high dispersion metal particles were obtained. Strong deactivation by high-coordination active site tar inhibition and coke formation effects were observed with the high-dispersion samples. High-temperature calcination (800 °C) was found to reduce the strong deactivation effects associated with small-diameter metal particles, proposed to result from increasing coke and/or coke precursor gasification rates assisted by Mg(Al)O support basic sites.

The potential of the Switch-SRCG (cyclic steam reforming and coke gasification) dual-bed design was demonstrated, reducing overall coke deposition with both Ni and Ni-Co catalysts. The concept provides continuous on-stream catalyst regeneration by coke gasification, representing a novel approach to net low-coking biomass gasification tar reforming.

# Preface

This thesis is submitted to the Norwegian University of Science and Technology (NTNU) for partial fulfilment of the requirements for the degree of philosophiae doctor (PhD).

The presented work was carried out at the Department of Chemical Engineering at NTNU, Trondheim, with Professor Edd A. Blekkan as main supervisor and Kumar R. Rout as co-supervisor.

The project was funded by the Norwegian Research Council (project number: 257622) through the Centre for Environment-friendly Energy Research (FME) Bio4Fuels. The Norwegian Research Council is also acknowledged for the support to the Norwegian Micro- and Nano-Fabrication Facility, NorFab (project number: 295864).

# Acknowledgements

I would like to thank my supervisor Prof. Edd A. Blekkan for his excellent guidance throughout this project. Thank you for making yourself available, supporting and challenging my ideas, and for always understanding that life in the lab comes with both good and bad days. My co-supervisor Dr. Kumar R. Rout is also acknowledged for his contributions to the project. Thank you to master student Kristin, Rémi, Ida and Emma for their efforts in the lab. Thank you to my previous office mate PhD candidate Jibin Antony for sharing his great experience with STEM/EDS, and for his supporting presence in the office. All engineers and technical support in the Catalysis group and at Department of Chemical Engineering are acknowledged for their help throughout this work. Especially, head engineer Dr. Estelle Marie M. Vanhaecke is acknowledged for her tremendous support. Thank you for making space in your busy schedule for our daily struggles.

All friends in the Catalysis group are greatly appreciated for your help and emotional support whenever I came to you with challenges and questions. Thank you for putting a smile on my face during lunch and by the coffee machine. All friends outside work are also highly appreciated. Thank you for listening to all my ups and downs throughout my PhD journey, and for making me forget work challenges from time to time.

Finally, I am very grateful for the everyday support from my family, parents, brothers, their partners and children. Especially, my wife Astrid, my son Magnus, and my soon to be born second son are highly treasured. Thank you for filling my life with joy and laughter, for making me work hard to go home, and for always supporting me in good times and in bad.

# List of publications

Paper I Lysne, A.; Madsen, K. Ø.; Antony, J.; Rout, K. R.; Blekkan, E. A., Effects of Ni-Co Ratio on Deactivation and Coke Formation in Steam Reforming of Hydrocarbon Impurities from Biomass Gasification with Ni-Co/Mg(Al)O Catalysts, *Chem. Eng. Trans.* **2022**, 92, 37-42.

Paper II Lysne, A.; Saxrud, I.; Madsen, K. Ø.; Blekkan, E. A., Steam reforming of bio-syngas tar impurities with Ni-Co/Mg(Al)O catalysts - Operating parameter effects. Manuscript submitted to *Appl. Catal. B: Environ.* (2024).

Paper III Lysne, A.; Saxrud, I.; Snidaro, R. L. G.; Blekkan, E. A., Nobel metal (Pt, Pd and Rh) promoted Ni-Co/Mg(Al)O catalysts for steam reforming of biomass gasification tar impurities. Manuscript submitted to *J. Catal.* (2024).

Paper IV Lysne, A.; Blekkan, E. A., Continuous coke management with Ni and Ni-Co catalysts for bio-syngas tar steam reforming – The Switch-SRCG unit. Manuscript submitted to *Catal. Commun.* (2024).

# List of presentations

Lysne, A.; Rout, K. R.; Blekkan, E. A., *Catalytic Steam Reforming of Hydrocarbon Impurities from Biomass Gasification*, Bio4Fuls Days: Working towards a climate-neutral 2050, November 18-19, **2020**, online seminar. Oral presentation.

Lysne, A.; Rout, K. R.; Blekkan, E. A., *Steam Reforming of Hydrocarbon Impurities from Biomass Gasification with Ni-Co/Mg(Al)O Catalysts*, Bio4Fuls Days, November 17-18, **2021**, Drammen, Norway. Poster presentation.

Lysne, A.; Madsen, K. Ø.; Antony, J.; Rout, K. R.; Blekkan, E. A., *Deactivation and Coke Formation in Steam Reforming of Hydrocarbon Impurities from Biomass Gasification with Ni-Co/Mg(Al)O Catalysts*, International Conference on Biomass (IConBM2022), June 5-8, **2022**, Naples, Italy. Oral presentation.

Lysne, A.; Madsen, K. Ø.; Antony, J.; Rout, K. R.; Blekkan, E. A., *Deactivation and Coke Formation in Steam Reforming of Hydrocarbon Impurities from Biomass Gasification with Ni-Co/Mg(Al)O Catalysts*, Bio4Fuels Days, November 16-17, **2022**, Lindås, Norway. Oral presentation.

Lysne, A.; Madsen, K. Ø.; Antony, J.; Rout, K. R.; Blekkan, E. A., *Hydrotalcite-Derived Nickel-Cobalt Catalysts for Steam Reforming of Bio-Syngas Hydrocarbon Impurities*, Norwegian Catalysis Symposium, December 1-2, **2022**, Stavanger, Norway. Oral presentation.

Lysne, A.; Madsen, K. Ø.; Antony, J.; Rout, K. R.; Blekkan, E. A., *Hydrotalcite-Derived Nickel-Cobalt Catalysts for Steam Reforming of Bio-Syngas Hydrocarbon Impurities*, CATHEX/iCSI seminar, June 6-8, **2023**, Trondheim, Norway. Poster presentation.

Lysne, A.; Saxrud, I.; Madsen, K. Ø.; Blekkan, E. A., *Steam Reforming of Bio-Syngas Hydrocarbon Impurities with Ni-Co/Mg(Al)O Catalysts - Operating Parameter Effects*, 15th European Congress on Catalysis (EuropaCat 2023), August 27-September 1, **2023**, Prague, Czech Republic. Poster presentation.

Lysne, A.; Saxrud, I.; Madsen, K. Ø.; Blekkan, E. A., *Steam Reforming of Bio-Syngas Hydrocarbon Impurities with Ni-Co/Mg(Al)O Catalysts - Operating Parameter Effects*, 6th Doctoral Colloquium BIOENERGY (DOC2023), September 18-19, **2023**, Göttingen, Germany. Oral presentation.

Lysne, A.; Saxrud, I.; Madsen, K. Ø.; Blekkan, E. A., *Steam Reforming of Bio-Syngas Hydrocarbon Impurities with Ni-Co/Mg(Al)O Catalysts - Operating Parameter Effects*, Bio4Fuls Days: Technology Implementation, November 15-16, **2023**, Oslo, Norway. Poster presentation.

## Author's contribution

The author played an active role in all stages of the research presented in this thesis. The building of the experimental setup was planned and coordinated by the author. The candidate developed the experimental approach and preformed the experimental work and data analysis. The result interpretation was conducted in collaboration with co-authors. All manuscripts were written by the author and reviewed by co-authors.

The synthesis, fresh catalyst characterisation and activity tests reported in Paper I were performed in collaboration with master student Kristin Ø. Madsen. The synthesis, fresh catalyst characterisation and activity tests reported in Paper III were (partly) performed in collaboration with master student Ida Saxrud. Master student Rémi L. G. Snidaro also contributed to the fresh catalyst characterisation presented in Paper III. The STEM/EDS results were acquired in collaboration with PhD candidate Jibin Antony and master student Ida Saxrud. The ICP-MS was performed by SINTEF.

# List of abbreviations

| | |
|---|---|
| BET | Brunauer-Emmett-Teller |
| BJH | Barrett-Joyner-Halenda |
| BTL | Biomass-to-liquid |
| CCUS | Carbon capture, utilization and storage |
| CTL | Coal-to-liquid |
| DRM | Dry reforming of methane |
| DSS | Daily start-up and shut-down |
| EDS | Energy dispersive X-ray spectroscopy |
| EFG | Entrained flow gasifier |
| ESR | Ethanol steam reforming |
| ETIP | European Technology and Innovation Platform |
| FAME | Fatty acids and methyl esters |
| FBG | Fluidized bed gasifier |
| FGF | First generation feedstock |
| ER | Equivalence ratio |
| ESP | Electrostatic precipitators |
| EXAFS | Extended X-ray absorption fine structure |
| FID | Flame ionisation detector |
| FT | Fischer-Tropsch |
| FWHM | Full width at half maximum |
| GC | Gas chromatography |
| GHG | Greenhouse gas |
| GHSV | Gas hourly space velocity |
| GTL | Gas-to-liquid |
| HEFA | Hydroprocessed esters and fatty acids |
| HOB | Hot oxygen burner |
| HT-WGS | High-temperature water-gas shift |
| ICDD | International Centre for Diffraction Data |
| ICP-MS | Inductively coupled plasma mass spectrometry |
| IEA | International Energy Agency |
| LT-WGS | Low-temperature water-gas shift |
| MFC | Mass-flow controller |
| MS | Mass spectrometry |
| MSW | Municipal solid waste |
| NDC | Nationally determined contribution |
| NZE | Net-zero emission |
| OSER | Oxidative steam reforming of ethanol |
| PAH | Polycyclic aromatic hydrocarbons |

| | |
|---|---|
| PDF | Powder diffraction files |
| POX | Partial oxidation |
| RPS | Rotating particle separator |
| SAF | Sustainable aviation fuels |
| S/B | Steam-to-biomass ratio |
| S/C | Steam-to-carbon ratio |
| SECSG | Sorption enhanced catalytic steam gasification |
| SEM | Scanning electron microscope |
| SESMR | Sorption enhanced steam methane reforming |
| SESR | Sorption enhanced steam reforming |
| SESRE | Sorption enhanced steam reforming of ethanol |
| SESRG | Sorption enhanced steam reforming of glycerol |
| SEWGS | Sorption enhanced water-gas shift |
| SF | Stoichiometric factor |
| S/G | Steam-to-gas ratio |
| SGF | Second generation feedstock |
| SMR | Steam methane reforming |
| SNG | Synthetic natural gas |
| SRCG | Steam reforming and coke gasification |
| STEM | Scanning transmission electron microscopy |
| STP | Standard temperature and pressure |
| TCD | Thermal conductivity detector |
| TGA | Thermogravimetric analysis |
| TOF | Turnover frequency |
| TPD | Temperature-programmed desorption |
| TPO | Temperature-programmed oxidation |
| TPR | Temperature-programmed reduction |
| TRI | ThermoChem Recovery International |
| TWV | Three-way valve |
| UHT-WGS | Ultra-high-temperature water-gas shift |
| WGS | Water-gas shift |
| WMO | World Meteorological Organization |
| WTL | Waste-to-liquid |
| XRD | X-ray diffraction |
| XRF | X-ray fluoresence |

# List of symbols

| | |
|---|---|
| $a_m$ | Atomic surface area ($H_2$-chemisorption) |
| Bo | Bodenstein number |
| c | BET constant |
| Ca | Carberry number |
| $C_{CH4}$ | $CH_4$ concentration |
| $C_{CH4,b}$ | Bulk $CH_4$ concentration |
| $C_{CH4,s}$ | Surface $CH_4$ concentration |
| $C_{CH4,o}$ | Inlet $CH_4$ concentration |
| D | Mean crystallite domain size (XRD) |
| d | Interplanar spacing (XRD) |
| $D_{CH4,eff}$ | Effective $CH_4$ pore diffusivity |
| $D_{CH4,k}$ | $CH_4$ Knudsen diffusivity |
| $D_{CH4,m}$ | Molecular $CH_4$ bulk diffusivity |
| $D_m$ | Active metal dispersion ($H_2$-chemisorption) |
| $d_m$ | Mean metal particle diameter ($H_2$-chemisorption) |
| $d_p$ | Catalyst particle diameter |
| $d_t$ | Reactor inner cross section diameter |
| $E_a$ | Activation energy |
| $F_n$ | Mole flow (compound n) |
| $F_{n,o}$ | Inlet mole flow (compound n) |
| $F_{tot}$ | Total mole flow |
| $h_b$ | Catalyst bed height |
| K | Scherrer constant (XRD) |
| k | Reaction rate constant |
| $k_g$ | External mass-transfer coefficient |
| m | Full width at half maximum (XRD) |
| $M_m$ | Molar mass |
| n | Order of reflection (XRD) |
| P | Adsorptive pressure (BET) |
| $P_o$ | Equilibrium pressure of condensed gas (BET) |
| $r_{CH4}$ | $CH_4$ reaction rate |
| $r_{CH4,v}$ | Volumetric $CH_4$ reaction rate |
| $r_{CH4,o}$ | Inlet $CH_4$ reaction rate |
| Re | Reynolds number |
| $R^2$ | Coefficient of determination (regression analysis) |
| Sc | Schmidt number |
| SF | Stoichiometric factor ($H_2$-chemisorption) |
| Sh | Sherwood number |

| | |
|---|---|
| TOF | Turnover frequency |
| $u_o$ | Superficial gas velocity |
| v | Adsorbed volume (BET) |
| $V_m$ | Mono-layer adsorption volume ($H_2$-chemisorption) |
| $v_m$ | Bulk metal atomic volume ($H_2$-chemisorption) |
| $v_m$ | Mono-layer adsorption volume (BET) |
| $V_{STP}$ | Standard ideal gas molar volume ($H_2$-chemisorption) |
| W | Catalyst mass |
| $w_m$ | Active metal weight fraction |
| $X_{CH4}$ | $CH_4$ conversion |
| $x_n$ | Mole fraction (compound n) |
| $X_{tar}$ | Tar conversion |
| $\alpha$ | Reaction order |
| $\Delta C$ | Carbon mass balance |
| $\Delta H°$ | Standard enthalpy of reaction |
| $\varepsilon_b$ | Catalyst bed porosity |
| $\varepsilon_p$ | Catalyst particle porosity |
| $\eta$ | Effectiveness factor (internal mass-transfer) |
| $\lambda$ | Wavelength of incident X-rays (XRD) |
| $\mu_g$ | Gas phase dynamic viscosity |
| $\Phi$ | Weisz-modulus (internal mass-transfer) |
| $\phi$ | Thiele-modulus (internal mass-transfer) |
| $\rho_g$ | Gas phase density |
| $\tau_b$ | Catalyst bed tortuosity |
| $\tau_p$ | Catalyst pore tortuosity |
| $\theta$ | Diffraction angle (XRD) |

# Contents

**Abstract** i

**Preface** iii

**Acknowledgements** v

**List of publications** vi

**List of presentations** vii

**Author's contribution** viii

**List of abbreviations** x

**List of symbols** xii

**Contents** xiv

**1 Introduction** 1
- 1.1 Liquid biofuels in NZE scenario . . . 1
- 1.2 Scientific objectives . . . 2
- 1.3 Thesis outline . . . 3

**2 Literature review** 5
- 2.1 Bio-FT technology . . . 5
  - 2.1.1 Biomass gasification . . . 6
  - 2.1.2 Tar impurities . . . 13
  - 2.1.3 Fischer-Tropsch requirements . . . 14
  - 2.1.4 Commercialisation status . . . 15
- 2.2 Bio-syngas conditioning . . . 20
  - 2.2.1 $H_2$/CO ratio adjustment . . . 20
  - 2.2.2 Tar elimination strategies . . . 21
- 2.3 Ni-based steam reforming catalysts . . . 21
  - 2.3.1 Deactivation by coke formation . . . 22
  - 2.3.2 Hydrotalcite-based Ni-Co catalysts . . . 23
  - 2.3.3 Noble metal promotion . . . 26

**3 Methodology** 29
- 3.1 Catalyst preparation . . . 29
- 3.2 Catalyst characterisation . . . 30

3.2.1 XRD . . . 30
3.2.2 XRF . . . 31
3.2.3 ICP-MS . . . 31
3.2.4 $N_2$-physisorption . . . 31
3.2.5 $H_2$-chemisorption . . . 32
3.2.6 TPR . . . 33
3.3 Catalyst testing . . . 33
3.3.1 Experimental setup . . . 33
3.3.2 Steam reforming experiments . . . 37
3.3.3 Regeneration experiments . . . 37
3.3.4 Condenser sample analysis . . . 38
3.3.5 Calculations . . . 38
3.3.6 Thermodynamic equilibrium . . . 40
3.3.7 Empty-reactor tests . . . 40
3.3.8 Carbon mass balance . . . 41
3.3.9 Mass-transfer limitations . . . 42
3.4 Coke characterisation . . . 46
3.4.1 Raman spectroscopy . . . 46
3.4.2 TGA-TPO-MS . . . 46
3.4.3 STEM/EDS . . . 47

**4 Summary of scientific investigations** **49**
4.1 Paper I: Ni-Co ratio effects . . . 49
4.2 Paper II: Key operating parameters . . . 50
4.3 Paper III: Noble metal promotion . . . 51
4.4 Paper IV: Switch-SRCG . . . 53

**5 Conclusion and future work** **55**

**References** **57**

**Appendix** **71**
A Paper I . . . 71
B Paper II . . . 79
C Paper III . . . 105
D Paper IV . . . 133

# 1 Introduction

The World Meteorological Organization (WMO) recently reported (2022) an all time high global average surface mole fraction of $CO_2$ (415.7 ppm, 149% of pre-industrial 1750 level) [1]. The continuously increasing greenhouse gas (GHG) levels point in the direction of a global climate crisis with current policy scenarios resulting in a global warming of 2.8 °C by 2100 [2]. The predicted temperature is reduced to 2.4 °C upon implementation of all unconditional and conditional nationally determined contributions (NDCs) reported before COP27 (27th United Nations Climate Change Conference of the Parties, 2022). Needless to say, immediate action is required in order to achieve the Paris Agreement temperature goal. The 1.5 °C scenario requires net-zero $CO_2$ emissions by 2050, with increasingly negative emissions in the following decades [3].

The necessary transformation of the global energy sector is outlined by the International Energy Agency (IEA) through the net-zero $CO_2$ emission by 2050 (NZE) scenario [4]. Low-emission liquid fuels are herein required for long-distance transportation where electrification cannot be easily or economically achieved. Such limitations on electric power applications relates to the superior energy density and recharging efficiency of liquid fuels [5]. The annual growth of terrestrial plants store more than three times the global energy demand, and biomass has been put forth as the most viable feedstock for renewable carbon-based liquid fuels [6].

## 1.1 Liquid biofuels in NZE scenario

The NZE scenario includes advanced liquid biofuels as bioethanol, biodiesel and biokerosene produced from second generation feedstocks (SGFs) [4]. This includes waste, residues and non-food cellulosic energy crops (grown on marginal/non-arable land). Such advanced biofuels should replace conventional bioethanol and biodiesel (FAME, fatty acid and methyl esters), produced from first generation feedstocks (FGFs), competing with food production. The NZE scenario relies on advanced biodiesel production by Fischer-Tropsch synthesis following biomass gasification (bio-FT) and HEFA (hydroprocessed esters and fatty acids) routs. The drop-in capabilities of liquid biofuels provides the advantage of continued utilisation of operating combustion engine technology [7]. This is included in the NZE scenario where production of advanced biofuels increase from 0.1 to 2.7 mboe/d (million barrels of oil equivalent per day) from 2020 to 2030, mostly to replace fossil fuels for passenger vehicles, light trucks and aviation [4].

After 2030, advanced biofuel production continues to increase, reaching 6.2 mboe/d by 2050. The application now shifts towards heavy-duty vehicles, shipping and aviation, as the electrification of passenger vehicles and light trucks advances. The NZE scenario herein rely on advanced biofuel production technologies like bio-FT to be able to rapidly shift product compositions from biodiesel to biokerosene. It is worth noting that around 50% of advanced biodiesel and biokerosene production should include carbon capture, utilization and storage (CCUS) by 2050 [4].

The rapid large-scale commercialisation of bio-FT technology face serious challenges in terms of efficiency and economic sustainability [8]. Integration of biomass gasification and Fischer-Tropsch technologies requires intermediate bio-syngas conditioning, effectively removing inorganic, organic and particulate contaminants [9]. The elimination of condensable aromatic hydrocarbon impurities (tars) has herein been put forth as the most cumbersome technical challenge [10]. Tar removal by catalytic steam reforming is generally considered a highly interesting approach, potentially increasing process efficiencies compared to physical separation and high-temperature thermal cracking strategies [11].

## 1.2 Scientific objectives

The goal of the PhD project was to contribute in the development of a suitable catalyst system for steam reforming of biomass gasification tars. The initial work focused on establishing an experimental approach for catalyst testing at relevant operating conditions. An experimental rig was designed and built for the purpose of model studies addressing catalyst reforming activity, stability and product selectivity ($H_2$/CO/$CO_2$). Initial testing focused on establishing a reliable approach in terms of operation at intrinsic kinetic conditions, stable reactant feed and product analysis control, and experimental repeatability. Recent reviews on tar steam reforming catalysts call upon further research on bi-metallic Ni-Co systems, targeting low-cost, high-performance alloy catalysts with increased resistance towards deactivation by coke formation [12]. The hydrotalcite-derived Ni-Co/Mg(Al)O catalyst was selected based on the high activity and reduced coke formation reported for other steam reforming systems in previous literature [13].

Paper I (Ni-Co ratio effects) presents the first testing of such Ni-Co/Mg(Al)O catalysts for steam reforming of biomass gasification tar at relevant operating conditions [14]. Post-run coke characterisation was included (Raman spectroscopy, TGA-TPO-MS and STEM/EDS), targeting a better understanding of coke morphology following bio-syngas tar steam reforming.

Paper II presents the results from further screening of key operating parameter effects (temperature, S/C ratio, model tar loading and tar composition), considering the intermediate Ni-Co ratio system. The approach was selected targeting the identification of critical operating parameter limits affecting catalyst deactivation by coke formation.

Paper III presents the first report on noble metal promoted (Pt, Pd and Rh) Ni-Co/Mg(Al)O catalysts for bio-syngas conditioning in a secondary reformer at relevant operating conditions. Noble metal promotion was selected considering previous reports on Pt-promoted Ni-Co/Mg(Al)O catalysts providing stable high conversion of hydrocarbon impurities during *in situ* sorption enhanced catalytic steam gasification (SECSG) [15]. Pt-doped Ni/Mg(Al)O catalysts have also been shown to provide *in situ* self-activation capabilities in daily start-up and shut-down (DSS) of steam methane reforming (SMR) [16]. Such properties are highly interesting also for steam reforming of biomass gasification tars, considering cyclic catalyst regeneration by coke combustion/gasification. The effects of Pt/Pd/Rh promotion on bio-syngas *in situ* activation were investigated in this work. The effects of Ni+Co loading and calcination temperature were additionally studied within the Ni-Co/Mg(Al)O catalyst system.

Paper IV demonstrates the viability of the Switch-SRCG dual-bed catalyst regeneration scheme (at model conditions). The first steam reforming (SR) bed effectively removes hydrocarbon impurities, providing clean bio-syngas for downstream catalyst regeneration by coke gasification (CG) in the second bed. The two catalyst beds switch between SR and CG operation assisted by two 4-port valves (see Appendix D, Figure 1).

## 1.3 Thesis outline

Chapter 2 includes literature background covering relevant technical implications and commercialisation status of bio-FT technology. The key tar elimination challenge in bio-syngas conditioning is further introduced. The status of Ni-based steam reforming catalysts is reviewed, focusing on low-coking bi-metallic Ni-Co systems, hydrotalcite-precursor effects and noble metal promotion. Chapter 3 presents the project methodology, including catalyst preparation and fresh catalyst characterisation techniques. The experimental setup applied for bio-syngas conditioning model studies is further described. The post-run coke characterisation approach is introduced. Chapter 4 provides a summary of the scientific results included in this work. Finally, Chapter 5 presents concluding remarks and recommendations for future work. All papers are provided in the Appendix A-D.

# 2 Literature review

## 2.1 Bio-FT technology

The long history of Fischer-Tropsch (FT) hydrocarbon synthesis dates back to the early experiments of invention around 1925 (Franz Fischer and Hans Tropsch, Kaiser Wilhelm Institute for Coal Research, Germany) [17]. The strategic advantage of the original coal-to-liquid (CTL) process led to a rapid development and commercialisation of FT technology, reaching an industrial CTL production capacity of 600.000 t/year around 1945. After World War II, further large-scale commercialisation of CTL technology was demonstrated through the construction of the FT plant Sasol 1 (Sasolburg, South Africa) in 1952 [18]. Two additional coal-based plants Sasol 2 (1976) and Sasol 3 (1983) were built in South Africa (Secunda) following the oil crisis in the early 1970s, with a production capacity of 160.000 bpd (mainly gasoline and diesel). The first natural gas-to-liquid (GTL) plants were built by PetroSA (Mossel Bay, South Africa) and Shell (Bintulu, Malaysia) in 1993. The Sasol 1 plant has also been adapted to the natural gas feedstock (2004). The largest GTL facility is today the Shell Pearl plant (Qatar), producing 140.000 bpd of GTL products [19], as well as 120.000 boe/d of liquefied petroleum gas (propane and butane) and ethane [18].

The successful adaptation of FT technology to GTL process schemes demonstrates the feedstock flexibility associated with the FT approach. Further development of biomass-to-liquid (BTL) and organic waste-to-liquid (WTL) technologies, integrating thermal gasification of biomass feedstocks and FT synthesis (bio-FT), have been suggested to provide a highly attractive scheme for the production of low-emission liquid biofuels and chemicals [20]. The bio-FT approach includes the considerable advantage of the utilisation of already available gasification and FT technology [21].

The typical bio-FT process scheme includes generation of syngas ($H_2$/CO) through biomass gasification, conditioning (cleaning, cooling and $H_2$/CO ratio adjustment), $H_2$/CO separation, FT synthesis, product recovery, separation and refining into useful product [21]. The commercialisation of bio-FT technology has herein been limited by the intermediate bio-syngas conditioning steps, requiring efficient removal of inorganic, organic and particulate contaminants [9]. The elimination of tar impurities (condensable hydrocarbons) has been put forth as the most cumbersome challenge [10].

It should be noted that the intermediate bio-syngas product additionally offers a range of alternative applications shown in Figure 2.1 [22]. This in-

cludes methanol synthesis (key intermediate in chemical industry) as well as $H_2$ and $NH_3$ production *via* water-gas shift (WGS) reaction.

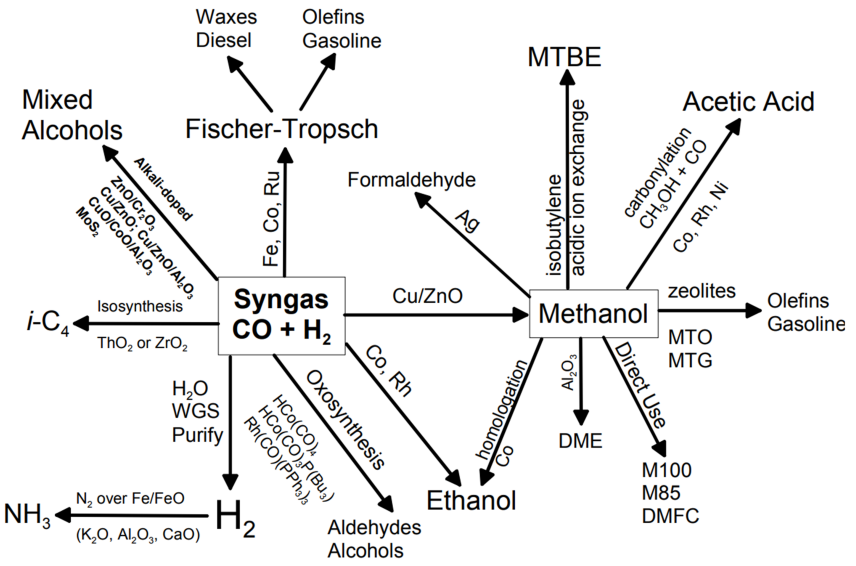


**Figure 2.1:** Potential bio-syngas application schemes following biomass gasification. Reproduced from Spath and Dayton [22].

Some additional bio-syngas applications not included in Figure 2.1 are synthetic natural gas (SNG) production as well as direct power or heat generation [23]. The following sections will focus on the bio-FT process scheme, mainly for the production of sustainable aviation fuels (SAF).

### 2.1.1 Biomass gasification

The gasification process involves thermal decomposition of biomass feedstock through a complex set of reactions, forming mainly $H_2$, CO, $CO_2$, $CH_4$ and $H_2O$ [10]. The typical process scheme can be divided into four partly overlapping reaction domains including drying, pyrolysis, oxidation and reduction [24–26]. The main reactions involved are listed in Table 2.1. The water content in fresh wood is typically 30-60 wt%, and pre-drying of the biomass feedstock is commonly required, reducing the moisture content to 10-15 wt% [27]. Further drying occurs within the biomass gasifier in the

temperature range of 100-250 °C [24]. The vapour is utilised in the following reactions. The pyrolysis involves primary thermal decomposition and vaporisation of volatile components within the biomass. The process occurs without $O_2$ at 200-400 °C, producing a mixture of gases, tar and char. The biomass feed differs from coal in a considerably higher content of volatile constituents, and the pyrolysis hereby plays a larger part in the biomass gasification process [28].

The pyrolysis products further undergo partial or complete oxidation (see reaction R1-R6 in Table 2.1) in the presence of sub-stochiometric amounts of $O_2$ in the temperature range of 600-1400 °C [24]. The exothermic oxidation reactions supply heat for the endothermic drying and pyrolysis steps [26]. The pyrolysis products are also reduced in the presence of $H_2O$ at 600-950 °C [24]. The reduction domain includes the water-gas shift (WGS) reaction (R7) and char steam gasification (R8), also called heterogeneous water-gas shift. The WGS reaction is of particular importance, potentially increasing the $H_2$/CO ratio of the effluent bio-syngas [10]. The ability to adjust the $H_2$/CO ratio is important considering the 2/1 ratio required for downstream FT synthesis [21].

**Table 2.1:** Main biomass gasification reactions.

| No. | Classification | Reaction equation | $\Delta H°$ (kJ/mol) |
|---|---|---|---|
| R1 | Partial oxidation | $C + 1/2O_2 \rightarrow CO$ | -111 |
| R2 | Complete oxidation | $C + O_2 \rightarrow CO_2$ | -394 |
| R3 | Complete oxidation | $CO + 1/2O_2 \rightarrow CO_2$ | -283 |
| R4 | Complete oxidation | $H_2 + 1/2O_2 \rightarrow H_2O$ | -242 |
| R5 | Partial oxidation | $CH_4 + 1/2O_2 \rightarrow CO + 2H_2$ | -37 |
| R6 | Complete oxidation | $CH_4 + 2O_2 \rightarrow CO_2 + 2H_2O$ | -804 |
| R7 | Water-gas shift | $CO + H_2O \leftrightarrow CO_2 + H_2$ | -41 |
| R8 | Steam gasification | $C + H_2O \leftrightarrow CO + H_2$ | 131 |
| R9 | Boudouard | $C + CO_2 \leftrightarrow 2CO$ | 172 |
| R10 | Hydrogasification | $C + 2H_2 \leftrightarrow CH_4$ | -74 |
| R11 | Steam reforming | $CH_4 + H_2O \leftrightarrow CO + 3H_2$ | 205 |
| R12 | Dry reforming | $CH_4 + CO_2 \leftrightarrow 2CO + 2H_2$ | 246 |
| R13 | Partial oxidation | $C_nH_m + (n/2)O_2 \rightarrow nCO + (m/2)H_2$ | < 0 |
| R14 | Steam reforming | $C_nH_m + nH_2O \rightarrow (m/2+n)H_2 + nCO$ | > 0 |
| R15 | Dry reforming | $C_nH_m + nCO_2 \rightarrow 2nCO + (m/2)H_2$ | > 0 |
| R16 | Hydrogenation | $C_nH_m + (2n-m/2)H_2 \rightarrow nCH_4$ | < 0 |
| R17 | Thermal cracking | $C_nH_m \rightarrow (m/4)CH_4 + (n-m/4)C$ | < 0 |

Additional reactions include char decomposition through the Boudouard and hydrogasification (R9-R10) reactions, as well as $CH_4$ steam and dry reforming (R11-R12) [24]. Larger hydrocarbons similarly react through partial oxidation (R13), steam and dry reforming (R14-R15), as well as hydrogenation and thermal cracking (R16-R17).

The gasification process can be divided into indirect allothermal and direct autothermal gasification based on whether the required heat is generated externally or internally from the exothermic combustion and partial oxidation reactions inside the reactor [10]. The autothermal approach requires the presence of $O_2$ within the gasification agent. The typically applied gasification agents are air, $H_2O$/air or $H_2O/O_2$ for autothermal gasification, and $H_2O$ or $CO_2$ upon allothermal gasification [28]. The use of air introduces the issue of $N_2$ dilution, lowering the product gas heating value to 2.5-8.0 MJ/Nm$^3$ [29]. For comparison, heating values in the range of 10-20 MJ/Nm$^3$ are typically afforded with $O_2$ as the gasification agent.

The equivalence ratio (ER) of the gasification process describes the applied amount of $O_2$ relative to the stoichiometric amount required for complete combustion [30]. The effluent $CO_2$ concentrations have been shown to rise with increasing ER at the expense of $H_2$ and CO, lowering the heating value of the product gas. High ER values are however also known to afford a desired high tar conversion efficiency. The steam-to-biomass (S/B) ratio similarly describes the relative amounts of steam and biomass. High S/B ratios are known to increase $CH_4$, tar and char conversion levels and $H_2$/CO ratios due to enhanced steam reforming and WGS reaction activity.

The most commonly applied gasification reactors are updraft and downdraft fixed bed gasifiers, entrained flow gasifiers (EFGs) and fluidized bed gasifiers (FBGs) [31–33]. In an updraft fixed bed gasifier, the gasification agent enters at the bottom of the reactor, flowing counter-current to the top-fed biomass. The downdraft gasifier opposingly involve a co-current flow of the gasification agent and the biomass feed. The updraft and downdraft gasifiers are illustrated in Figure 2.2, showing the effects on the main reaction zones within the two designs [34]. The updraft gasifier typically yields high tar concentrations of around 100 g/Nm$^3$, compared to around 1 g/Nm$^3$ with a downdraft design [31]. The enhanced tar conversion within the downdraft gasifier is attributed to the gasification agent forcing pyrolysis products downwards through the high-temperature combustion and gasification zones [29]. The two fixed bed designs are generally less suited for large scale commercial applications due to low heat and mass transfer efficiencies in the absence of effective mixing.

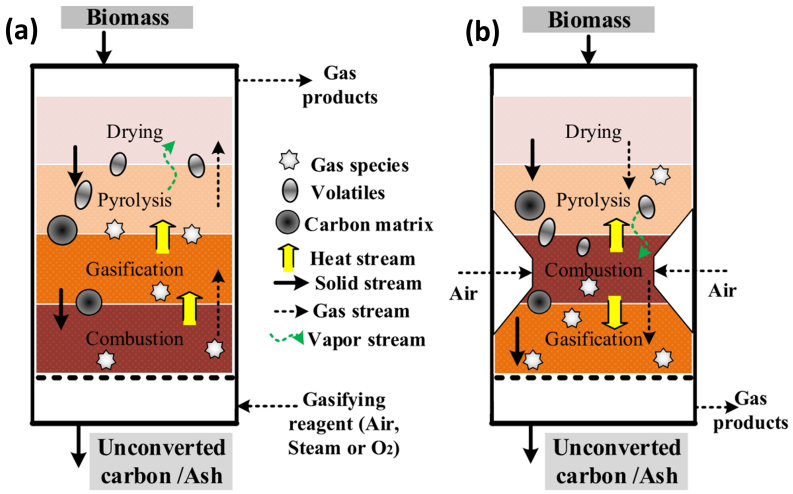


**Figure 2.2:** Principle design and reaction zones of updraft (a) and downdraft (b) fixed bed biomass gasifiers. Reproduced from Zhang *et al.* [34].

The EFG design involves rapid gasification of a small-diameter biomass feed entrained in a high velocity gasification agent flow [35]. EFG reactors are typically operated at 1250-1600 °C and 20-70 bar, with a very short residence time. The severe operating conditions can provide high-quality syngas with complete conversion of tar impurities. However, the high EFG temperature, above the typical melting point of biomass ash, complicates bulk ash collection [34]. Also, EFG operation requires small-diameter particles (around 0.1-1 mm), adding cost-intensive drying and grinding pretreatment steps to the overall process [36, 37].

With the FBG design, the gasification agent flows through a fine particle biomass feed mixed with an inert solid bed material [31]. The FBGs typically provide an intimate contact between the biomass and the gasification agent affording high conversion efficiencies [32]. Some examples on design variations are bubbling, circulating and dual-bed FBGs [37]. For waste feedstocks, bubbling FBG technology has been developed by ThermoChem Recovery International (TRI) [38]. The TRI gasification technology is applied in the Sierra BioFuels plant (Fulcrum Bioenergy, Nevada, USA). This is the only commercial-scale FT-based WTL/BTL plant in operation worldwide (see Section 2.1.4), annually producing 42 million litres of renewable

transportation fuels from 175.000 tonnes of municipal solid waste (MSW). The TRI gasifier is illustrated in Figure 2.3, with the gasification agent (superheated steam) bubbling through the mixed biomass/waste and $Al_2O_3$ bed material. The design is an example of allothermal gasification, heated by high-temperature flue gas flowing through tubes inside the gasifier. This provides a high-quality syngas and enables $H_2$/CO ratio adjustment through gasification temperature control [38]. Also, integrated cyclone separators provide initial removal of particulates within the gasifier design. Generally, the product gas from FBGs typically contains a high number of particulates due to the turbulent conditions inside the reactor [31].

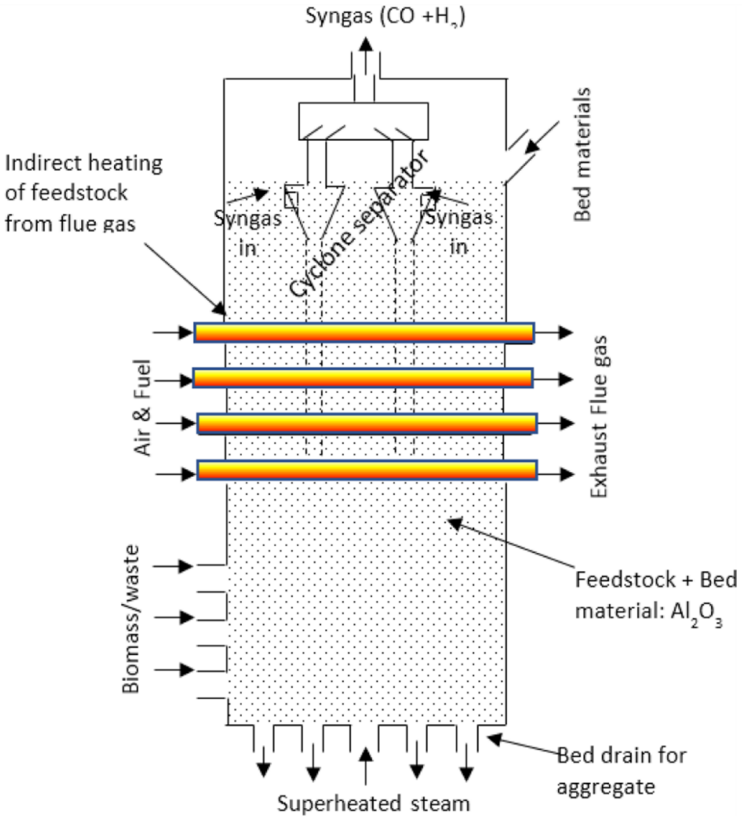


**Figure 2.3:** TRI biomass/waste gasification technology applied in Sierra BioFuels plant (Nevada, USA). Reproduced from Shahabuddin *et al.* [38].

The composition of the effluent product gas (bubbling FBGs) depends heavily on factors like the applied gasification agent [39], biomass feedstock [40], biomass feed particle size, temperature, ER and S/B ratio [41]. The typical range of key operating parameters and main product concentrations are shown in Table 2.2 (atmospheric pressure, lignocellulosic biomass, dry inert-free basis). Also, the product gas contains $C_2H_6$ (0-0.37%), $C_2H_4$ (0.96-4.44%) and $C_2H_2$ (0.03-0.48%) [41]. Higher gasification temperatures have been shown to limit $C_2H_n$ formation (900 °C). The typical FBG product gas additionally contains around 10 g/Nm$^3$ of tar impurities [31]. The tar composition will be further discussed in Section 2.1.2.

**Table 2.2:** Typical bubbling fluidized bed gasifier product gas composition data and operating parameter range (atmospheric pressure, lignocellulosic biomass, dry inert-free basis) [41–43]. Partly reproduced from Puig-Arnavat *et al.* [39].

| | | | Gasification | Product gas composition (vol%) | | | |
|---|---|---|---|---|---|---|---|
| T (°C) | ER (-) | S/B (-) | agent | $H_2$ | CO | $CO_2$ | $CH_4$ |
| 700-900 | 0.19-0.27 | 0-2.70 | $H_2O$/air | 22-39 | 33-43 | 16-22 | 6-10 |
| 785-830 | 0.24-0.51 | 0.48-1.11 | $H_2O/O_2$ | 14-32 | 43-52 | 14-36 | 7-12 |
| 750-780 | 0 | 0.53-1.10 | $H_2O$ | 38-56 | 17-32 | 13-17 | 6-8 |

Recently, machine learning methods were applied to predict bio-syngas properties following FBG steam gasification based on experimental data from 22 publications [44]. The model included 6 biomass feedstock input factors; ash content, fixed carbon, volatile matter and total hydrogen, carbon and oxygen content. Additionally, temperature, ER and S/B ratio were included as gasification condition input factors. The output targets were $H_2$, CO, $CO_2$ and $CH_4$ concentrations (and $H_2$/CO ratio). Figure 2.4 shows the predicted two-factor impact of the three most important input factors (T: temperature, H: biomass hydrogen content, O: biomass oxygen content) on $H_2$ (a-c) and CO concentration (d-f), as well as $H_2$/CO ratio (g-i). The ER and S/B ratio were found to be the most important factors affecting the effluent bio-syngas composition. High $H_2$ concentrations (40-45%) and $H_2$/CO ratios above 2 were predicted with low ER (below 0.08) and high S/B ratios (1-2.5). High CO concentrations (above 25%) were mainly obtained with low S/B ratios (below 1).

The inorganic constituents of the biomass feedstock are during the gasification process converted to solid ash containing alkali and alkali earth metal oxides including $Na_2O$, $K_2O$, MgO and CaO as well as other metal and non-metal oxides like $SiO_2$, $P_2O_5$, $SO_3$, $Al_2O_3$ and $Fe_2O_3$ [45–47].

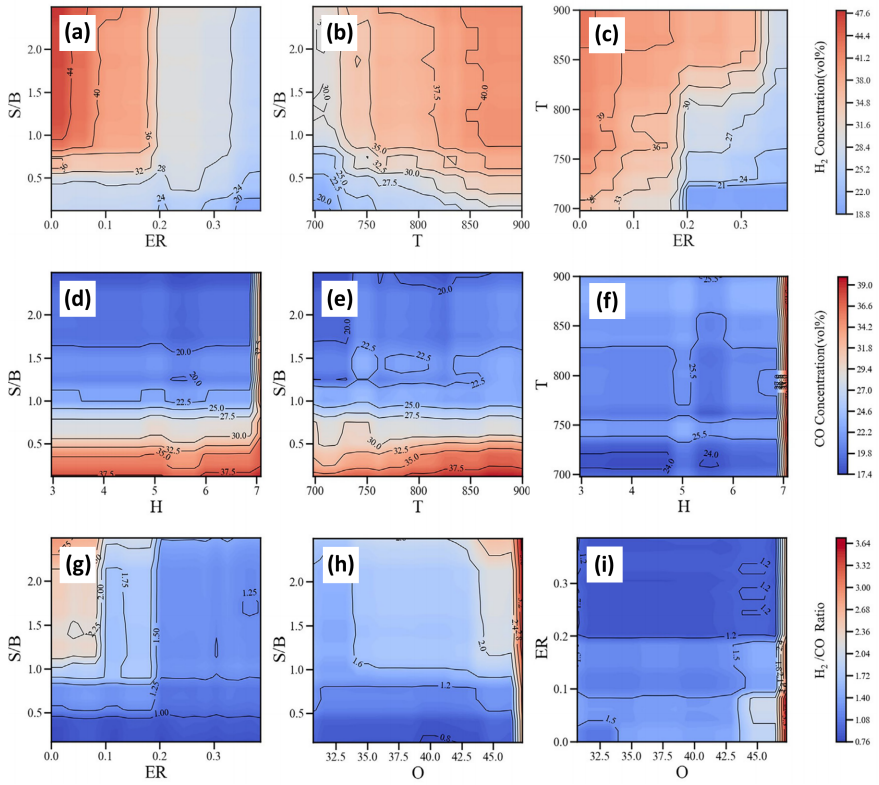


**Figure 2.4:** Two-factor impact of most important FBG steam biomass gasification input factors on $H_2$ (a-c) and CO concentration (d-f), and $H_2$/CO ratio (g-i). Reproduced from Xue *et al.* (machine learning predictions) [44].

The ash content of wood based biomass feedstocks has been reported in the rage of 0.40-3.34 wt% [48]. The product gas also contains small amounts of inorganic gases like $NH_3$, HCN, $H_2S$ and HCl [49]. The biomass feed generally differs from coal in a lower Al and Fe content and higher contents of K and Si [46]. The alkali oxides, producing low melting point mixtures, are particularly challenging regarding ash sintering and slagging in downstream equipment [50]. The ash typically leaves the gasifier as a solid residue at the bottom of the reactor or as fly ash following the product gas stream [10]. This requires a gasification temperature below the ash melting point (typically around 1000 °C) to avoid sintering and slagging.

### 2.1.2 Tar impurities

The product gas following biomass gasification still contains higher molecular weight hydrocarbon impurities commonly called tars that may cause considerable problems with condensation, corrosion, polymerisation and coking in downstream operations [51–53]. The coking issue refers to catalyst deactivation due to the formation of carbonaceous deposits on the catalyst surface [54]. Additionally, tar molecules are carcinogenic and contain considerable amounts of energy [51]. Efficient tar conversion into useful gas products (syngas) is hereby of great technical and economic interest.

Tars may be broadly defined as any organic compound condensable in downstream equipment and are generally considered to consist largely of aromatic hydrocarbons [55]. The tar composition is strongly related to the gasification conditions, evolving with increasing temperature from mixed oxygenates forming around 400 °C, to phenolic ethers at 500 °C, alkyl phenolics at 600 °C, polycyclic aromatic hydrocarbons (PAHs) at 800 °C, and larger PAHs at 900 °C. Typical tars from gasification of lignocellulosic biomass have been reported to contain mostly one-ring (66%) and two-ring (17%) aromatic hydrocarbons like benzene, toluene and naphthalene (see Table 2.3) [56]. The most commonly applied tar model compounds are toluene, benzene, naphthalene and phenol [57].

**Table 2.3:** Typical tar composition from lignocellulosic biomass gasification [56].

| Tar constituent | Amount (wt%) |
|---|---|
| Benzene | 37.9 |
| Toluene | 14.3 |
| Other one-ring aromatic hydrocarbons | 13.9 |
| Naphthalene | 9.6 |
| Other two-ring aromatic hydrocarbons | 7.8 |
| Three-ring aromatic hydrocarbons | 3.6 |
| Four-ring aromatic hydrocarbons | 0.8 |
| Phenolic compounds | 4.6 |
| Heterocyclic compounds | 6.5 |
| Other | 1.0 |

Tars are commonly classified based on their physical properties regarding condensation behaviour and water solubility as shown in Table 2.4 [58]. Class 1 and 5 tars contain very heavy polyaromatic and heavy 4- to 6-ring polyaromatic compounds respectively. These tars will condense at high

temperatures at very low concentrations. Class 2 and 3 tars include water soluble heterocyclic and lighter aromatics respectively. These tars will normally only cause condensation issues at low temperatures and higher concentrations. Class 4 tars contain light 2- and 3-ring polyaromatics, condensing at intermediate temperatures and moderate concentrations.

**Table 2.4:** Tar classification based on water solubility and tar dew point [58].

| Tar class | Classification | Dew point |
|---|---|---|
| Class 1 | GC-undetectable | Very high at low concentrations |
| Class 2 | Heterocyclic aromatics | $<$ -50 °C at 10 g/Nm$^3$ |
| Class 3 | Light aromatics | $<$ -50 °C at 10 g/Nm$^3$ |
| Class 4 | Light polyaromatics | $>$ 10 °C at 1 mg/Nm$^3$ |
| Class 5 | Heavy polyaromatics | $\geq$ 120 °C at 0.1 mg/Nm$^3$ |

### 2.1.3 Fischer-Tropsch requirements

The typically required maximum amounts of some common bio-syngas impurities for downstream FT-applications are listed in Table 2.5 [59]. The nitrogen-, sulphur- and halogen-containing impurities must be removed due to their corrosive nature and metal-catalyst poisoning properties [59–61]. The nitrogen- and sulphur-containing compounds are also subject to environmental regulations regarding their $NO_x$ and $SO_2$ derivatives [61]. Alkali oxides similarly present issues with corrosion, catalyst deactivation and reactor bed agglomeration, sintering and slagging. The removal of particulates is required to avoid downstream clogging and erosion [52].

**Table 2.5:** Maximum amounts of common bio-syngas impurities for downstream Fischer-Tropsch applications [59].

| Contaminants | Maximum amount |
|---|---|
| $NH_3$ | 10 ppm |
| HCN | 10-20 ppb |
| $H_2S$ | 10-60 ppb |
| HCl / HBr | 10 ppb |
| $Na_2O$ / $K_2O$ / MgO / CaO | 10 ppb |
| Particulates | 0.1 ppm |
| Tars | Below tar dew point (a) |

(a) See Section 2.1.2 regarding tar composition and dew point.

The tar removal is generally required to avoid plugging of downstream equipment due to tar condensation and polymerisation as well as deactivation of FT-catalysts by tar deposition and coke formation [62]. Efficient tar elimination has been put forth as the greatest challenge in the commercialisation of bio-FT technology [10]. The tar dew point and the required tar removal is strongly dependent on the specific tar composition (see Section 2.1.2). However, the total tar content is typically required to be below 1 mg/Nm$^3$ [63]. Table 2.6 shows an overview of tar concentration limits and associated problems for different bio-syngas applications.

**Table 2.6:** Tar concentration limits for different bio-syngas application [63].

| Application | Concentration limit (mg/Nm$^3$) | Problems |
|---|---|---|
| Fischer-Tropsch | 1 | Catalyst coke formation. |
| Methanol synthesis | 1 | Catalyst coke formation. |
| Methanation | 1 | Catalyst coke formation. |
| Gas engine | 100 | Carbon deposition and injection system tar condensation. |
| Gas turbine | 5 | Carbon deposition and turbine blade erosion. |
| Fuel cell | 1 | Anode degradation by carbon deposition and corrosion. |

### 2.1.4 Commercialisation status

A selection of bio-FT commercialisation efforts around the world is shown in Table 2.7. The list is based on a summary by ETIP (European Technology and Innovation Platform) Bioenergy (updated in 2022) [64] and reviewed by the author. The list includes operational/planned demonstration or commercial scale plants fully integrating biomass gasification (waste or non-food cellulosic feedstocks) and FT-technology. It should be noted that plant specifications are largely based on online (none peer reviewed) sources.

The most mature biomass gasification technology is the TRI bubbling FBG (see Section 2.1.1), applied by Fulcrum Bioenergy in the Sierra BioFuels plant (Nevada), the Centerpoint BioFuels plant (Indiana) and the Trinity Fuels plant (Gulf Coast) in USA. The TRI technology is also applied by Fulcrum Bioenergy and Essar in the Fulcrum NorthPoint plant (Cheshire) and by British Airways and Velocys in the Altalto plant (Immingham) in England.

**Table 2.7:** Selection of bio-FT commercialisation efforts around the world.

| | |
|---|---|
| **Sierra BioFuels** [38, 65–69] | **Project specifications:** |
| | Partners: Fulcrum Bioenergy<br>Plant location: Reno, Nevada, USA<br>Classification: Commercial plant<br>Production scale: 42 ML/year (basis not specified)<br>Feedstock: MSW<br>Product: Transportation fuels (not specified)<br>Status: Production started in 2022 |
| | **Bio-FT technology:** |
| | Gasification: TRI bubbling fluidized bed gasifier (superheated steam, 600-800 °C, 4 bar, $Al_2O_3$ bed).<br>Cleaning: Non-catalytic $CH_4$/tar partial oxidation (POX), Praxair Hot Oxygen Burner (HOB) technology (turbulent oxygen jet, 1100 °C) + wet scrubbing + guard beds.<br>Fischer-Tropsch: JM/bp FT CANS™ technology. |
| **Centerpoint BioFuels** [38, 66, 67, 70] | **Project specifications:** |
| | Partners: Fulcrum Bioenergy<br>Plant location: Gary, Indiana, USA<br>Classification: Commercial plant<br>Production scale: 117 ML/year SAF<br>Feedstock: MSW<br>Product: SAF (not further specified)<br>Status: Production planned from 2025 |
| | **Bio-FT technology:** |
| | Gasification: TRI bubbling fluidized bed gasifier (superheated steam, 600-800 °C, 4 bar, $Al_2O_3$ bed).<br>Cleaning: Wet scrubbing + guard beds.<br>Fischer-Tropsch: JM/bp FT technology. |
| **Trinity Fuels** [38, 66, 67, 71] | **Project specifications:** |
| | Partners: Fulcrum Bioenergy<br>Plant location: Gulf Coast, USA<br>Classification: Commercial plant<br>Production scale: 117 ML/year SAF<br>Feedstock: MSW<br>Product: SAF (not further specified) |

| | |
|---|---|
| | Status: Production planned from 2026 |
| | **Bio-FT technology:** |
| | Gasification: TRI bubbling fluidized bed gasifier (superheated steam, 600-800 °C, 4 bar, $Al_2O_3$ bed).<br>Cleaning: Wet scrubbing + guard beds.<br>Fischer-Tropsch: JM/bp FT technology. |
| **Fulcrum NorthPoint** [38, 66, 67, 72] | **Project specifications:** |
| | Partners: Fulcrum Bioenergy and Essar<br>Plant location: Cheshire, England<br>Classification: Commercial plant<br>Production scale: 100 ML/year SAF<br>Feedstock: Organic MSW<br>Product: Drop-in fuels (including SAF)<br>Status: Production planned from 2027 |
| | **Bio-FT technology:** |
| | Gasification: TRI bubbling fluidized bed gasifier (superheated steam, 600-800 °C, 4 bar, $Al_2O_3$ bed).<br>Cleaning: Wet scrubbing + guard beds.<br>Fischer-Tropsch: JM/bp FT technology. |
| **Altalto** [38, 67, 73, 74] | **Project specifications:** |
| | Partners: British Airways and Velocys<br>Plant location: Immingham, England<br>Classification: Commercial plant<br>Production scale: 60 ML/year (basis not specified)<br>Feedstock: MSW<br>Product: Kerosene, diesel and naphtha<br>Status: Production planned from 2027 |
| | **Bio-FT technology:** |
| | Gasification: TRI bubbling fluidized bed gasifier (superheated steam, 600-800 °C, 4 bar, $Al_2O_3$ bed).<br>Cleaning: Delivered by Air Liquide (not specified).<br>Fischer-Tropsch: Velocys FT technology. |
| **BioTfueL** [75–77] | **Project specifications:** |
| | Partners: Axens, CEA, IFP Energies Nouvelles, Avril, Thyssenkrupp and TotalEnergies<br>Plant location: Dunkirk, France |

| | |
|---|---|
| | Classification: Demonstration plant<br>Production scale: 60 ton/year diesel and jet fuel<br>Feedstock: Forest/agricultural waste and designated energy crops<br>Product: Diesel and jet fuel<br>Status: Technology demonstrated in 2021 (commercial scale-up under planning)<br>**Bio-FT technology:**<br>Gasification: Thyssenkrupp uhde® entrained-flow gasifier (steam/air, above ash melting temperature, 40 bar).<br>Cleaning: Scrubbing (not further specified).<br>Fischer-Tropsch: Axens Gasel® FT technology. |
| **BayuoFuels** [78, 79] | **Project specifications:**<br>Partners: Velocys (in negotiation)<br>Plant location: Natchez, Mississippi, USA<br>Classification: Commercial plant<br>Production scale: 125 ML/year SAF + naphtha<br>Feedstock: Waste woody biomass<br>Product: SAF (kerosene) and naphtha<br>Status: Pre-FEED and permitting completed<br>**Bio-FT technology:**<br>Gasification: Not specified.<br>Cleaning: Not specified.<br>Fischer-Tropsch: Velocys FT technology. |
| **Red Rock Biofuels** [80, 81] | **Project specifications:**<br>Partners: Red Rock Biofuels and Frontline<br>Plant location: Lakeview, Oregon, USA<br>Classification: Commercial plant<br>Production scale: 76 ML/year SAF + diesel<br>Feedstock: Waste woody biomass<br>Product: SAF and diesel<br>Status: Discontinued in 2023<br>**Bio-FT technology:**<br>Gasification: Frontline BioEnergy TarFreeGas® pressurised bubbling fluidized bed (steam/air/oxygen, temperature not specified, up to 10 bar, sand bed). |

| | |
|---|---|
| | Cleaning: Frontline BioEnergy PMFreeGas® removal of char/ash (not further specified).<br>Fischer-Tropsch: Velocys FT technology. |
| **Toyo**<br>[82, 83] | **Project specifications:**<br>Partners: Toyo Engineering Corporation, JERA and Mitsubishi Power<br>Plant location: Nagoya, Japan<br>Classification: Demonstration plant<br>Production scale: 27 L/day SAF<br>Feedstock: Woody biomass<br>Product: SAF (not further specified)<br>Status: Technology demonstrated in 2020 (commercial scale-up under planning)<br>**Bio-FT technology:**<br>Gasification: Mitsubishi Power entrained-flow (steam/oxygen, temperature not specified, atmospheric pressure).<br>Cleaning: Not specified.<br>Fischer-Tropsch: Velocys FT technology. |
| **COMSYN**<br>[84] | **Project specifications:**<br>Partners: VTT, GKN, DLR, Wood, ORLEN UniCRE, AFRY and INERATEC<br>Plant location: Espoo, Finland<br>Classification: Pilot plant<br>Production scale: 100 kg/hour biomass<br>Feedstock: Wood/agricultural residues<br>Product: Kerosene, gasoline and diesel<br>Status: Project ended in 2021<br>**Bio-FT technology:**<br>Gasification: Dual fluidized bed gasifier (steam/air, 700-820 °C, 1-3 bar).<br>Cleaning: High-temperature filtration (800 °C), tar/hydrocarbon steam reforming (900 °C) with oxygen feed, fixed bed ZnO/activate carbon sulphur adsorbent.<br>Fischer-Tropsch: INERATEC FT technology. |

In the Sierra BioFuels plant, the TRI gasifier is combined with $CH_4$/tar elimination by partial oxidation (POX) with Praxair Hot Oxygen Burner (HOB) technology (non-catalytic). Additionally, wet scrubbing and guard beds are typically applied for bio-syngas conditioning before FT-applications.

## 2.2 Bio-syngas conditioning

The bio-syngas conditioning generally includes cooling, cleaning (removal of inorganic impurities, tars and particulates) and $H_2$/CO ratio adjustment. The cleaning steps can be divided into hot and cold cleaning strategies depending on weather or not the product gas is cooled before or after the cleaning [85]. The cold gas cleaning can further be divided into dry and wet cleaning measures where dry cleaning equipment includes cyclones, rotating particle separators (RPSs), electrostatic precipitators (ESPs), absorbers and bag, baffle, ceramic, fabric and sand bed filters. The wet cleaning includes spray towers, wet cyclones, wet ESPs and packed column, impingement and venture scrubbers. The hot gas cleaning is typically divided into high-temperature thermal treatment and catalytic treatment inside the gasification reactor or in a downstream reformer. The typically applied cleaning measures for inorganic and particulate contaminants has been reviewed elsewhere [85–87]. The wide range of tar elimination strategies will be briefly discussed in Section 2.2.2.

### 2.2.1 $H_2$/CO ratio adjustment

The required $H_2$/CO ratio adjustment can be achieved by the WGS reaction (see R7 in Table 2.1). The forward reaction is mildly exothermic, and thermodynamically favoured at low temperatures and kinetically favoured at high temperatures. Traditionally, the WGS reaction is performed in a high-temperature (HT-WGS) reactor with Fe-Cr oxide catalysts (at 310-450 °C), or in a low-temperature (LT-WGS) reactor with Cu-Zn oxide catalysts (at 200-250 °C) [88]. However, high WGS activity is also obtained with Ni-based steam reforming catalysts [89], and the minor bio-syngas $H_2$/CO ratio adjustment required for downstream FT-applications could be achieved during simultaneous steam reforming of hydrocarbon impurities.

Few reports were found considering relevant ultra-high-temperature (UHT-WGS) conditions. Ashok *et al.* [89] reviewed the development of Ni-based catalysts for HT-WGS and UHT-WGS reaction applications, including only one study considering temperatures up to 650 °C. Additionally, two reports on higher temperatures were found in previous literature. Haryanto *et al.* [90] studied UHT-WGS performance of $CeO_2/Al_2O_3$ supported Rh, Pt, Pd,

Ir, Ru, Ag and Ni catalysts with a fairly high steam-to-gas (S/G) ratio of 5.2 (CO basis) and pure CO/$H_2O$ in the feed. A high $H_2$-selectivity (94.7%) was reported for the Pt-$CeO_2$/$Al_2O_3$ catalyst at 700 °C (CO conversion = 76.3%, $H_2$-yield = 52.2%). Chein *et al.* [91] studied a series of Pt, Ni and Pt-Ni catalysts with $Al_2O_3$, $TiO_2$, $CeO_2$/$Al_2O_3$ and $CeO_2$/$TiO_2$ supports for $H_2$ upgrade in model syngas (18/30/22/30 mol% $H_2$/CO/$CO_2$/$N_2$) at 750-850 °C with S/G ratios of 1-5 (CO+$CO_2$ basis). $H_2$-yields up to around 35% were found throughout the tested conditions. Generally, the WGS discussion is focused on $H_2$ production where low temperatures and high S/G ratios are required due to thermodynamic limitations.

### 2.2.2 Tar elimination strategies

Tar removal methods can be classified as physical absorption processes or chemical catalytic and non-catalytic thermal techniques [11]. Chemical elimination is considered to be favourable compared to physical tar removal due to the increased overall efficiency from the conversion of hydrocarbon impurities into useful gas products (syngas) [58]. The bio-syngas tar content has been reported to contain up to 5-15% of the energy in the product gas [63]. Physical absorption strategies additionally require expensive solvent regeneration and toxic waste treatment procedures [57]. Non-catalytic thermal cracking typically requires high temperatures above 1000 °C and is energetically inefficient compared to catalytic strategies [61]. Catalytic reforming can further be divided into primary and secondary techniques involving catalytic treatment inside the gasifier (*in situ*) or in a downstream secondary reformer (*ex situ*) [57]. Primary catalytic strategies typically suffer from considerable stability issues in the harsh gasification environment, and secondary techniques, allowing a better control of the catalyst environment, are generally preferred. Catalytic steam reforming is considered an attractive approach with simultaneous $CH_4$/tar elimination at relatively low operating temperatures [11, 57, 92].

## 2.3 Ni-based steam reforming catalysts

The development of commercially applicable reforming catalysts generally requires high reforming activity, suitable product selectivity, high deactivation resistance, easy regeneration, high mechanical strength and low cost of production [92]. Supported metal catalysts including Ni, Co, Fe, Rh, Ru, Pt, Pd and Ir have been shown both theoretically and experimentally to provide the desired hydrocarbon steam reforming activity [92–95]. The noble metals Rh and Ru show the highest activity [95], but Ni-based catalysts

are generally preferred for commercial applications due to the superior activity-to-cost ratio [11]. Both Co and Fe show good theoretical activities, but are more prone to metal oxidation (compared to Ni) [94].

The high reforming activity of Ni-based catalysts is generally attributed to the ability of metallic Ni to activate hydrocarbon C-H and C-C bonds as well as $H_2O$ and $CO_2$ molecules involved in reforming and WGS reactions [92]. Further development of Ni catalysts should focus on the four main challenges pointed out by Sehested [96], targeting the improvement of catalyst activity and resistance towards deactivation by coke formation, metal particle sintering and poisoning. Small amounts of $H_2S$ (100-200 ppm) expected downstream of biomass gasification is considered the main poisoning agent, with strong catalyst deactivation effects (Ni catalysts) [97, 98]. Furthermore, coke formation is a key challenge in catalytic reforming of biomass gasification tars, and Ni-based catalysts are commonly modified to reduce deactivation by coke formation [99]. The most common modifications can be grouped by the addition of secondary metals (Co, Fe, Cu, Cr), noble metal promotion (Pt, Pd, Rh, Ru), addition of rare earth metal oxides (Ce, La), doping with alkali metals (Li, Na, K) and alkaline earth metal oxides (Mg, Ca) as well as modification of the catalyst support. The wide range of modification strategies has been reviewed elsewhere [12, 57, 99].

### 2.3.1 Deactivation by coke formation

Catalyst coke generally refers to unwanted carbonaceous species formed on the catalyst surface, blocking active sites and pores, leading to a loss of catalyst activity. An overview of commonly described deactivation effects following coke formation is shown in Figure 2.5 [100].
Figure 2.5 includes (i) active site blocking by chemisorption/physisorption of carbon species, (ii) metal particle encapsulation, (iii) pore blocking and (iv) structural catalyst degradation (following carbon filament growth) [100].

The carbon filament growth refers to graphitic carbon whiskers growing from catalyst metal particles [96]. The filament growth mechanism is still debated, considering carbon transportation through metal bulk diffusion vs over the metal particle surface. Leung *et al.* [101] recently found the filament growth rate to be proportional to $P_{CH_4}P_{CO}/P_{CO_2}$ and $P_{CH_4}P_{H_2}/P_{H_2O}$ partial pressure ratios, consistent with a growth model limited by carbon bulk diffusion rates (SMR/DRM with Ni/MgO catalysts). Further graphitization of carbon filaments following extensive filament growth has additionally been described in previous literature (ESR) [102], with strong deactivation effects through bulk encapsulation and blocking of catalyst pores.

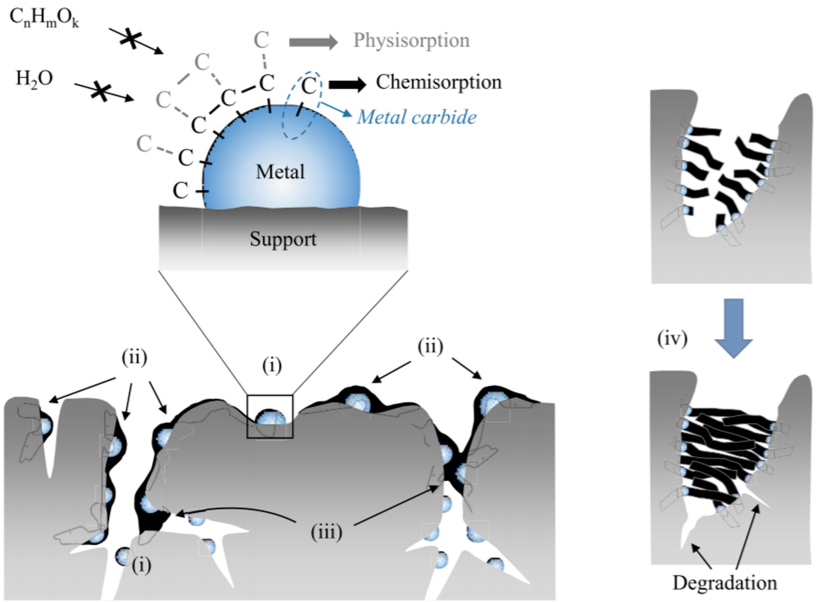


**Figure 2.5:** Common deactivation effects following coke formation, with (i) active site blocking, (ii) metal particle encapsulation, (iii) pore blocking and (iv) structural degradation. Reproduced from Ochoa *et al.* [100].

### 2.3.2 Hydrotalcite-based Ni-Co catalysts

Bi-metallic Ni-Co catalysts have been put forth as particularly interesting for tar steam reforming, potentially improving catalyst activity and coke formation resistance through the formation of stable, high dispersion Ni-Co alloy particles [12]. Wang *et al.* [103] studied the performance of 12-15 wt% Ni-Co/$Al_2O_3$ catalysts for steam reforming of biomass pyrolysis tars. The performance in terms of reforming activity and coke formation resistance was shown to follow Ni-Co > Co > Ni, with an optimum 4-1 Ni-Co ratio. It should however be noted that the mono-metallic Co/$Al_2O_3$ was reported to outperform the Ni-Co catalyst in further toluene steam reforming tests. Gao *et al.* [104] tested the performance of a series of Ni-Co/$La_2O_3$ catalysts in toluene steam reforming, reporting on high toluene conversion levels, reduced coke deposition and enhanced metal dispersion in the optimised 4-1 Ni-Co system. Nabgan *et al.* [105] similarly tested a series of 10 wt% Ni-

$Co/ZrO_2$ catalysts in steam reforming of phenol. The 3-1 Ni-$Co/ZrO_2$ sample was found to provide the highest phenol conversion and $H_2$ yield, accompanied by low coke formation. The enhanced performance of the 3-1 Ni-Co sample was shown to correlate with a high number of basic sites through $CO_2$ temperature-programmed desorption ($CO_2$-TPD) analysis.

The development of Ni-Co catalysts for biomass tar steam reforming was reviewed by Li *et al.* [106], highlighting catalyst preparation *via* hydrotalcite-like precursors, potentially providing high-activity uniform alloy catalysts. The general $M(II)_6M(III)_2(OH)_{16}CO_3{\cdot}4H_2O$ hydrotalcite structure is shown in Figure 2.6 [107]. Such bi-metallic Ni-Co/Mg(Al)O catalysts prepared through calcination and reduction of hydrotalcite-like precursors have mostly been studied for $H_2$ production by ethanol steam reforming (ESR) [13, 108–112]. He *et al.* [13] studied the effect of Ni-Co ratio (40-0, 30-10, 20-20, 10-30 and 0-40 wt%) for ESR applications. The catalyst surface area, metal dispersion and reduction resistance were found to depend on the degree of formation of the hydrotalcite-like precursor, decreasing with increasing Co content. The 10-30 wt% Ni-Co/Mg(Al)O catalyst was reported to provide the overall best performance in the ESR reaction. He *et al.* [108] also tested these catalysts in sorption enhanced steam reforming of ethanol (SESRE) with a CaO-based $CO_2$ acceptor. The excellent reforming and WGS activity of the Ni-Co/Mg(Al)O catalysts was demonstrated, affording $H_2$ purities above 99% with the 40-0 and 20-20 wt% Ni-Co/Mg(Al)O samples.

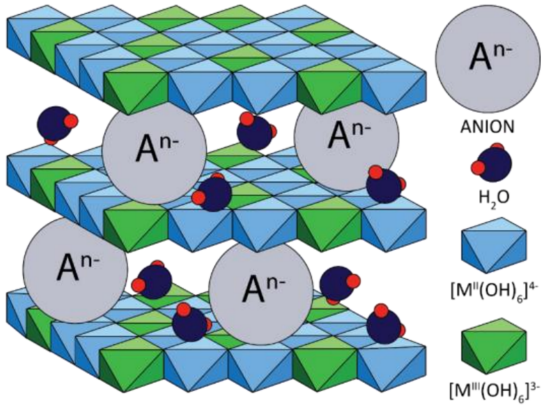


**Figure 2.6:** Schematic illustration of $M(II)_6M(III)_2(OH)_{16}CO_3{\cdot}4H_2O$ structure of hydrotalcite-like precursors. Reproduced from Dębek *et al.* [107].

Shejale and Yadav [109] compared the ESR performance of a hydrotalcite-based Ni/Mg(Al)O catalyst with Ni on MgO, $Al_2O_3$, $CeO_2$ and $ZrO_2$ supports. The Ni/Mg(Al)O catalyst was reported to provide superior reforming activity and $H_2$ selecivity compared to the other metal-oxide supports. A Cu promoted (1-5 wt%) 10-10 wt% Ni-Co/Mg(Al)O catalyst was additionally shown to provide excellent $H_2$ yields and low formation of known coke precursors. Muñoz *et al.* [110] compared a hydrotalcite-derived (25 wt%) 1-1 Ni-Co/Mg(Al)O catalyst with the equivalent mono-metallic Ni and Co catalysts. The Ni-Co synergy was found to enhance oxygen mobility and basicity of the catalyst increasing the performance in oxidative steam reforming of ethanol (OSRE). Further promotion of the Ni/Mg(Al)O, Co/Mg(Al)O and Ni-Co/Mg(Al)O catalysts with Ce and Pr was reported to increase the WGS activity. Muñoz *et al.* [111] also studied the effect of Ni-Co ratio (2-1, 1-1 and 1-2) compared to the mono-metallic equivalents in OSRE without catalyst pre-reduction. The 1-1 Ni-Co/Mg(Al)O and Ni/Mg(Al)O catalysts were found to provide the best *in situ* reducibility and OSRE activity. de Souza *et al.* [112] studied the effects of the addition of Mg, Zn, Mo and Co to Ni-Al hydrotalcite-like precursors on catalyst ESR performance. The presence of Zn, Mo and Co was found to enhance catalyst reducibility and ESR activity compared to the Ni-Al and Mg-Ni-Al precursors. The Ni-Al catalyst also showed a particularly high susceptibility towards coke formation attributed to a higher surface acidity.

The steam reforming performance of hydrotalcite-based Ni-Co catalysts has also been demonstrated with other hydrocarbons [113–116]. He *et al.* [113] tested two 10-30 and 15-25 wt% Ni-Co/Mg(Al)O catalysts in sorption enhanced steam reforming of glycerol (SESRG) with a calcined dolomite $CO_2$ acceptor, reporting on excellent reforming and WGS activity with $H_2$ yields and purities above 99%. Noor *et al.* [114] tested two hydrotalcite-derived 30-10 and 20-20 wt% Ni-Co/Mg(Al)O catalysts in sorption enhanced water-gas shift (SEWGS) with a CaO-based $CO_2$ acceptor. The 20-20 wt% Ni-Co/Mg(Al)O catalyst was further promoted with Pd (1 wt%) enhancing the observed CO conversion. The 30-10 wt% Ni-Co/Mg(Al)O catalyst was however reported to outperform the Pd-Ni-Co/Mg(Al)O catalyst regarding a lower methanation activity at low temperatures and high CO feed pressures. Ghungrud *et al.* [115] studied Ce-promotion of a hydrotalcite-based 20-20 and 10-30 wt% Ni-Co/Mg(Al)O bi-functional catalyst and $CO_2$ acceptor for low-temperature sorption enhanced steam methane reforming (SESMR). The effect of Ni-Co ratio (40-0, 30-10, 20-20, 10-30 and 0-40 wt%) on SESMR performance at 450 °C was included in a preliminary screening. The highest $CH_4$ conversion and $H_2$ yield was reported for the 20-20 and 10-30 wt%

Ni-Co/Mg(Al)O samples. Ce-promotion was shown to improve $CO_2$ adsorption capacity and coke resistance by increasing surface area and basicity.

Duan *et al.* [116] recently studied a series of 12 wt% Ni-Co/Mg(Al)O catalysts derived from hydrotalcite-like precursors for dry reforming of methane (DRM). Again, increasing catalyst basicity upon Co addition, accompanied by reduced coke deposition, was shown by $CO_2$-TPD analysis. Carbon filament growth (observed with SEM) was shown to be effectively suppressed in the mono-metallic Co/Mg(Al)O sample. This was however at the expense of catalyst activity, and the overall best performance was reported for the 3-9 wt% Ni-Co catalyst. The Ni-Co synergy was attributed to enhanced $CO_2$ adsorption at metal particles and/or metal-support interface, promoting coke gasification reactions. Recently, Ren *et al.* [117] demonstrated that the number of basic sites of mixed oxide Mg(Al)O supports (Ni catalysts for $CO_2$ methanation) can be considerably enhanced upon high-temperature calcination (1.28-2.18 mmol/$g_{cat}$ at 500-1000 °C). Further investigations considering calcination temperature effects on hydrotalcite-derived catalyst coke formation resistance is hereby considered to be highly interesting. The work presented in Paper I-IV includes the first reports on hydrotalcite-based Ni-Co catalyst performance in bio-syngas $CH_4$/tar steam reforming at relevant operating conditions.

### 2.3.3 Noble metal promotion

Noble metal promotion with Pt, Pd, Rh and Ru has been reported to improve catalyst reforming activity (steam methane reforming, SMR) and resistance to coke formation and Ni oxidation through bi-metallic synergy effects [118]. In catalytic biomass gasification, several studies report on enhanced performance following Pt promotion. Chaiprasert *et al.* [119] tested a 10 wt% Ni/dolomite catalyst promoted with Pt, Fe and Co (1 wt%) in steam gasification of coconut shell (FBG, 800 °C). All promoters were found to reduce coke formation with Pt < Fe < Co (6.5-9.3 wt%) compared to the unpromoted Ni catalyst (16.5 wt%). Nishikawa *et al.* [120] similarly studied the promotion of 4-12 wt% Ni/$CeO_2$/$Al_2O_3$ catalysts with Pt, Pd, Rh and Ru (0.01-0.5 wt%) in steam gasification of cedar wood (dual-bed gasifier), reporting on the best performance following Pt promotion. In particular, no pre-reduction step was required for the Pt promoted samples. Pt-Ni alloy formation was suggested by EXAFS (extended X-ray absorption fine structure) analysis. Fermoso *et al.* [15] tested a hydrotalcite-based Pd promoted (1 wt%) 20-20 wt% Ni-Co/Mg(Al)O catalyst for *in situ* sorption enhanced catalytic steam gasification (SECSG) of lignocellulosic biomass with

a dolomite $CO_2$ acceptor. The Pd-Ni-Co/Mg(Al)O catalyst showed excellent reforming and WGS activity, high tar/$CH_4$ conversion levels and high $H_2$ yields. Stable operation was demonstrated through several reaction and regeneration cycles, with no intermediate reduction step required. The application of such Pd-Ni-Co/Mg(Al)O catalysts have also been reported for SEWGS [114] and high-pressure sorption enhanced steam reforming (SESR) of acetic acid, glycolaldehyde and hydroxyacetone as byproducts from biomass fast-hydropyrolysis [121].

The *in situ* activation and self-regeneration properties following Pt/Pd/Rh promotion of Ni/Mg(Al)O catalysts derived from hydrotalcite precursors have been extensively studied for daily start-up and shut-down (DSS) SMR operation [16]. The self-regeneration properties during DSS SMR were not obtained with unpromoted Ni/Mg(Al)O samples, and were attributed to continuous re-reduction of oxidised Ni from Mg(Ni,Al)O periclase following noble metal H-spillover [122, 123]. The effects were most strongly observed in Pt-Ni/Mg(Al)O (with optimised Pt-loading), attributed to $CH_4$ dissociation assisted by adsorbed oxygen species (Pt-O and/or Pt-OH) on Pt (or Pt-Ni alloy) particles [124]. The results were supported by theoretical studies on $CH_4$ dissociation and syngas formation on transition metal M(111) surfaces (M = Ru/Os/Rh/Ir/Pd/Pt/Cu/Ag/Au), showing that adsorbed oxygen promotes $CH_4$ dehydrogenation in the case of Pt [125]. Such *in situ* activation capabilities are considered to be highly interesting regarding cyclic regeneration of bio-syngas tar reforming catalysts by coke combustion/gasification, potentially avoiding intermediate reduction steps.

# 3 Methodology

## 3.1 Catalyst preparation

The Ni-Co/Mg(Al)O, Ni/Mg(Al)O and Co/Mg(Al)O catalysts were synthesised based on the protocol reported by He *et al.* [13]. The (Ni+Co+Mg)/Al and NaOH/Al ratios (molar basis) were kept constants at 6/2 and 16/2 respectively to resemble the $M(II)_6M(III)_2(OH)_{16}CO_3{\cdot}4H_2O$ composition of the hydrotalcite structure. The $Na_2CO_3$ was added in excess (50 mol%). Samples were prepared targeting a Ni-Co loading of 30-10, 20-20, 10-30, 15-15 and 10-10 wt% (Ni+Co+MgO+$Al_2O_3$ basis). The mono-metallic 40 wt% Ni/Mg(Al)O and Co/Mg(Al)O samples were prepared for reference. The hydrotalcite-like precursors were prepared by co-precipitation, pumping an anion solution (200 mL/hour) of NaOH and $Na_2CO_3$ dissolved in DI-water (400 mL) dropwise into a stirred (400 rpm) cation solution of $Ni(NO_3)_2{\cdot}6H_2O$, $Co(NO_3)_2{\cdot}6H_2O$, $Mg(NO_3)_2{\cdot}6H_2O$ and $Al(NO_3)_3{\cdot}9H_2O$ dissolved in DI-water (400 mL). The pH was adjusted to 8-9 by addition of $HNO_3$ (ca 4.3 mL, 68% in $H_2O$). The reaction mixture was heated at 80 °C and aged overnight for 16 hours. The mixture was cooled to room temperature, and the precipitate washed with DI-water (ca 3000 mL) by vacuum filtration. The pH of the filtrate was measured to 6-7 at the end of the filtration. The hydrotalcite-like precursors were dried overnight at 80 °C and calcined at 600 °C for 6 hours in air (60 NmL/min) after 2 hours of additional pre-drying at 80 °C. The temperature ramp rate was 5 °C/min. The effect of calcination temperature was studied through calcination of the 15-15 wt% Ni-Co precursor at 600, 700 and 800 °C. All samples were crushed and sieved to the required particle size (75-150 or 150-250 µm).

The noble metal promoted samples (Pt, Pd and Rh) were prepared by incipient wetness impregnation (1.0 wt%, Pt/Pd/Rh+Ni+Co+MgO+$Al_2O_3$ basis) of the 20-20 wt% Ni-Co calcined precursor (NiO+CoO+MgO+$Al_2O_3$ basis). The impregnation solutions were prepared from $Pt(NO_3)_4$ solution (ca 15 wt% Pt), $Pd(NO_3)_2{\cdot}2H_2O$ (ca 40 wt% Pd) and $Rh(NO_3)_3{\cdot}xH_2O$ (ca 36 wt% Rh). The samples were dried overnight at 80 °C and calcined at 600 °C following the protocol previously described. Table 3.1 shows an overview of sample compositions prepared in this work. All applied chemicals were acquired from Sigma-Aldrich (Merch), VWR Chemicals or Thermo Fisher Scientific.

**Table 3.1:** Overview of catalyst sample compositions prepared in this work.

| Metal loading (wt%) | | | | | Calcination |
|---|---|---|---|---|---|
| Ni | Co | Pt | Pd | Rh | temperature (°C) |
| 40 | 0 | 0 | 0 | 0 | 600 |
| 30 | 10 | 0 | 0 | 0 | 600 |
| 20 | 20 | 0 | 0 | 0 | 600 |
| 10 | 30 | 0 | 0 | 0 | 600 |
| 0 | 40 | 0 | 0 | 0 | 600 |
| 15 | 15 | 0 | 0 | 0 | 600 |
| 10 | 10 | 0 | 0 | 0 | 600 |
| 15 | 15 | 0 | 0 | 0 | 700 |
| 15 | 15 | 0 | 0 | 0 | 800 |
| 20 | 20 | 1.0 | 0 | 0 | 600 (a) |
| 20 | 20 | 0 | 1.0 | 0 | 600 (a) |
| 20 | 20 | 0 | 0 | 1.0 | 600 (a) |

(a) Calcined two times (before and after noble metal impregnation).

## 3.2 Catalyst characterisation

### 3.2.1 XRD

Powder X-ray diffraction (XRD) was performed on a Bruker D8 A25 DaVinci X-ray Diffractometer with CuK$\alpha$ radiation and a LynxEye$^{TM}$ SuperSpeed Detector. Sample holders were covered with a Kapton film for all samples. An additional zero diffraction Si-cavity wafer (10 mm) was applied for the calcined samples. The background was subtracted and a baseline correction performed for all spectra. Phase identification was reported with reference to Powder Diffraction Files (PDFs) from the International Centre for Diffraction Data (ICDD) database of powder diffraction patterns.

The key hydrotalcite lattice parameters a ($2 \cdot d_{110}$) and c ($3 \cdot d_{003}$) reported in Paper III, were calculated following the methods described by Rives [126]. The interplanar spacing $d_{110}$ and $d_{003}$ were calculated from the diffraction angles (60.6 and 11.5 degree peaks) following Bragg's Law (see Equation 3.1). Here n, $\lambda$ and $\theta$ are the order of reflection (first order assumed), wavelength of incident X-rays (1.54 Å) and diffraction angle respectively.

$$d = \frac{n \cdot \lambda}{2 \cdot \sin(\theta)} \tag{3.1}$$

The literature values of the hydrotalcite a and c lattice parameters are 0.305 and 2.28 nm [127]. These parameters correspond to the distance between cations inside the double hydroxide layers and three times the interlayer distance respectively.

The mean crystallite domain size (D) reported in Paper III was estimated by the Scherrer equation (see Equation 3.2) based on the diffraction peaks with the highest intensities [128]. Here K is the Scherrer constant (commonly assumed to be 0.9) and m is the full width at half maximum (FWHM).

$$D = \frac{K \cdot \lambda}{m \cdot \cos(\theta)} \tag{3.2}$$

### 3.2.2 XRF

X-ray fluorescence (XRF) was performed on a Rigaku Superminiz00 WDXRF spectrometer. The samples (ca 200 mg) were grinded and pelletized with boric acid (ca 3000 mg) as binder before analysis. The Ni/Co ratios were estimated from K$\alpha$ peak intensities.

### 3.2.3 ICP-MS

Inductively coupled plasma mass spectrometry (ICP-MS) was performed by SINTEF Industry. In Paper I, the samples (calcined precursors) were decomposed with HCl and $HNO_3$ at 250 °C for 10 minutes in a Milestone UltraWAVE microwave oven and analysed with an Agilent 8800 Triple Quadrupole ICP-MS equipped with an SPS 4 Autosampler. In Paper III, the samples were decomposed with $HNO_3$ and analysed with an Agilent 8900 Triple Quadrupole ICP-MS. The Ni, Co, Mg, Al, Pt, Pd and Rh were quantified with respect to standards from Inorganic Ventures, with $^{115}$In as internal standard.

### 3.2.4 $N_2$-physisorption

$N_2$-physisorption was performed with a Micromeritics TriStar 3000 Surface Area and Porosity Analyser. The calcined precursors (ca 200-300 mg) were degassed under vacuum for 1 hour at room temperature and overnight at

100 °C. Adsorption and desorption isotherms were recorded at -196 °C. The surface area was estimated based on the Brunauer-Emmett-Teller (BET) theory [129]. The cumulative pore volume and average pore diameters were determined based on adsorption isotherms in the 1.7-300 nm pore diameter range following Barrett-Joyner-Halenda (BJH) theory [130].

The BET theory is a multi-layer extension of Langmuir adsorption, assuming dynamic equilibrium between adsorbate and adsorptive in any layer, first layer adsorption on equivalent sites, adsorbed molecules in the below layer is the adsorption site for next layer adsorption, interactions between adsorbed molecules are ignored, identical adsorption-desorption conditions for all layers except the first, the adsorption energy equals the condensation energy for all layers except the first, and that the number of multi-layers approach infinity as adsorptive pressure (P) reaches the equilibrium pressure of the condensed gas ($P_0$) [131]. The BET Equation 3.3 can be derived based on these assumptions [129].

$$\frac{\mathrm{P}}{\mathrm{v}(\mathrm{P}_0 - \mathrm{P})} = \frac{1}{\mathrm{v_m} \cdot \mathrm{c}} + \frac{(\mathrm{c}-1)}{\mathrm{v_m} \cdot \mathrm{c}} \cdot \frac{\mathrm{P}}{\mathrm{P}_0} \tag{3.3}$$

Here, v is the total volume adsorbed, $v_m$ is the mono-layer adsorption volume, and c is the BET constant. The surface area is calculated from $v_m$, determined by linear regression, plotting $P/v(P_0-P)$ vs $P/P_0$ (Equation 3.3).

### 3.2.5 $H_2$-chemisorption

The $H_2$-chemisorption was performed with a Micrometrics ASAP 2020 instrument. The calcined catalysts (ca 150 mg) were evacuated for 1 hour at 30 °C and reduced in $H_2$ at 670 °C for 16 hours (10 °C/min heating rate). The samples were further evacuated for 30 min at 670 °C and 1.5 hours at 35 °C before recording the adsorption isotherms. The active metal dispersion ($D_m$) was calculated assuming dissociative $H_2$ adsorption on two active metal cites (stoichiometric factor SF = 2), following Equation 3.4 [132]. Here, $V_m$ is the specific mono-layer adsorption volume (STP basis), and $V_{STP}$ is the ideal gas molar volume (22414 $cm^3$/mol). The molar mass ($M_m$) was calculated as a weighted average of the individual metals. The weight fraction ($w_m$) was included as the total active metal content.

$$\mathrm{D_m} = \frac{\mathrm{V_m} \cdot \mathrm{SF} \cdot \mathrm{M_m}}{\mathrm{V_{STP}} \cdot \mathrm{w_m}} \cdot 100\% \tag{3.4}$$

The mass loss upon pre-reduction was taken into account, assuming complete reduction of $PtO_2$/PdO/$Rh_2O_3$+NiO+CoO+MgO+$Al_2O_3$ to Pt/Pd/Rh+Ni+Co+MgO+$Al_2O_3$. The slightly lower theoretical Ni+Co loading (19.8+19.8 wt%) after noble metal promotion was included. Calculations corrected for the amount of un-reduced Ni/Co (estimated from TPR experiments) were reposted in Paper III. The mean metal particle diameter ($d_m$) were calculated assuming uniform spherical particles, following Equation 3.5 [132].

$$d_m = \frac{6 \cdot v_m}{D_m \cdot a_m} \tag{3.5}$$

The bulk metal atomic volume ($v_m$) and atomic surface area ($a_m$) were included as weighted averages of the literature values (fcc crystal structure).

### 3.2.6 TPR

Temperature-programmed reduction (TPR) experiments were performed with an Altamira BenchCat Hybrid 1000HP. Calcined samples (ca 50 mg) were placed between quartz wool in a quartz reactor (U-shape), pre-dried at 200 °C for 30 minutes (10 °C/min heating rate) in Ar (50 NmL/min) and cooled to 50 °C before the experiment. The samples were heated to 900 °C (10 °C/min heating rate) in 7 mol% $H_2$ in Ar (50 NmL/min). The final temperature was held for 30 min. TPR profiles were recorded as $H_2$ consumption measured with a thermal conductivity detector (TCD).

In Paper III, the TPR experiments were repeated with a 670 °C temperature hold (5 hours). The degree of reduction following activation at 670 °C was estimated based on the peak integration area before and after the end of the 670 °C hold (assuming complete reduction after final 900 °C hold).

## 3.3 Catalyst testing

### 3.3.1 Experimental setup

The experimental setup shown in Figure 3.1 was designed for catalyst testing at relevant bio-syngas model conditions. The setup has been described in Paper I [14]. A technical description is included in Figure 3.2. Catalyst samples (10.0 mg, 75-150 µm) were diluted with $\alpha$-$Al_2O_3$ (400.0 mg). The samples were placed on a quartz filter (150-250 µm pore diameter) inside

a tubular quartz-reactor (see Figure 3.3, bed height = 7-8 mm), and kept in place with a piece of alumina wool (ca 3 mm) above and below the sample. The high amount of inert bed dilution material was applied to minimise deviations from isothermal operation. The bio-syngas contained 10/35/25/25/5 mol% $CH_4/H_2/CO/CO_2/N_2$ (with $N_2$ as internal standard). All gases were fed by Bronkhorst mass-flow controllers (MFCs).

Stable steam supply was provided with an in-house built vaporiser with an MFC feeding DI-water from a water-tank (pressurised with He) through a heating furnace. The Ar feed was used as carrier gas with a double-tube design at the heating furnace inlet (Ar flowing in 1/4" outer tube, with $H_2O$ in 1/16" inner tube). Complete evaporation was secured, preheating the $H_2O$/Ar flow at 250 °C inside the vaporiser (coiled 1/8" tube, length = 10 cm, diameter = 3 cm, windings = 9). All lines downstream of the vaporiser were heated (with heat-tape) and isolated to avoid condensation issues.

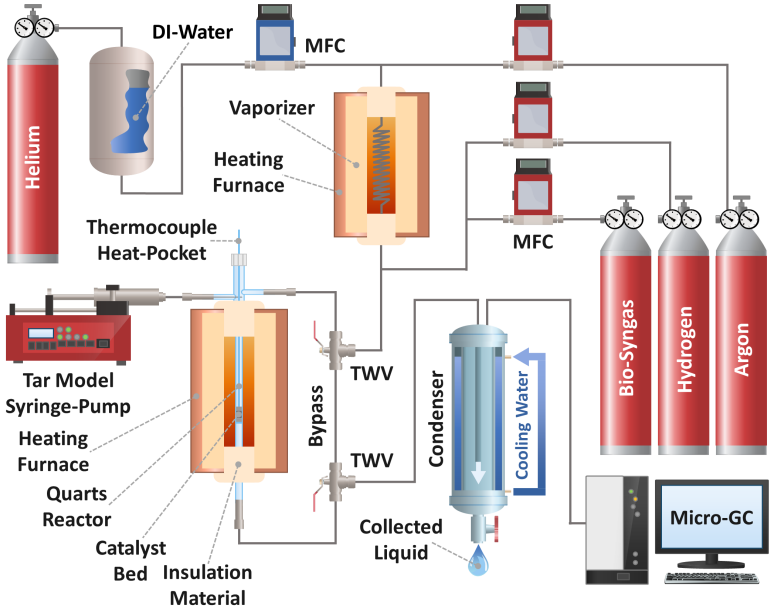


**Figure 3.1:** Schematic illustration of experimental setup for catalyst testing at bio-syngas model conditions. Reproduced from Lysne *et al.* [14].

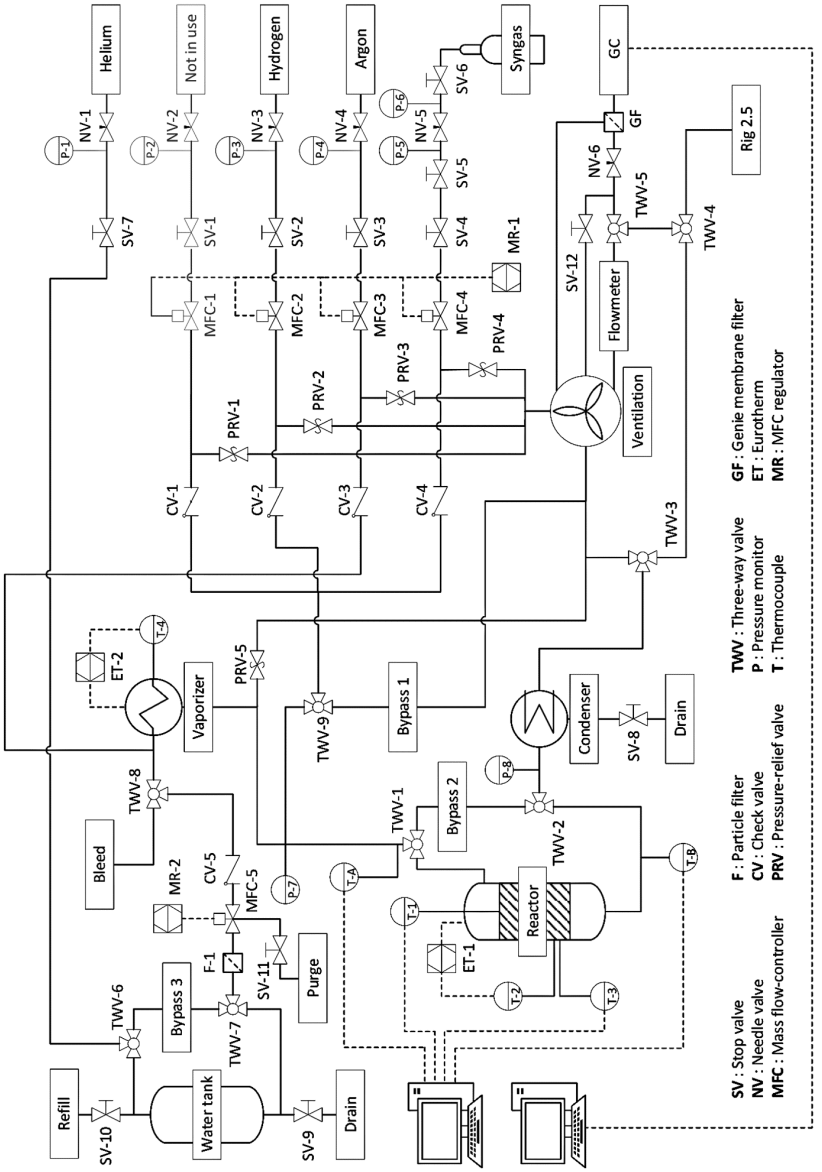


**Figure 3.2:** Technical description of experimental setup for catalyst testing at bio-syngas model conditions (tar syringe-pump not included).

The model tar was injected directly into the reactor centre (through 1/16" tube) with a syringe-pump (NE-1000, 50 mL stainless steel syringe, KD Scientific). The reactor configurations, including the model tar syringe-pump connection point is shown in Figure 3.3.

Condensable liquids were removed before outlet $CH_4/H_2/CO/CO_2/N_2$ composition analysis with an Agilent 490 Micro-GC system (CP-COX column).

The reaction temperature was measured with a thermocouple (type K) in a reactor centre heat-pocket in close contact with the top of the catalyst bed. The heating furnace temperature was controlled with a thermocouple in the reactor side heat-pocket in close contact with the reactor wall.

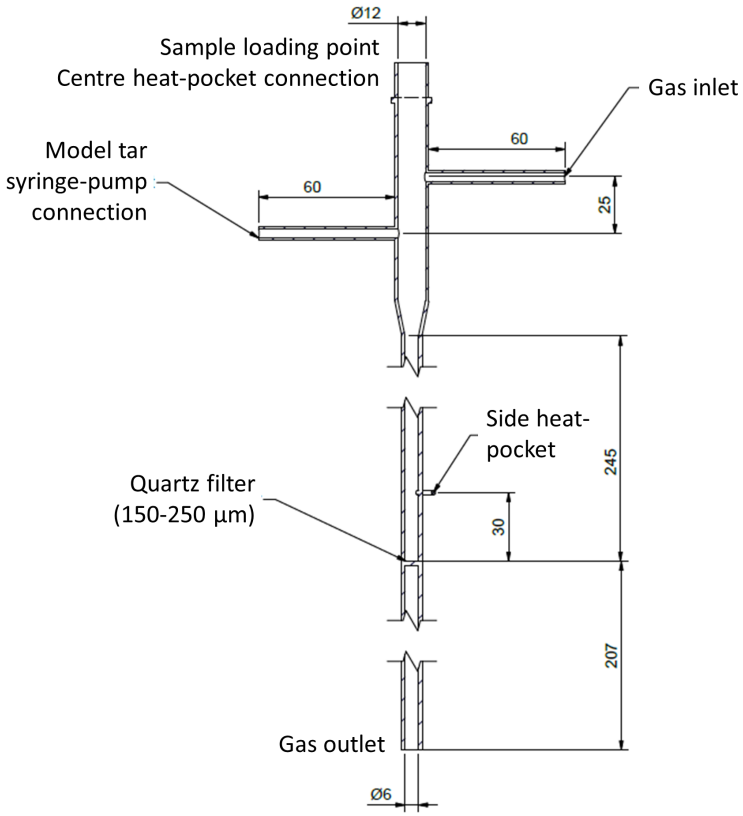


**Figure 3.3:** Technical description (unit = mm) of quartz reactor for catalyst testing at bio-syngas model conditions. Reproduced from Madsen [133].

### 3.3.2 Steam reforming experiments

All samples were reduced in 50 mol% $H_2$ in Ar (200 NmL/min) overnight (16 hours) at 670 °C after pre-heating at 2.0 °C/min prior to the experiments. The reactant flow was stabilised in the reactor bypass before directing the flow to the catalyst bed. The *in situ* activation experiments reported in Paper III were conducted without pre-reduction. The catalysts were heated in Ar (200 NmL/min) overnight (16 hours) at 670 °C (2.0 °C/min heating rate).

All experiments were performed with a constant bio-syngas flow rate (400 NmL/min) and atmospheric pressure. In Paper I-III, the total gas hourly space velocity (GHSV) of 85000 NmL/$g_{cat}$min (including $H_2O$, model tar and Ar balance) was kept constant. The high GHSV was applied targeting low-conversion differential reactor operation. The conversion could however not be further reduced in the current setup (due to high catalyst activity) without compromising the relevance of the operating conditions.

The catalyst stability during hydrocarbon steam reforming was studied with and without the addition of a model tar to the feed. The catalyst activity and deactivation was monitored by $CH_4$ conversion. The effects of temperature (650-800 °C), S/C ratio (2-5, molar hydrocarbon basis), tar loading (10-30 g/$Nm^3$, dry model bio-syngas basis) and model tar composition were studied in Paper II. Table 3.2 shows the tested model tar compositions.

**Table 3.2:** Overview of bio-syngas model tar compositions tested in this work.

| Tar model | Composition (wt%) | | |
|---|---|---|---|
| | Toluene | 1-Methylnaphthalene | Phenol |
| Tar-1 | 100 | 0 | 0 |
| Tar-2 | 75 | 25 | 0 |
| Tar-3 | 70 | 25 | 5 |

Spent catalyst samples were cooled to room temperature in Ar (100 NmL/min) and isolated from the bed dilution material by magnetic separation.

### 3.3.3 Regeneration experiments

In Paper III, the coke gasification potential in tar free bio-syngas was briefly investigated through one and two cycles of tar reforming (2 hours) and tar free catalyst coke gasification (2 hours).

The Switch-SRCG (dual-bed sequential steam reforming and coke gasification) experiments reported in Paper IV were performed with a higher cat-

alyst amount (50.0 mg, 150-250 µm, in 50.0 mg $\alpha$-$Al_2O_3$). The experimental setup was modified to enable coke gasification in a 0.5/50.1/27.6/18.2/3.6 mol% $CH_4/H_2/CO/CO_2/N_2$ bio-syngas (550 NmL/min) to resemble the expected equilibrium conditions following the first steam reforming reactor (T = 700 °C, S/C = 3.0, model tar = 20.0 g/Nm$^3$ toluene). The $H_2O$ flow was reduced by 31.9% during the coke gasification step to account for the water consumption of the $CH_4$/tar reforming and WGS reactions in the first reactor. This corresponds to a total GHSV of 17000 and 18920 NmL/$g_{cat}$min in the reforming and regeneration steps respectively.

### 3.3.4 Condenser sample analysis

The condenser samples were extracted with n-pentane (5-10 mL) and analyzed with an Agilent 7820A GC-FID (VF-Xms column, 60 m × 250 um × 1 um). The quantification of remaining model tar compounds was addressed by standard sample analysis. Peak identification was achieved with an Agilent 7820A GC-MS using the same column.

### 3.3.5 Calculations

The effluent mole fractions ($x_n$) were determined based on calibration of the micro-GC response. The effluent mole flow $F_n$ was calculated following Equation 3.8 by combination of Equation 3.6 and 3.7, considering the bio-syngas internal standard ($N_2$). Here $F_{tot}$ is the total effluent mole flow, and the internal standard mole flow ($F_{N2} = F_{N2,0}$) is assumed to be unchanged.

$$x_n = \frac{F_n}{F_{tot}} \tag{3.6}$$

$$x_{N2} = \frac{F_{N2}}{F_{tot}} = \frac{F_{N2,0}}{F_{tot}} \tag{3.7}$$

$$F_n = \frac{x_n \cdot F_{N2,0}}{x_{N2}} \tag{3.8}$$

The $CH_4$ conversion ($X_{CH4}$) was calculated following Equation 3.9. The product selectivity was evaluated considering the effluent $H_2$/CO and CO/$CO_2$ ratios, defined as $F_{H2}/F_{CO}$ and $F_{CO}/F_{CO2}$ respectively.

$$X_{CH4} = \frac{F_{CH4,0} - F_{CH4}}{F_{CH4,0}} \cdot 100\% \tag{3.9}$$

The turnover frequencies (TOF) reported in Paper III were based on integral reactor calculations. The design equation for packed bed reactors shown in Equation 3.10, is given by the mole balance at steady-state conditions. Here W and $-r_{CH4}$ are the catalyst mass and $CH_4$ reaction rate respectively.

$$F_{CH4,0} \cdot \frac{dX_{CH4}}{dW} = -r_{CH4} \tag{3.10}$$

At low $CH_4$ concentrations (dilute flow), the total mole flow change throughout the reactor can be neglected. The $CH_4$ concentration ($C_{CH4}$) can then be expressed as a function of $CH_4$ conversion following Equation 3.11 (constant temperature and pressure). By assuming a first order reaction with respect to $CH_4$ and zero order to the other components, the reaction rate can be expressed by Equation 3.12, where k is the rate constant.

The reaction order assumptions were based on kinetic studies in previous literature (similar Ni/MgO catalyst system) [134], and supported by operating parameter screening results reported herein (Paper II).

$$C_{CH4} = C_{CH4,0}(1 - X_{CH4}) \tag{3.11}$$

$$-r_{CH4} = k \cdot C_{CH4} = k \cdot C_{CH4,0}(1 - X_{CH4}) \tag{3.12}$$

The integral Equation 3.13 is obtained by combination of Equation 3.10 and 3.12. The integrals are evaluated analytically to obtain Equation 3.14.

$$\int_0^{X_{CH4}} \frac{1}{(1 - X_{CH4})} dX_{CH4} = \frac{k \cdot C_{CH4,0}}{F_{CH4,0}} \int_0^{W} dW \tag{3.13}$$

$$-\ln(1 - X_{CH4}) = \frac{k \cdot C_{CH4,0}}{F_{CH4,0}} \cdot W \tag{3.14}$$

The reaction rate at the reactor inlet can then be expressed by Equation 3.15. Finally, the TOF can be calculated following Equation 3.16.

$$-\mathrm{r_{CH4,0}} = \mathrm{k} \cdot \mathrm{C_{CH4,0}} = -\ln(1 - \mathrm{X_{CH4}}) \cdot \frac{\mathrm{F_{CH4,0}}}{\mathrm{W}} \tag{3.15}$$

$$\mathrm{TOF} = \frac{-\mathrm{r_{CH4,0}} \cdot \mathrm{M_m}}{\mathrm{w_m} \cdot \mathrm{D_m}} \tag{3.16}$$

Here, $M_m$, $w_m$ and $D_m$ are the average molar mass, weight fraction (loading) and dispersion of the active metals respectively.

### 3.3.6 Thermodynamic equilibrium

The equilibrium compositions were calculated in Aspen Plus V9 applying the Peng-Robinson cubic equation of state. The equilibrium $H_2$/CO and CO/$CO_2$ ratios were calculated considering the theoretical $H_2$/CO/$CO_2$/$H_2O$ composition (SMR basis) following the observed $CH_4$ conversion for each individual measurement. The model tar conversion ($X_{tar}$) was assumed to be 100% for these calculations.

### 3.3.7 Empty-reactor tests

Initial empty-reactor tests (at 675-800 °C) were preformed loading the reactor with only $\alpha$-$Al_2O_3$ (200.0 mg), following the experimental procedure described in Section 3.3.2 (S/C = 3.0). The results are reported in Table 3.3.

**Table 3.3:** Results from initial empty-reactor tests (average from 5 measurements, loading = 200.0 mg $\alpha$-$Al_2O_3$, S/C = 3.0, GHSV = 85000 NmL/$g_{cat}$min).

| Temperature (°C) | $X_{CH4}$ (%) (a) | $H_2$/CO (-) (b) | CO/$CO_2$ (-) (c) |
|---|---|---|---|
| 675 | 1.6 | 1.44 | 1.01 |
| 700 | 1.4 | 1.44 | 1.01 |
| 725 | 1.3 | 1.44 | 1.00 |
| 750 | 1.3 | 1.45 | 1.01 |
| 775 | 1.3 | 1.44 | 1.00 |
| 800 | 1.5 | 1.45 | 1.01 |

(a) Standard deviation = 0.1-0.2%.
(b) Standard deviation = 0.004-0.01.
(c) Standard deviation = 0.001-0.009.

The low $CH_4$ conversion and minor deviation from the inlet $H_2/CO$ (1.4) and $CO/CO_2$ (1.0) ratios were considered to be within the inaccuracy of the measurements, indicating negligible SMR and WGS activity as expected.

### 3.3.8 Carbon mass balance

The carbon mass balance ($\Delta C$) was defined as the measured outlet carbon flow rate ($CH_4/CO/CO_2$) vs initial carbon flow ratio (molar). Equation 3.17 shows the calculation of $\Delta C$ with toluene as model tar.

$$\Delta C = \frac{F_{CH4} + F_{CO} + F_{CO2}}{F_{CH4,0} + F_{CO,0} + F_{CO2,0} + 7 \cdot F_{toluene,0}} \cdot 100\% \qquad (3.17)$$

Figure 3.4 shows typical variations in $\Delta C$ and effluent carbon flow rate through 8 hours on stream with and without tar model addition. The tar carbon (0.303 mmol/min for tar = 10.0 g/Nm$^3$ toluene) was well accounted for as $CH_4/CO/CO_2$ in the effluent flow (see Figure 3.4b). The mean $\Delta C$ for all data included in Paper I-IV were 99.0/99.6/99.4/99.5% (1162/1534/1100/197 data points, standard deviation = 0.9-1.8%). The high $\Delta C$ indicated a high quality feed and product analysis control throughout the experiments.

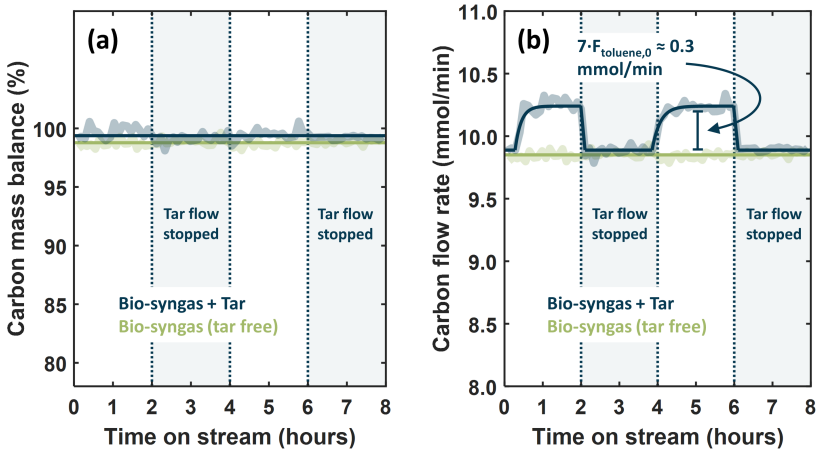


**Figure 3.4:** (a) Carbon mass balance and (b) outlet $CH_4/CO/CO_2$ carbon flow rate (20-20 wt% Ni-Co, T = 700 °C, S/C = 3.0, tar = 10 g/Nm$^3$ toluene).

### 3.3.9 Mass-transfer limitations

The following preliminary theoretical calculations regarding ideal plug-flow behaviour and mass-transfer limitations (calculations at tar free conditions) were based on the approach described by the EUROKIN project [135].

The ideal plug-flow assumption includes negligible radial and axial dispersion. Radial dispersion effects were addressed considering the criteria described by Chu and Ng [136] shown in Equation 3.18, where $d_t$ and $d_p$ are the reactor inner cross section and catalyst particle diameters respectively.

$$\frac{d_t}{d_p} > 8 \tag{3.18}$$

Axial dispersion was similarly evaluated considering the criteria shown in Equation 3.19 following Mears [137] and Gierman [138]. Here, $h_b$ is the bed height, $\alpha$ is the $CH_4$ reaction order, and Bo is the Bodenstein number.

$$\frac{h_b}{d_p} > \frac{8 \cdot \alpha}{Bo} \cdot \ln\left(\frac{1}{1 - X_{CH4}}\right) \tag{3.19}$$

The ideal plug-flow criteria in Equation 3.18 and 3.19 were both satisfied at all conditions reported herein. The Bo number was calculated by Equation 3.20 [139], where $\varepsilon_b$ is the catalyst bed porosity (void fraction within catalyst bed), $D_{CH4,m}$ is the molecular bulk diffusivity of $CH_4$, $\tau_b$ is the catalyst bed tortuosity and $u_0$ is the superficial gas velocity.

$$\frac{1}{Bo} = \frac{\varepsilon_b \cdot D_{CH4,m}}{\tau_b \cdot d_p \cdot u_0} + 0.5 \tag{3.20}$$

The bed tortuosity $\tau_b$ (average fluid flow path through the bed relative to bed height) can be estimated as $1/\sqrt{\varepsilon_b}$ [140]. The bed porosity $\varepsilon_b$ is typically 0.37-0.41 [135], and was set to 0.39 for the preliminary calculations reported herein. The superficial gas velocity $u_0$ was calculated from the inlet total volumetric flow rate at the applied conditions (ideal gas calculations). The molecular bulk diffusivity was estimated following Maestri *et al.* [135], with binary molecular diffusivities from Perry and Green [141].

External mass-transfer limitations were evaluated by the Carberry number (Ca) criteria in Equation 3.21 (spherical particles assumed) [142]. Here, $r_{CH4,v}$ is the volumetric reaction rate (per catalyst unit volume), $k_g$ is the external mass-transfer coefficient and $C_{CH4,b}$ is the $CH_4$ bulk concentration.

$$\mathrm{Ca} = \frac{\mathrm{r_{CH4,v}} \cdot \mathrm{d_p}}{6 \cdot \mathrm{k_g} \cdot \mathrm{C_{CH4,b}}} < \frac{0.05}{\alpha} \tag{3.21}$$

The external mass-transfer coefficient $k_g$ can be calculated from the Sherwood number (Sh) following Equation 3.22 [135], and Sh from Reynolds number (Re) and the Schmidt number (Sc) by Equation 3.23 to 3.25 [139]. Equation 3.23 is reported to be valid for Re values between 0.1 and 100. The external mass-transfer limitation criteria in Equation 3.21 and the Re number criteria were both satisfied at all conditions reported herein.

$$\mathrm{k_g} = \frac{\mathrm{Sh} \cdot \mathrm{D_{CH4,m}}}{\mathrm{d_p}} \tag{3.22}$$

$$\mathrm{Sh} = 2 + 1.1 \cdot \mathrm{Re}^{3/5} \cdot \mathrm{Sc}^{1/3} \tag{3.23}$$

$$\mathrm{Re} = \frac{\mathrm{d_p} \cdot \rho_\mathrm{g} \cdot \mathrm{u_0}}{\mu_\mathrm{g}} \tag{3.24}$$

$$\mathrm{Sc} = \frac{\mu_\mathrm{g}}{\rho_\mathrm{g} \cdot \mathrm{D_{CH4,m}}} \tag{3.25}$$

Here, $\rho_g$ and $\mu_g$ are the gas density and dynamic viscosity. The gas density was calculated by ideal gas law, considering the applied reaction conditions. The dynamic viscosity of the gas mixture can be estimated from the dynamic viscosity of the individual components following Wilke [143].

Internal mass-transfer limitations were evaluated considering the Weisz-Prater criteria for the Weisz-modulus ($\Phi$) shown in Equation 3.26, where $\eta$ and $\phi$ are the effectiveness factor and the Thiele-modulus defined by Equation 3.27 (spherical particles) [135]. Here, $C_{CH4,s}$ and $D_{CH4,eff}$ are the particle surface concentration and the effective diffusivity inside catalyst pores.

$$\Phi = \eta \cdot \phi^2 < 0.08 \tag{3.26}$$

$$\phi = \frac{\mathrm{d_p}}{6} \cdot \sqrt{\frac{\alpha + 1}{2} \cdot \frac{\mathrm{r_{CH4,v}}}{\mathrm{C_{CH4,s}} \cdot \mathrm{D_{CH4,eff}}}} \tag{3.27}$$

In the case of limited external mass-transfer limitations, the surface concentration $C_{CH4,s}$ can be assumed to be equal to the bulk concentration. For first order reactions, $\Phi$ < 0.08, implies that $\eta$ > 0.95, and the deviation from intrinsic kinetics due to intra-particle diffusion limitations is less than 5% [135]. In this case, the Weisz-modulus $\Phi$ is commonly estimated as $\phi^2$, and calculated following Equation 3.28.

$$\Phi \approx \frac{\mathrm{d_p^2} \cdot \mathrm{r_{CH4,v}}}{36 \cdot \mathrm{C_{CH4,b}} \cdot \mathrm{D_{CH4,eff}}} \tag{3.28}$$

The effective pore diffusivity $D_{CH4,eff}$ was calculated from the molecular bulk diffusivity $D_{CH4,m}$ and Knudsen diffusivity $D_{CH4,k}$ by Equation 3.29 [144]. Here, $\varepsilon_p$ and $\tau_p$ are the catalyst particle porosity and pore tortuosity. The Knudsen diffusion describes molecular transport inside catalyst pores where diffusion is limited by molecule-wall (not molecule-molecule) interactions. The Knudsen diffusivity was estimated following Maestri *et al.* [135].

$$\mathrm{D_{CH4,eff}} = \frac{\varepsilon_\mathrm{p}/\tau_\mathrm{p}}{1/\mathrm{D_{CH4,m}} + 1/\mathrm{D_{CH4,k}}} \tag{3.29}$$

The tortuosity was set to 2.0 upon preliminary calculations, based on common values reported by Satterfield [144]. The porosity was similarly set to 0.6 based on Froment and Bischoff [145]. The calculated Weisz-modulus was generally close to the Weisz-Prater criteria for 150 µm catalyst particles. It should be noted that the criteria was not satisfied above 124 and 105 µm for the high-temperature experiments at 750 and 800 °C (Paper II).

An initial temperature screening was performed with the Ni-Co ratio series (with S/C ratio 3.0). Linear Arrhenius-plots were found (see Figure 3.5) in the low-temperature region (650-700 °C), indicating intrinsic kinetic control

[131], as expected from preliminary calculations. Figure 3.5 additionally illustrates the approach to equilibrium as well as experimental repeatability, comparing screening results with initial activity from stability tests.

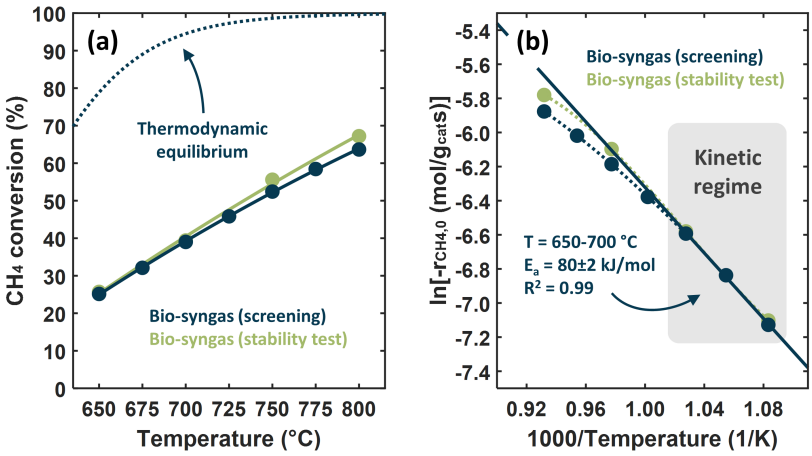


**Figure 3.5:** Temperature screening with (a) activity and (b) Arrhenius-plot (20-20 wt% Ni-Co, S/C = 3.0). Linear low-temperature Arrhenius-plots (650-700 °C) indicate intrinsic kinetic control.

The activation energies ($E_a$) were determined for the Ni-Co ratio samples in the range of 75-89 kJ/mol, based on the 650-700 °C region of the Arrhenius-plots (see Table 3.4). The apparent activation energies were slightly lower than typically values reported for SMR over supported Ni-catalysts in previous literature (96-102 kJ/mol) [134, 146, 147]. Similar activation energies (92-113 kJ/mol) were also found by Wang *et al.* [148] for a series of hydrotalcite-based 12 wt% Ni/Mg(Al)O catalysts.

**Table 3.4:** Activation energies from Arrhenius-plots (650-700 °C, S/C = 3.0).

| Sample | $E_a$ (kJ/mol) | $R^2$-value |
|---|---|---|
| 40 wt% Ni/Mg(Al)O | 89 ± 1 | 1.00 |
| 30-10 wt% Ni-Co/Mg(Al)O | 88 ± 1 | 1.00 |
| 20-20 wt% Ni-Co/Mg(Al)O | 80 ± 2 | 0.99 |
| 10-30 wt% Ni-Co/Mg(Al)O | 75 ± 2 | 0.98 |
| 40 wt% Co/Mg(Al)O | 79 ± 3 | 0.97 |

It should be noted that such studies commonly apply $CH_4/H_2O/H_2$ model systems without the possible effects of high bio-syngas CO and $CO_2$ partial pressures included in the present work. A considerably lower activation energy (56 kJ/mol) was found by Wang *et al.* [149] for dry reforming of methane (DRM) with the same 12 wt% Ni/Mg(Al)O catalyst. Similar values (56-69 kJ/mol) have also been reported for DRM with bi-metallic Ni-Co catalysts [150, 151]. It is reasonable to believe (considering the $CO_2$ rich model bio-syngas) that the reforming activity reported herein result from simultaneous SMR and DRM operation. The observed activation energies were generally considered to be in reasonable agreement with previous literature. The minor deviation from values typically reported in pure SMR kinetic studies shows the importance of studying steam reforming catalysts for bio-syngas cleaning at relevant $H_2/CO/CO_2$ rich conditions.

## 3.4 Coke characterisation

### 3.4.1 Raman spectroscopy

Raman spectroscopy was performed with a Horiba Jobin Yvon LabRAM HR800 system equipped with a visible light laser (633 nm) excitation source. Inelastic Raman scattering (vs elastic Reyleigh scattering) following excitation can provide information about the vibrational modes of the system. The technique is commonly applied for qualitative characterisation of catalyst coke species [102, 152]. The D band (around 1325 $cm^{-1}$) generally indicates the presence of disordered and defective carbon like microcrystalline graphite or unstructured aromatic species. The G band (around 1590 $cm^{-1}$) is attributed to more ordered graphitic structures. The D/G ratio is typically reported as a measure of overall degree of graphitization.

### 3.4.2 TGA-TPO-MS

The thermogravimetric analysis and temperature-programmed oxidation with mass spectrometry (TGA-TPO-MS) reported in Paper I was performed with an Linseis STA PT1600 instrument, heating the recovered spent catalyst samples (5-10 mg) from 150 to 800 °C (5 °C/min) in synthetic air (21 mol% $O_2$ in $N_2$, 140 NmL/min) and Ar (60 NmL/min) after 1 hour of pre-drying at 150 °C in Ar (200 NmL/min). The coke combustion was monitored by $CO_2$ formation with a Pfeiffer Vacuum ThermoStar™ MS detector (m/z = 44).

In Paper II-III, a different TGA-TPO-MS instrument was applied due to technical problems with the first setup. The experiments were performed with a Netzsch STA 449 C instrument heating the spent samples (5-10 mg) from

35 to 900 °C (heating rate 5 °C/min) in synthetic air (21 mol% O2 in N2, 55 NmL/min) and Ar (25 NmL/min). The coke combustion was monitored by $CO_2$ formation with a Netzsch QMS 403 C MS detector (m/z = 44). For the low-coking samples, the low coke amounts (combined with low sample amounts) were considered to be below the detection limit of the gravimetric measurements. The coke carbon quantities were estimated from the $CO_2$ formation curves by calibration of the MS-detector, considering the thermal decomposition of calcium oxalate monohydrate (third degradation step: $CaCO_3 \rightarrow CaO + CO_2$). The MS calibration curve is shown in the support material of Paper II, with a proportional peak area response ($R^2$ = 0.9997) in a broad $CO_2$ formation range. This approach avoids the common issue with metal oxidation potentially masking the coke combustion mass change generally associated with gravimetric coke analysis.

In Paper IV, TPO-MS experiments were performed at the same conditions with a third setup (Netzsch STA 449 C with a Netzsch QMS 403 C MS detector) due to technical problems with the second instrument.

### 3.4.3 STEM/EDS

The scanning transmission electron microscopy (STEM) and energy dispersive X-ray spectroscopy (EDS) were performed with an ultra-high resolution Hitachi SU9000 STEM instrument. The samples were dispersed in ethanol and drop-casted onto plasma cleaned diced silicon wafers. Elemental mapping was performed with an Oxford Ultim Extreme EDS detector.

# 4 Summary of scientific investigations

The following sections provide brief summaries of the scientific investigations and key findings in the papers included in the thesis. Comprehensive descriptions are provided in the full Papers found in Appendix A-D.

## 4.1 Paper I: Ni-Co ratio effects

Hydrotalcite-derived Ni-Co/Mg(Al)O catalysts with different Ni-Co ratios (40-0, 30-10, 20-20, 10-30 and 0-40 wt%) were prepared based on the method described by He *et al.* [13]. The fresh catalyst samples were characterised by XRD, ICP-MS, $N_2$-physisorption, $H_2$-chemisorption and TPR. The fresh catalyst characterisation was in agreement with previous reports.

Efficient Ni-Co alloy formation was suggested by a gradually shifting Ni/Co d-spacing upon XRD analysis with reduced and passivated samples (see Appendix A, Figure 2). Ni-Co ratios close to target values were found both at a bulk level (by ICP-MS) and at a single metal particle level by STEM/EDS elemental analysis point scan.

The catalysts were tested for steam reforming of biomass gasification tar impurities at model conditions (10/35/25/25 mol% $CH_4/H_2/CO/CO_2$, 5 mol% $N_2$ as internal standard, Ar balance, bio-syngas flow = 400 NmL/min, GHSV = 85000 NmL/$g_{cat}$min, 700 °C, S/C = 3.0), with and without model tar addition (10 g/$Nm^3$ toluene). Post-run coke characterisation was addressed by TGA-TPO-MS, Raman spectroscopy and STEM. The high Ni-Co ratio samples showed the highest initial activity. At tar free conditions, coke free operation was obtained with all samples. All catalysts were shown to provide complete tar elimination, at the expense of deactivation by coke formation. The activity was monitored by $CH_4$ conversion through 8 hours on stream.

Strong deactivation was observed during tar reforming with the monometallic Ni catalyst, accompanied by a high coke formation (19.2 wt%, 8 hours on stream) and a high-temperature shift of the TGA-TPO-MS coke combustion $CO_2$ formation band (see Appendix A, Figure 4a). The 30-10 wt% Ni-Co sample showed enhanced stability, accompanied by increasing coke deposition (36.5 wt%). The effect was proposed to follow a reduced formation of strongly deactivating encapsulating coke by efficient removal of surface carbon coke precursors at the expense of enhanced carbon filament growth. Lower Ni-Co ratios were shown to effectively reduce the coke formation (10.6/4.9/1.2 wt% for 20-20/10-30/0-40 wt% Ni-Co) at the expense of the higher initial activity associated with the high Ni-Co ratio cat-

alysts. Encapsulating coke species, carbon filaments and fused filament clusters were identified by STEM. Restructuring of carbon filament clusters was proposed as an additional route to encapsulating coke species with potential long-term deactivation effects. The higher coke deposition with 30-10 wt% Ni-Co was accompanied by a broader filament diameter distribution (observed by STEM), suggesting a changing filament growth initiation threshold and/or filament growth rate. The coke formation effects were proposed to depend on both Ni-Co ratio and metal particle size.

The potential benefits of the bi-metallic Ni-Co/Mg(Al)O system in bio-syngas tar steam reforming was clearly demonstrated. The results contribute to the understanding of the highly attractive resistance towards deactivation by coke formation associated with Ni-Co catalyst systems. The intermediate Ni-Co ratio system provides a compromise between coke formation resistance associated with high Co samples and the higher initial activity of high Ni catalysts. The intermediate 20-20 wt% Ni-Co system was selected for further operating parameter screening, targeting coke free operation.

## 4.2 Paper II: Key operating parameters

The effects of key operating parameters in steam reforming of biomass gasification tar impurities were investigated at model bio-syngas conditions (10/35/25/25 mol% $CH_4/H_2/CO/CO_2$, 5 mol% $N_2$ as internal standard, Ar balance, bio-syngas flow = 400 NmL/min, GHSV = 85000 NmL/$g_{cat}$min). The performance of the 20-20 wt% Ni-Co/Mg(Al)O catalyst was tested with and without model tar addition (10 g/$Nm^3$ toluene), in a broad range of temperature (650-800 °C) and steam (S/C ratio = 2-5) conditions. The effects of tar loading (10-30 g/$Nm^3$ toluene) and model tar composition (Tar-1 = 100/0/0, Tar-2 = 75/25/0 and Tar-3 = 70/25/5 wt% toluene/1-methylenaphthalene/phenol) were also studied. Complete tar elimination was achieved at all tested conditions, and catalyst deactivation was monitored by $CH_4$ conversion throughout 8 hours on stream. The coke formation was characterised by TGA-TPO-MS and Raman spectroscopy following steam reforming operation. Selected samples were additionally analysed by STEM/EDS.

At tar free conditions, only soft coke A (combustion peak maximum at 225-316 °C) were found (0.5-1.4 wt%). The type A coke was not observed in Raman spectroscopy, and attributed to small amounts of undeveloped surface carbon. In the presence of tar, additional hard coke formation could not be completely avoided at any conditions tested. Two broad hard coke combustion bands B1.1/B1.2 (at 342-381 °C) and B2 (at 475-523 °C) with a high-temperature shoulder peak B3 (at 576-593 °C) were identified (see

Appendix B, Figure 3). A coke formation/classification scheme was proposed, including adsorbed surface carbon species (type A), initial scattered carbon filaments (type B1.1), filament clusters and fused filaments (type B2), and strongly deactivating bulk encapsulating coke (type B3) forming through progressive filament cluster graphitization (see Appendix B, Figure 8). The formation of strongly deactivating metal particle encapsulating coke (type B1.2) was additionally observed in the presence of Tar-2 (high-molecular-weight tar). A critical low-temperature limit was found around 650 °C, where rapid deactivation was accompanied by increasing hard coke amounts. This was similarly the case upon high Tar-1 loading (20-30 g/$Nm^3$). No critical low S/C ratio limit was found within the tested range. The presence of phenol (Tar-3) showed little effect on deactivation and coke deposition. At high-temperature conditions (750-800 °C), the formation of B3 hard coke was effectively suppressed. At high-steam conditions (S/C ratio = 5), a coke selectivity shift from B2/B3 towards B1.1 hard coke was observed. A dynamic temperature/steam effect on carbon filament diameters was suggested, where the overall filament size distribution result from metal particle size availability (sintering effects) and filament size selectivity (filament growth initiation threshold).

Simultaneous adjustment of $H_2$/CO/$CO_2$ ratios, preparing the bio-syngas for downstream Fischer-Tropsch applications, was demonstrated by efficient WGS equilibration at relevant high-temperature conditions.

Catalyst regeneration by coke gasification (2 hours) in the bio-syngas environment was briefly investigated, demonstrating effective removal of hard coke species at tar free conditions (following 2 hours of tar reforming).

## 4.3 Paper III: Noble metal promotion

The effects of noble metal promotion (1.0 wt% Pt/Pd/Rh), Ni+Co loading (20-40 wt%) and calcination temperature (600-800 °C) were investigated within the Ni-Co/Mg(Al)O catalysts system. The Ni/Co ratio (1/1) was kept constant for all samples. The fresh catalyst samples were characterised by XRD, ICP-MS, XRF, $N_2$-physisorption, $H_2$-chemisorption and TPR. All noble metals were found to assist Ni/Co reduction (low-temperature shifted TPR profiles), with Rh > Pt/Pd (see Appendix C, Figure 2e). The final degree of reduction after activation at 670 °C (estimated from TPR analysis) was however found to be similar for all Pt/Pd/Rh-promoted and un-promoted 40NiCo samples (96-97%). The degree of reduction was found to result from the amount of hard-to-reduce Ni/Co, mainly increasing upon higher-temperature calcination. The effect was proposed to be associated with

restricted Mg(Ni,Co,Al)O active metal extraction due to a larger crystallite domain size of the calcined precursor (from XRD) following calcination at higher temperatures (see Appendix C, Figure 3). $H_2$-chemisorption results (corrected by TPR degree of reduction) indicated a Ni+Co loading threshold (above 30 wt%), below which small mean Ni/Co metal particle diameters were obtained (5.1-5.8 nm for all 20NiCo/30NiCo calcined at 600-800 °C). The lower dispersion of the 40NiCo samples (8.8-10.9 nm mean metal particle size) was found to coincide with the formation of spinel-type structures (observed by XRD). The results suggest the extraction of Ni/Co from the Mg(Ni,Co,Al)O periclase precursor to be beneficial for high-dispersion metal particle formation in the reduction step.

The catalysts were tested for steam reforming of biomass gasification tar impurities at model conditions (10/35/25/25 mol% $CH_4/H_2/CO/CO_2$, 5 mol% $N_2$ as internal standard, Ar balance, bio-syngas flow = 400 NmL/min, GHSV = 85000 NmL/$g_{cat}$min, 700 °C, S/C = 3.0) with and without model tar addition (75/25 wt% toluene/1-methylenaphthalene, 10 g/$Nm^3$). Complete tar elimination was achieved with all samples, and catalyst deactivation was monitored by $CH_4$ conversion (through 6 hours on stream). The effects of noble metal promotion on bio-syngas *in situ* activation performance was tested at tar free conditions, with *in situ* activation rates following Rh-40NiCo > Pt-40NiCo > Pd-40NiCo > 40NiCo (see Appendix C, Figure 6). The trend was explained by Pt/Pd/Rh spillover effects following $CH_4$, $H_2$ and/or CO activation, but could not be further distinguished based on the present results.

Spent catalyst coke characteristics were investigated by TPO-MS and Raman spectroscopy. Similar type A (0.8-1.7 wt%), B1 (2.9-5.3 wt%) and B2 (0.6-1.8 wt%) coke distributions were found in all samples. Small amounts of type B3 coke (0.6 wt%) was only observed in the Pd-40NiCo catalyst, accompanied by a slightly decreasing carbon band D/G ratios in Raman spectroscopy (to 1.65) compared to the other 40NiCo samples (1.81-2.18). The high-dispersion 20NiCo/30NiCo samples calcined at 600-700 °C were strongly deactivated through model tar high-coordination active site inhibition and coke formation effects. The effect was found to be accompanied by decreasing D/G ratios (20NiCo: 0.48 and 30NiCo: 1.10-1.31), suggesting a higher overall degree of graphitization associated with the strongly deactivating high-coordination site coke species formed in the 20NiCo/30NiCo catalysts calcined at 600-700 °C. High-temperature calcination (800 °C) was found to reduce the strong deactivation effects observed with the other small-diameter metal particle samples (see Appendix C, Figure 5c), accompanied by a higher post-run coke characterisation D/G ratio (2.21). The effect was proposed to result from increasing coke and/or coke precursor

gasification rates assisted by Mg(Al)O support basic sites. Enhanced activity accompanied by strong tar active site inhibition effects were found for the Rh-40NiCo catalyst (see Appendix C, Figure 5a-b). Pt/Pd/Rh-promotion did not considerably affect deactivation by coke formation.

## 4.4 Paper IV: Switch-SRCG

The Switch-SRCG dual-bed design (see Appendix D, Figure 1) provides continuous on-stream catalyst coke removal by gasification following steam reforming of biomass gasification tars. The first steam reforming (SR) catalyst bed, removing tar impurities (at the expense of coke formation), provides clean bio-syngas for downstream regeneration of the second bed through coke gasification (CG). The two beds switch between SR and CG operation assisted by two 4-port valves. The concept represents a novel approach to net low-coking bio-syngas tar reforming.

The Switch-SRCG concept was tested with a Ni and Ni-Co catalyst (40 wt% Ni/Mg(Al)O and 20-20 wt% Ni-Co/Mg(Al)O), through two cycles of reforming and regeneration (2+2 hours of SR), compared with SR-operation only (4 hours). The SR-step was performed in a model bio-syngas (10/35/25/25 mol% $CH_4/H_2/CO/CO_2$, 5 mol% $N_2$ as internal standard, Ar balance, bio-syngas flow = 400 NmL/min, GHSV = 17000 NmL/$g_{cat}$min, 700 °C, S/C = 3.0, model tar = 20 g/$Nm^3$ toluene). The CG-step was performed in a different bio-syngas (0.5/50.1/27.6/18.2 mol% $CH_4/H_2/CO/CO_2$, 3.6 mol% $N_2$ as internal standard, Ar balance, bio-syngas flow = 550 NmL/min, GHSV = 18920 NmL/$g_{cat}$min, 700 °C, steam reduced by 31.9%) to resemble the expected equilibrium conditions following the SR-reactor. Post-run coke characterisation was performed by TPO-MS and Raman spectroscopy.

Switch-SRCG operation was shown to reduce the coke deposition with both catalysts (see Appendix D, Figure 3). The lowest coke amounts after SR (2.0 wt%) and Switch-SRCG operation (0.9 wt%) were obtained with the Ni-Co catalyst. The high Switch-SRCG performance of the Ni catalyst (in terms of high carbon deposition during SR-operation, effectively removed in the CG-step) should also be highlighted (5.8 vs 1.3 wt% with SR vs Switch-SRCG). The best performance obtained with the Ni-Co system, was attributed to a better balance between coke deposition and coke gasification rates during SR- and CG-operation respectively (compared to Ni). The experimental results demonstrate the potential of the Switch-SRCG dual-bed design providing continuous on-stream catalyst regeneration by coke gasification.

# 5 Conclusion and future work

Hydrotalcite-derived Ni-Co/Mg(Al)O catalysts with a range of different Ni-Co ratios, Ni+Co loading, calcination temperatures and noble metal promotion (Pt/Pd/Rh) were prepared, targeting low-coking steam reforming of biomass gasification tar impurities. All catalysts were tested through experimental studies with model tar components. The effects of key operating parameters, including temperature, steam concentration, tar loading and model tar composition, were additionally investigated.

The potential benefits of bi-metallic Ni-Co/Mg(Al)O catalysts in steam reforming of biomass gasification tar impurities was clearly demonstrated (Paper I). Ni-Co alloy formation was shown by XRD and STEM/EDS analysis. Intermediate Ni-Co ratios provide a suitable compromise between coke formation resistance associated with low Ni-Co ratios and the higher initial activity of high Ni-Co ratio catalysts. However, in the presence of model tar components, catalyst deactivation by coke deposition could not be completely avoided at any conditions tested in this work. The post-run coke characterisation results contribute to the understanding of the highly attractive resistance towards deactivation by coke formation associated with Ni-Co catalyst systems. A coke classification system was proposed, based on characteristic TPO-MS coke combustion temperatures (Paper II). Critical low-temperature (around 650 °C) and tar loading limits (below 20 g/Nm$^3$) were identified, below/above which rapid deactivation by coke formation was observed (20-20 wt% Ni-Co sample).

Noble metal promotion was shown to enhance bio-syngas *in situ* activation performance, with Rh > Pt > Pd (Paper III). Such properties are highly attractive upon cyclic catalyst regeneration by coke combustion/gasification (avoiding additional reduction steps). Pt/Pd/Rh-promotion did not considerably affect deactivation by coke formation. A critical Ni+Co loading limit was found (above 30 wt% Ni+Co), below which high dispersion metal particles were obtained (Paper III). Strong deactivation by high-coordination active site tar inhibition and coke formation effects were observed with the high-dispersion samples. High-temperature calcination (800 °C) was found to reduce the strong deactivation effects associated with small-diameter metal particles, proposed to result from increasing coke and/or coke precursor gasification rates assisted by Mg(Al)O support basic sites.

The potential of the Switch-SRCG (cyclic steam reforming and coke gasification) dual-bed design was demonstrated, reducing overall coke deposition with both Ni and Ni-Co catalysts (Paper IV). The concept provides contin-

uous on-stream catalyst regeneration, representing a novel approach to net low-coking tar reforming. Based on the experimental results reported herein, the following topics are suggested for future work.

- Catalyst deactivation by coke formation could not be avoided in the presence of model tar at any conditions tested herein. The future of Ni-based tar reforming catalysts may hereby rely on cyclic regeneration schemes like the Switch-SRCG dual-bed design. The coke gasification approach (endothermic) is expected to provide a more gentle coke removal, avoiding catalyst degradation by hot-spot formation associated with coke combustion (exothermic). Future investigations considering factors like operating temperature, steam concentration and switching rate is recommended for the Switch-SRCG concept. The long-term stability (and net coke deposition) should also be addressed.
- The biomass gasification agent flow could also be utilised for catalyst regeneration, similarly providing on-stream coke removal, feeding the gasified coke carbon back into the biomass gasifier. Effects of gasification agent $H_2O/O_2/Air/CO_2$ composition on coke gasification rates is suggested for future studies. The high bio-syngas *in situ* activation performance obtained by Rh-promotion is highly attractive following more oxidative regeneration conditions (avoiding additional reduction steps).
- Testing of such regeneration schemes at real gasifier conditions is generally recommended, in order to fully include the potential implications of fluctuating $CH_4/C_2H_x/H_2/CO/CO_2/H_2O$ product gas compositions, complex tar mixtures (including three-ring/four-ring/phenolic/heterocyclic components) as well as volatile inorganic impurities.
- The strong deactivation observed with high-dispersion Ni-Co samples reported herein, suggests high-coordination active sites to be particularly susceptible towards tar inhibition and coke formation effects. Selective inhibition of high-coordination step-sites is suggested for future investigations. Impregnation with small amounts of K, S or Au, shown to be preferentially located at step-sites (Ni catalysts) [96], are considered to be promising candidates from previous literature.
- High-temperature calcination was proposed to increase coke gasification rates assisted by Mg(Al)O support basic sites, in accordance with recent literature [117]. Further investigations with higher calcination temperatures (800-1000 °C) is considered to be highly interesting. Characterisation of catalyst basic sites by $CO_2$-TPD (temperature-programmed desorption) is additionally suggested for future studies.

# References


[1] *WMO Provisional State of the Global Climate 2022*; tech. rep.; World Meteorological Organization (WMO), 2022.

[2] *Emissions Gap Report 2022: The Closing Window - Climate crisis calls for rapid transformation of societies*; tech. rep.; Nairobi: United Nations Environment Programme (UNEP), 2022.

[3] *Climate Change 2022: Mitigation of Climate Change - Working Group III Contribution to the Sixth Assessment Report of the Intergovernmental Panel on Climate Change*; tech. rep.; Intergovernmental Panel on Climate Change (IPCC), 2022.

[4] *Net Zero by 2050: A Roadmap for the Global Energy Sector*; tech. rep.; Paris: International Energy Agency (IEA), 2021.

[5] Chu, S.; Majumdar, A. Opportunities and challenges for a sustainable energy future. *Nature* **2012**, *488*, 294–303.

[6] Guo, M.; Song, W.; Buhain, J. Bioenergy and biofuels: History, status and perspective. *Renew. Sustain. Energy Rev.* **2015**, *42*, 712–725.

[7] Butterman, H. C.; Castaldi, M. J. $CO_2$ as a Carbon Neutral Fuel Source via Enhanced Biomass Gasification. *Environ. Sci. Technol.* **2009**, *43*, 9030–9037.

[8] Mathimani, T.; Pugazhendhi, A. Utilization of algae for biofuel, bio-products and bio-remediation. *Biocatal. Agric. Biotechnol.* **2019**, *17*, 326–330.

[9] Rauch, R.; Kiennemann, A.; Sauciuc, A. In *The Role of Catalysis for the Sustainable Production of Bio-fuels and Bio-chemicals*, Triantafyllidis, K. S., Lappas, A. A., Stöcker, M., Eds.; Elsevier B.V.: Oxford, 2013; Chapter 12, pp 397–443.

[10] Huber, G. W.; Iborra, S.; Corma, A. Synthesis of Transportation Fuels from Biomass: Chemistry, Catalysts, and Engineering. *Chem. Rev.* **2006**, *106*, 4044–4098.

[11] Guan, G.; Kaewpanha, M.; Hao, X.; Abudula, A. Catalytic steam reforming of biomass tar: Prospects and challenges. *Renew. Sustain. Energy Rev.* **2016**, *58*, 450–461.

[12] Li, D.; Tamura, M.; Nakagawa, Y.; Tomishige, K. Metal catalysts for steam reforming of tar derived from the gasification of lignocellulosic biomass. *Bioresour. Technol.* **2015**, *178*, 53–64.

[13] He, L.; Berntsen, H.; Ochoa-Fernández, E.; Walmsley, J. C.; Blekkan, E. A.; Chen, D. Co-Ni Catalysts Derived from Hydrotalcite-Like Materials for Hydrogen Production by Ethanol Steam Reforming. *Top. Catal.* **2009**, *52*, 206–217.

[14] Lysne, A.; Madsen, K. Ø.; Antony J. Rout, K. R.; Blekkan, E. A. Effects of Ni-Co Ratio on Deactivation and Coke Formation in Steam Reforming of Hydrocarbon Impurities from Biomass Gasification with Ni-Co/Mg(Al)O Catalysts. *Chem. Eng. Trans.* **2022**, *92*, 37–42.

[15] Fermoso, J.; Rudiera, F.; Chen, D. Sorption enhanced catalytic steam gasification process: a direct route from lignocellulosic biomass to high purity hydrogen. *Energy Environ. Sci.* **2012**, *5*, 6358–6367.

[16] Takehira, K. "Intelligent" reforming catalysts: Trace noble metal-doped Ni/Mg(Al)O derived from hydrotalcites. *J. Nat. Gas Chem.* **2009**, *18*, 237–259.

[17] Schulz, H. Short history and present trends of Fischer-Tropsch synthesis. *Appl. Catal. A: Gen.* **1999**, *186*, 3–12.

[18] Leckel, D. Diesel Production from Fischer-Tropsch: The Past, the Present, and New Concepts. *Energy Fuels* **2009**, *23*, 2342–2358.

[19] Guettel, R.; Kunz, U.; Turek, T. Reactors for Fischer-Tropsch Synthesis. *Chem. Eng. Technol.* **2008**, *31*, 746–754.

[20] Zennaro, R.; Ricci, M.; Bua, L.; Querci, C.; Carnelli, L.; d'Arminio Monforte, A. In *Greener Fischer-Tropsch Processes for Fuels and Feedstocks*, Maitlis, P. M., de Klerk, A., Eds.; Wiley-VCH: Weinheim, 2013; Chapter 2, pp 19–49.

[21] Ail, S. S.; Dasappa, S. Biomass to liquid transportation fuels via Fischer Tropsch synthesis - Technology review and current scenario. *Renew. Sustain. Energy Rev.* **2016**, *58*, 267–286.

[22] Spath, P. L.; Dayton, D. C. *Preliminary Screening - Technical and Economic Assessment of Synthesis Gas to Fuels and Chemicals with Emphasis on the Potential for Biomass-Derived Syngas*; tech. rep. NREL/TP-510-34929; National Renewable Energy Laboratory, U.S. Department of Energy, 2003.

[23] Wender, I. Reactions of synthesis gas. *Fuel Process. Technol.* **1996**, *48*, 189–297.

[24] Koido, K.; Iwasaki, T. In *Lignin - Trends and Applications*, Poletto, M., Ed.; InTech: Rijeka, 2018; Chapter 7, pp 161–180.

[25] Ruiz, J. A.; Juárez, M. C.; Moralees, M. P.; Muñoz, P.; Mendívil, M. A. Biomass gasification for electricity generation: Review of current technology barriers. *Renew. Sustain. Energy Rev.* **2013**, *18*, 174–183.

[26] Rios, M. L. V.; González, A. M.; Lora, E. E. S.; del Olmo, O. A. A. Reduction of tar generated during biomass gasification: A review. *Biomass Bioenergy* **2018**, *108*, 345–370.

[27] Ravi, M. R.; Kohli, S. In *Coal and Biomass Gasification - Recent Advances and Future Challenges*, De, S., Agarwal, A. K., Moholkar, V. S., Thallada, B., Eds.; Springer: Singapore, 2018; Chapter 2, pp 37–62.

[28] Hofbauer, H.; Rauch, R.; Ripfel-Nitsche, K. *Report on Gas Cleaning for Synthesis Applications - Work Package 2E: Gas treatment*; tech. rep. 2E-3; Institute of Chemical Engineering, Vienna University of Technology, 2007.

[29] Stevens, D. J. *Hot Gas Conditioning: Recent Progress With Larger-Scale Biomass Gasification Systems - Update and Summary of Recent Progress*; tech. rep. NREL/SR-510-29952; National Renewable Energy Laboratory, U.S. Department of Energy, 2001.

[30] Sikarwar, V. S.; Zhao, M.; Clough, P.; Yao, J.; Zhong, X.; Memon, M. Z.; Shah, N.; Anthony, E. J.; Fennell, P. S. An overview of advances in biomass gasification. *Energy Environ. Sci.* **2016**, *9*, 2939–2977.

[31] Milne, T. A.; Evans, R. J. *Biomass Gasifier Tars: Their Nature, Formation and Conversion*; tech. rep. NREL/TP-570-25357; National Renewable Energy Laboratory, U.S. Department of Energy, 1998.

[32] Heidenreich, S.; Foscolo, P. U. New concepts in biomass gasification. *Prog. Energy Combust. Sci.* **2015**, *46*, 72–95.

[33] Couto, N.; Rouboa, A.; Silva, V.; Monteiro, E.; Bouziane, K. Influence of the biomass gasification process on the final composition of syngas. *Energy Procedia* **2013**, *36*, 596–606.

[34] Zhang, Y.; Wan, L.; Guan, J.; Xiong, Q.; Zhang, S.; X., J. A Review on Biomass Gasification: Effect of Main Parameters on Char Generation and Reaction. *Energy Fuels* **2020**, *34*, 13438–13455.

[35] Tezer, Ö.; Karabağ, N.; Öngen, A.; Çolpan, C. Ö.; Ayol, A. Biomass gasification for sustainable energy production: A review. *Int. J. Hydrog. Energy* **2022**, *47*, 15419–15433.

[36] Chanavath, K. N.; Shah, K.; Islam, M. S.; Ronte, A.; Parthasarathy, R.; Bhargava, S. K.; Bankupalli, S. Experimental investigations on entrained flow gasification of Torrefied Karanja Press Seed Cake. *J. Environ. Chem. Eng.* **2018**, *6*, 1242–1249.

[37] Lian, Z.; Wang, Y.; Zhang, X.; Yusuf, A.; Famiyeh, L.; Murindababisha, D.; Jin, H.; Liu, Y.; He, J.; Wang, Y.; Yang, G.; Sun, Y. Hydrogen Production by Fluidized Bed Reactors: A Quantitative Perspective Using the Supervised Machine Learning Approach. *J.* **2021**, *4*, 266–287.

[38] Shahabuddin, M.; Alam, M. T.; Krishna, B. B.; Bhaskar, T.; Perkins, G. A review on the production of renewable aviation fuels from the gasification of biomass and residual wastes. *Bioresour. Technol.* **2020**, *312*, 123596.

[39] Puig-Arnavat, M.; Bruno, J. C.; Coronas, A. Review and analysis of biomass gasification models. *Renew. Sustain. Energy Rev.* **2010**, *14*, 2841–2851.

[40] Van der Drift, A.; van Doorn, J.; Vermeulen, J. W. Ten residual biomass fuels for circulating fluidized-bed gasification. *Biomass Bioenergy* **2001**, *20*, 45–56.

[41] Lv, P.; Chang, J.; Xiong, Z.; Huang, H.; Wu, C.; Chen, Y. Biomass Air-Steam Gasification in a Fluidized Bed to Produce Hydrogen-Rich Gas. *Energy Fuels* **2003**, *17*, 677–682.

[42] Herguido, J.; Corella, J.; González-Saiz, J. Steam Gasification of Lignocellulosic Residues in a Fluidized Bed at a Small Pilot Scale. Effect of the Type of Feedstock. *Ind. Eng. Chem. Res.* **1992**, *31*, 1274–1282.

[43] Gil, J.; Aznar, M. P.; Caballero, M. A.; Francés, E.; Corella, J. Biomass Gasification in Fluidized Bed at Pilot Scale with Steam-Oxygen Mixtures. Product Distribution for Very Different Operating Conditions. *Energy Fuels* **1997**, *11*, 1109–1118.

[44] Xue, P.; Chen, T.; Huang, X.; Hu, Q.; Hu, J.; Zhang, H.; Yang, H.; Chen, H. Prediction of syngas properties of biomass steam gasification in fluidized bed based on machine learning method. *Int. J. Hydrog. Energy* **2023**, in press.

[45] Klass, D. L., *Biomass for Renewable Energy, Fuels and Chemicals*; Academic Press: San Diego, 1998.

[46] Demirbas, A. Combustion characteristics of different biomass fuels. *Prog. Energy Combust. Sci.* **2004**, *30*, 219–230.

[47] McKendry, P. Energy production from biomass (part 1): overview of biomass. *Bioresour. Technol.* **2002**, *83*, 37–46.

[48] Li, X. T.; Grace, J. R.; Lim, C. J.; Watkinson, A. P.; Chen, H. P.; Kim, J. R. Biomass gasification in a circulating fluidized bed. *Biomass Bioenergy* **2004**, *26*, 171–193.

[49] Molino, A.; Chianese, S.; Musmarra, D. Biomass gasification technology: The state of the art overview. *J. Energy Chem.* **2016**, *25*, 10–25.

[50] McKendry, P. Energy production from biomass (part 3): gasification technologies. *Bioresour. Technol.* **2002**, *83*, 55–63.

[51] Shen, Y.; Yoshikawa, K. Recent progresses in catalytic tar elimination during biomass gasification or pyrolysis - A review. *Renew. Sustain. Energy Rev.* **2013**, *21*, 371–392.

[52] Göransson, K.; Söderlind, U.; He, J.; Zhang, W. Review of syngas production via biomass DFBGs. *Renew. Sustain. Energy Rev.* **2011**, *15*, 482–492.

[53] Anis, S.; Zainal, Z. A. Tar reduction in biomass producer gas via mechanical, catalytic and thermal methods: A review. *Renew. Sustain. Energy Rev.* **2011**, *15*, 2355–2377.

[54] Wolf, E. E.; Alfani, F. Catalyst Deactivation by Coking. *Cat. Rev. - Sci. Eng.* **1982**, *24*, 329–371.

[55] Li, C.; Suzuki, K. Tar property, analysis, reforming mechanism and model for biomass gasification - An overview. *Renew. Sustain. Energy Rev.* **2009**, *13*, 594–604.

[56] Coll, R.; Salvadó, J.; Farriol, X.; Montané, D. Steam reforming model compounds of biomass gasification tars: conversion at different operating conditions and tendency towards coke formation. *Fuel Process. Technol.* **2001**, *74*, 19–31.

[57] Ashok, J.; Dewangan, N.; Das, S.; Hongmanorom, P.; Wai, M. H.; Tomishige, K.; Kawi, S. Recent progress in the development of catalysts for steam reforming of biomass tar model reaction. *Fuel Process. Technol.* **2020**, *199*, 106252.

[58] Jordan, C. A.; Akay, G. Effect of CaO on tar production and dew point depression during gasification of fuel cane bagasse in a novel downdraft gasifier. *Fuel Process. Technol.* **2013**, *106*, 654–660.

[59] Leibold, H.; Hornung, A.; Seifert, H. HTHP sungas cleaning concept of tso stage biomass gasification for FT synthesis. *Power Technol.* **2008**, *180*, 265–270.

[60] Abdoulmoumine, N.; Adhikari, S.; Kulkarni, A.; Chattanathan, S. A review on biomass gasification syngas cleanup. *Appl. Energy* **2015**, *155*, 294–307.

[61] Richardson, Y.; Blin, J.; Julbe, A. A short overview on purification and conditioning of syngas produced by biomass gasification: Catalytic strategies, process intensification and new concepts. *Prog. Energy Combust. Sci.* **2012**, *38*, 765–781.

[62] Hernández, J. J.; Ballesteros, R.; Aranda, G. Characterization of tars from biomass gasification: Effect of the operating conditions. *Energy* **2013**, *50*, 333–342.

[63] Cortazar, M.; Santamaria, L.; Lopez, G.; Alvarez, J.; Zhang, L.; Wang, R.; Bi, X.; Olazar, M. A comprehensive review of primary strategies for tar removal in biomass gasification. *Energy Convers. Manag.* **2023**, *276*, 116496.

[64] Mesfun, S. A. *Biomass to Liquids (BTL) via Fischer-Tropsch: A Brief Review*; tech. rep.; ETIP (European Technology and Innovation Platform) Bioenergy, 2021 (updated 2022).

[65] Sierra BioFuels Plant & Feedstock Processing Facility. https://www.fulcrum-bioenergy.com/sierra-biofuels (accessed 03/02/2023).

[66] From your trash can to the sky. https://www.fulcrum-bioenergy.com/our-fuel-process (accessed 03/02/2023).

[67] Lee, R. P.; Seidl, L. G.; Huang, Q.; Meyer, B. An analysis of waste gasification and its contribution to China's transition towards carbon neutrality and zero waste cities. *J. Fuel Chem. Technol.* **2021**, *49*, 1057–1076.

[68] JM and bp's innovative FT CANS technology successfully produces product for Fulcrum's Sierra waste-to-fuels plant. https://matthey.com/fulcrum-sierra-23 (accessed 03/02/2023).

[69] Oxygen Reforming of Tar and Methane in Biomass-Derived Syngas. https://www.lindeus.com/-/media/corporate/praxairus/documents/reports-papers-case-studies-and-presentations/industries/metal-production/oxygen-based-reforming-technology-for-renewable-energy.pdf?la=en (accessed 07/02/2023).

[70] Centerpoint BioFuels Plant. https://www.fulcrum-bioenergy.com/centerpoint-biofuels (accessed 03/02/2023).

[71] Trinity Fuels Plant. https://www.fulcrum-bioenergy.com/trinity-fuels-plant (accessed 03/02/2023).

[72] Fulcrum NorthPoint. https://www.fulcrum-bioenergy.com/northpoint (accessed 03/02/2023).

[73] Transforming waste into sustainable advanced biofuels. https://www.altalto.com/ (accessed 03/02/2023).

[74] Process enabling technology. https://www.velocys.com/insights/3207/ (accessed 03/02/2023).

[75] BioTfueL: developing Second-Generation Biofuels. https://totalenergies.com/energy-expertise/projects/bioenergies/biotfuel-converting-plant-wastes-into-fuel (accessed 06/02/2023).

[76] Advanced Biofuels. https://www.thyssenkrupp-uhde.com/en/products-and-technologies/hydrogen-and-gas-technologies/gasification/advanced-biofuels (accessed 06/02/2023).

[77] Uhde® Entrained-Flow Gasification With Direct Quench (PDQ). https://www.thyssenkrupp-uhde.com/en/products-and-technologies/hydrogen-and-gas-technologies/gasification/pdq (accessed 06/02/2023).

[78] Bayou Fuels. https://www.bayoufuels.com/ (accessed 07/02/2023).

[79] Bayou Fuels. https://www.velocys.com/projects/bayou-fuels/ (accessed 07/02/2023).

[80] Red Rock Biofuels, Frontline BioEnergy Successfully Gasify Residual Woody Biomass Into Syngas for Production of Sustainable Aviation Fuel. https://www.businesswire.com/news/home/20220818005417/en/Red-Rock-Biofuels-Frontline-BioEnergy-Successfully-Gasify-Residual-Woody-Biomass-Into-Syngas-for-Production-of-Sustainable-Aviation-Fuel (accessed 07/02/2023).

[81] Gasification Technologies. https://frontlinebioenergy.com/gasification-and-gas-cleaning-technologies/#gas_cleaning (accessed 07/02/2023).

[82] Achieved the flight using sustainable aviation fuel (SAF) made from woody biomass. https://www.toyo-eng.com/jp/en/company/news/?n=584 (accessed 06/02/2023).

[83] Mitsubishi Power to Participate in a Joint Study for the Establishment of a Commercial-scale SAF Production Technology and the Creation of a Supply Chain: Entrained Bed Gasification Technology will Contribute to Decarbonization in Aviation Industry. https://power.mhi.com/news/210830.html (accessed 06/02/2023).

[84] COMSYN Technology. https://www.comsynproject.eu/technology/ (accessed 09/02/2024).

[85] Asadullah, M. Biomass gasification gas cleaning for downstream applications: A comparative review. *Renew. Sustain. Energy Rev.* **2014**, *40*, 118–132.

[86] Woolcock, P. J.; Brown, R. C. A review of cleaning technologies for biomass-derived syngas. *Biomass Bioenergy* **2013**, *52*, 54–84.

[87] Prabhansu, P.; Karmakar, M. K.; Chandra, P.; Chatterjee, P. K. A review on the fuel gas cleaning technologies in gasification process. *J. Environ. Chem. Eng.* **2015**, *3*, 689–702.

[88] Pal, D. B.; Chand, R.; Upadhyay, S. N.; Mishra, P. K. Performance of water gas shift reaction catalysts: A review. *Renew. Sustain. Energy Rev.* **2018**, *93*, 549–565.

[89] Ashok, J.; Wai, M. H.; Kawi, S. Nickel-based Catalysts for High-temperature Water Gas Shift Reaction - Methane Suppression. *ChemCatChem* **2018**, *10*, 3927–3942.

[90] Haryanto, A.; Fernando, S.; Adhikari, S. Ultrahigh temperature water gas shift catalysts to increase hydrogen yield from biomass gasification. *Catal. Today* **2007**, *129*, 269–274.

[91] Chein, R.-Y.; Fang, C.-M.; Chyou, Y.-P.; Chang, S.-H. Effect of Catalyst Support on Water-Gas Shift Reaction at Ultrahigh Temperatures Using Syngas. *Chem. Eng. Technol.* **2017**, *41*, 1390–1397.

[92] Zhang, Z.; Liu, L.; Shen, B.; Wu, C. Preparation, modification and development of Ni-based catalysts for catalytic reforming of tar produced from biomass gasification. *Renew. Sustain. Energy Rev.* **2018**, *94*, 1086–1109.

[93] Yung, M. M.; Jablonski, W. S.; Magrini-Bair, K. A. Review of Catalytic Conditioning of Biomass-Derived Syngas. *Energy Fuels* **2009**, *23*, 1874–1887.

[94] Horn, R.; Schlögl, R. Methane Activation by Heterogeneous Catalysis. *Catal. Lett.* **2015**, *145*, 23–39.

[95] Jones, G.; Jakoben, J. G.; Shim, S. S.; Kleis, J.; Andersson, M. P.; Rossmeisl, J.; Abild-Pedersen, F.; Bligaard, T.; Helveg, S.; Hinnemann, B.; Rostrup-Nielsen, J. R.; Chorkendorff, I.; Sehested, J.; Nørskov, J. K. First principles calculations and experimental insight into methane steam reforming over transition metal catalysts. *J. Catal.* **2008**, *259*, 147–160.

[96] Sehested, J. Four challenges for nickel steam-reforming catalysts. *Catal. Today* **2006**, *111*, 103–110.

[97] Basile, F.; Albertazzi, S.; Barbera, D.; Benito, P.; Einvall, J.; Brandin, J.; Fornasari, G.; Trifirò, F.; Vaccari, A. Steam reforming of hot gas from gasified wood types and miscanthus biomass. *Biomass Bioenergy* **2011**, *35*, 116–122.

[98] Albertazzi, S.; Basile, F.; Barbera, D.; Benito, P.; Brandin, J.; Einvall, J.; Fornasari, G.; Trifirò, F.; Vaccari, A. Deactivation of a Ni-Based Reforming Catalyst During the Upgrading of the Producer Gas, from Simulated to Real Conditions. *Top. Catal.* **2011**, *54*, 746–754.

[99] Gao, N.; Salisu, J.; Quan, C.; Williams, P. Modified nickel-based catalysts for improved steam reforming of biomass tar: A critical review. *Renew. Sustain. Energy Rev.* **2021**, *145*, 111023.

[100] Ochoa, A.; Bilbao, J.; Gayubo, A. G.; P., C. Coke formation and deactivation during catalytic reforming of biomass and waste pyrolysis products: A review. *Renew. Sustain. Energy Rev.* **2020**, *119*, 109600.

[101] Leung, S. L.; Wei, J.; Holstein, W. L.; Avalos-Borja, M.; Iglesia, E. Dynamics and Mechanism of Carbon Filament Formation during Methane Reforming on Supported Nickel Clusters. *J. Phys. Chem. C* **2020**, *124*, 20143–20160.

[102] Montero, C.; Ochoa, A.; Castaño, P.; Bilbao, J.; Gayubo, A. G. Monitoring $Ni^0$ and coke evolution during the deactivation of a $Ni/La_2O_3$-$\alpha Al_2O_3$ catalyst in ethanol steam reforming in a fluidized bed. *J. Catal.* **2015**, *331*, 181–192.

[103] Wang, L.; Li, D.; Koike, M.; Watanabe, H.; Xu, Y.; Nakagawa, Y.; Tomishige, K. Catalytic performance and characterization of Ni–Co catalysts for the steam reforming of biomass tar to synthesis gas. *Fuel* **2013**, *112*, 654–661.

[104] Gao, X.; Ashok, J.; Kawi, S.; Yang, N. Steam reforming of toluene as model compound of biomass tar over $Ni\text{-}Co/La_2O_3$ nano-catalysts: Synergy of Ni and Co. *Int. J. Hydrog. Energy* **2021**, *46*, 30926–30936.

[105] Nabgan, W.; Abdullah, T. A. T.; Mat, R.; Nabgan, B.; Gambo, Y.; Triwahyono, S. Influence of Ni to Co ratio supported on $ZrO_2$ catalysts in phenol steam reforming for hydrogen production. *Int. J. Hydrog. Energy* **2016**, *41*, 22922–22931.

[106] Li, D.; Wang, L.; Koike, M.; Tomishige, K. Development of Ni- and Co-based Alloy Catalysts for Steam Reforming of Biomass Tar. *J. Jpn. Petrol. Inst.* **2013**, *56*, 253–266.

[107] Dębek, R.; Motak, M.; Grzybek, T.; Galvez, M. E.; Costa, P. D. A Short Review on the Catalytic Activity of Hydrotalcite-Derived Materials for Dry Reforming of Methane. *Catalysts* **2017**, *7*, 32.

[108] He, L.; Berntsen, H.; Chen, D. Approaching Sustainable$H_2$ Production: Sorption Enhanced Steam Reforming of Ethanol. *J. Phys. Chem. A* **2010**, *114*, 3834–3844.

[109] Shejale, A. D.; Yadav, G. D. Cu promoted Ni-Co/hydrotalcite catalyst for improved hydrogen production in comparison with several modified Ni-based catalysts via steam reforming of ethanol. *Int. J. Hydrog. Energy* **2017**, *42*, 11321–11332.

[110] Muñoz, M.; Moreno, S.; Molina, R. Synthesis of Ce and Pr-promoted Ni and Co catalysts from hydrotalcite type precursors by reconstruction method. *Int. J. Hydrog. Energy* **2012**, *37*, 18827–18842.

[111] Muñoz, M.; Moreno, S.; Molina, R. The effect of the absence of Ni, Co and Ni-Co catalyst pretreatment on catalytic activity for hydrogen production via oxidative steam reforming of ethanol. *Int. J. Hydrog. Energy* **2014**, *39*, 10074–10089.

[112] De Souza, G.; Ávila, V. C.; Marcílio, N. R.; Perez-Lopes, O. W. Synthesis gas production by steam reforming of ethanol over M-Ni-Al hydrotalcite-type catalysts; M = Mg, Zn, Mo, Co. *Procedia Eng.* **2012**, *42*, 1805–1815.

[113] He, L.; Parra, J. M. S.; Blekkan, E. A.; Chen, D. Towards efficient hydrogen production from glycerol by sorption enhanced steam reforming. *Energy Environ. Sci.* **2010**, *3*, 1046–1056.

[114] Noor, T.; Gil, M. V.; Chen, D. Production of fuel-cell grade hydrogen by sorption enhanced water gas shift reaction using Pd/Ni-Co catalysts. *Appl. Catal. B: Environ.* **2014**, *150-151*, 585–595.

[115] Ghungrud, S. A.; Dewoolkar, K. D.; Vaidya, P. D. Cerium-promoted bi-functional hybrid materials made of Ni, Co and hydrotalcite for sorption-enhanced steam methane reforming (SESMR). *Int. J. Hydrog. Energy* **2019**, *44*, 694–706.

[116] Duan, X.; Pan, J.; Yang, X.; Wan, C.; Lin, X.; Li, D.; Jiang, L. Nickel–cobalt bimetallic catalysts prepared from hydrotalcite-like compounds for dry reforming of methane. *Int. J. Hydrog. Energy* **2022**, *47*, 24358–24373.

[117] Ren, J.; Lei, H.; Mebrahtu, C.; Zeng, F.; Zheng, X.; Pei, G.; Zhang, W.; Wang, Z. Ni-based hydrotalcite-derived catalysts for enhanced $CO_2$ methanation: Thermal tuning of the metal-support interaction. *Appl. Catal. B: Environ.* **2024**, *340*, 123245.

[118] Li, D.; Nakagawa, Y.; Tomishige, K. Methane reforming to synthesis gas over Ni catalysts modified with noble metals. *Appl. Catal. A: Gen.* **2011**, *408*, 1–24.

[119] Chaiprasert, P.; Vitidsant, T. Effects of promoters on biomass gasification using nickel/dolomite catalyst. *Korean J. Chem. Eng.* **2009**, *26*, 1545–1549.

[120] Nishikawa, J.; Nakamura, K.; Asadullah, M.; Miyazawa, T.; Kunimori, K.; Tomishige, K. Catalytic performance of $Ni/CeO_2/Al_2O_3$ modified with noble metals in steam gasification of biomass. *Catal. Today* **2008**, *131*, 146–155.

[121] Gil, M. V.; Rout, K. R.; Chen, D. Production of high pressure pure H2 by pressure swing sorption enhanced steam reforming (PS-SESR) of byproducts in biorefinery. *Appl. Energy* **2018**, *222*, 595–607.

[122] Miyata, T.; Li, D.; Shiraga, M.; Shishido, T.; Oumi, Y.; Sano, T.; Takehira, K. Promoting effect of Rh, Pd and Pt noble metals to the Ni/Mg (Al)O catalysts for the DSS-like operation in $CH_4$ steam reforming. *Appl. Catal. A: Gen.* **2006**, *310*, 97–104.

[123] Li, D.; Shishido, T.; Oumi, Y.; Sano, T.; Takehira, K. Self-activation and self-regenerative activity of trace Rh-doped Ni/Mg(Al)O catalysts in steam reforming of methane. *Appl. Catal. A: Gen.* **2007**, *332*, 98–109.

[124] Li, D.; Nishida, K.; Zhan, Y.; Shishido, T.; Oumi, Y.; Sano, T.; Takehira, K. Superior catalytic behavior of trace Pt-doped Ni/Mg(Al)O in methane reforming under daily start-up and shut-down operation. *Appl. Catal. A: Gen.* **2008**, *350*, 225–236.

[125] Au, C.-T.; Ng, C.-F.; Liao, M.-S. Methane Dissociation and Syngas Formation on Ru, Os, Rh, Ir, Pd, Pt, Cu, Ag, and Au: A Theoretical Study. *J. Catal.* **1999**, *185*, 12–22.

[126] Rives, V. Characterisation of layered double hydroxides and their decomposition products. *Mater. Chem. Phys.* **2002**, *75*, 19–25.

[127] Cavani, F.; Trifirb, F.; Vaccari, A. Hydrotalcite-Type Anionic Clays: Preparation, Properties and Applications. *Catal. Today* **1991**, *11*, 173–301.

[128] He, K.; Chen, N.; Wang, C.; Wei, L.; Chen, J. Method for Determining Crystal Grain Size by X-Ray Diffraction. *Cryst. Res. Technol.* **2018**, *53*, 1700157.

[129] Brunauer, S.; Emmett, P. H.; Teller, E. Adsorption of Gases in Multimolecular Layers. *J. Am. Chem. Soc.* **1938**, *60*, 309–319.

[130] Barrett, E. P.; Joyner, L. G.; Halenda, P. P. The Determination of Pore Volume and Area Distributions in Porous Substances. I. Computations from Nitrogen Isotherms. *J. Am. Chem. Soc.* **1951**, *73*, 373–380.

[131] Chorkendorff, I.; Niemantsverdriet, J. W., *Concepts of Modern Catalysis and Kinetics - Third, Completely Revised and Enlarged Edition*; Wiley-VCH: Weinheim, 2017.

[132] Bergeret, G.; Gallezot, P. In *Handbook of Heterogeneous Catalysis*, Ertl, G., Knözinger, H., Weitkamp, J., Eds.; Wiley-VCH: Weinheim, 2008; Chapter 3.1.2, pp 738–765.

[133] Madsen, K. Ø. Catalytic Steam Reforming of Hydrocarbon Impurities from Biomass Gasification, Master's thesis, Norwegian University of Science and Technology, 2021.

[134] Wei, J.; Iglesia, E. Isotopic and kinetic assessment of the mechanism of reactions of $CH_4$ with $CO_2$ or $H_2O$ to form synthesis gas and carbon on nickel catalysts. *J. Catal.* **2004**, *224*, 370–383.

[135] Maestri, M.; Tronconi, E.; Berger, R. J.; Kapteijn, F.; Moulijn, J. A. *EUROKIN, Overview of requirements for measurement of intrinsic kinetics in and overview of correlations for characteristics of the G-S and L-S fixed-bed reactor*; tech. rep.; Politecnico di Milano and Delft University of Technology, 2018.

[136] Chu, C. F.; Ng, K. M. Flow in packed tubes with a small tube to particle diameter ratio. *AIChE J.* **1989**, *35*, 148–158.

[137] Mears, D. E. Role of axial dispersion in trickle-flow laboratory reactors. *Chem. Eng. Sci.* **1971**, *26*, 1361–1366.

[138] Gierman, H. Design of laboratory hydrotreating reactors: Scaling Down of Trickle-flow Reactors. *Appl. Catal.* **1988**, *43*, 277–286.

[139] Wakao, N.; Kaguei, S.; Funazkri, T. Effect of fluid dispersion coefficients on particle-to-fluid heat-transfer coefficients in packed-beds: Correlation of Nusselt numbers. *Chem. Eng. Sci.* **1979**, *34*, 325–336.

[140] Punčochář, M.; Drahoš, J. The tortuosity concept in fixed and fluidized bed. *Chem. Eng. Sci.* **1993**, *48*, 2173–2175.

[141] Perry, R. H.; Green, D. W., *Perry's Chemical Engineers' Handbook*, 7th; McGraw-Hill: New York, 1997.

[142] Mears, D. E. Diagnostic criteria for heat transport limitations in fixed bed reactors. *J. Catal.* **1971**, *20*, 121–131.

[143] Wilke, C. R. A Viscosity Equation for Gas Mixtures. *J. Chem. Phys.* **1950**, *18*, 517–519.

[144] Satterfield, C. N., *Mass transfer in heterogeneous catalysis*; MIT Press: Cambridge, Massachusetts, 1970.

[145] Froment, G. F.; Bischoff, K., *Chemical Reactor Analysis and Design*; John Wiley  Sons: New York, 1990.

[146] Nikolla, E.; Schwank, J.; Linic, S. Comparative study of the kinetics of methane steam reforming on supported Ni and Sn/Ni alloy catalysts: The impact of the formation of Ni alloy on chemistry. *J. Catal.* **2009**, *263*, 220–227.

[147] Zeppieri, M.; Villa, P. L.; Verdone, N.; Scarsella, M.; De Filippis, P. Kinetic of methane steam reforming reaction over nickel- and rhodium-based catalysts. *Appl. Catal. A: Gen.* **2010**, *387*, 147–154.

[148] Wang, Y.; Wang, H.; Dam, A. H.; Xiao, L.; Qi, Y.; Niu, J.; Yang, J.; Zhu, Y.-A.; Holmen, A.; Chen, D. Understanding effects of Ni particle size on steam methane reforming activity by combined experimental and theoretical analysis. *Catal. Today* **2020**, *355*, 139–147.

[149] Wan, C.; Song, K.; Pan, J.; Huang, M.; Luo, R.; Li, D.; Jiang, L. Ni-Fe/Mg (Al)O alloy catalyst for carbon dioxide reforming of methane: Influence of reduction temperature and Ni–Fe alloying on coking. *Int. J. Hydrog. Energy* **2020**, *45*, 33574–33585.

[150] Siang, T. J.; Singh, S.; Omoregbe, O.; Bach, L. G.; Phuc, N. H. H.; Vo, D.-V. N. Hydrogen production from $CH_4$ dry reforming over bimetallic Ni–Co/Al2O3 catalyst. *J. Energy Inst.* **2018**, *91*, 683–694.

[151] Zhang, J.; Wang, H.; Dalai, A. K. Kinetic Studies of Carbon Dioxide Reforming of Methane over Ni-Co/Al-Mg-O Bimetallic Catalyst. *Ind. Eng. Chem. Res.* **2009**, *48*, 677–684.

[152] Liao, X.; Gerdts, R.; Parker, S. F.; Chi, L.; Zhao, Y.; Hill, M.; Guo, J.; Jones, M. O.; Jiang, Z. An in-depth understanding of the bimetallic effects and coked carbon species on an active bimetallic Ni(Co)/$Al_2O_3$ dry reforming catalyst. *Phys. Chem. Chem. Phys.* **2016**, *18*, 17311–17319.

# Appendix A

## Paper I: Effects of Ni-Co Ratio on Deactivation and Coke Formation in Steam Reforming of Hydrocarbon Impurities from Biomass Gasification with Ni-Co/Mg(Al)O Catalysts

Ask Lysne, Kristin Ø. Madsen, Jibin Antony, Kumar R. Rout and Edd A. Blekkan

*Chem. Eng. Trans.*, **2022**, 92, 37-42.

CHEMICAL ENGINEERING TRANSACTIONS
VOL. 92, 2022
A publication of AIDIC
The Italian Association of Chemical Engineering
Online at www.cetjournal.it
Guest Editors: Rubens Maciel Filho, Eliseo Ranzi, Leonardo Tognotti

**ISBN** 978-88-95608-90-7; **ISSN** 2283-9216
DOI: 10.3303/CET2292007

# Effects of Ni-Co Ratio on Deactivation and Coke Formation in Steam Reforming of Hydrocarbon Impurities from Biomass Gasification with Ni-Co/Mg(Al)O Catalysts

Ask Lysne, Kristin Ø. Madsen, Jibin Antony, Kumar R. Rout, Edd A. Blekkan*

Department of Chemical Engineering, Norwegian University of Science and Technology
edd.a.blekkan@ntnu.no

Ni-Co/Mg(Al)O catalysts with different Ni-Co ratios (40-0, 30-10, 20-20, 10-30 and 0-40 wt%) have been tested for steam reforming of hydrocarbon impurities in a model biomass gasification syngas at relevant operating conditions. Effects of tar model (toluene) presence on catalyst deactivation and coke formation were studied. The fresh samples were characterized by ICP-MS, XRD, TPR, $N_2$-physisorption and $H_2$-chemisorption. The coke formation was studied by TGA-TPO, Raman spectroscopy and SEM/EDS. Efficient formation of Ni-Co alloy particles was confirmed by XRD and SEM/EDS. The Ni-Co/Mg(Al)O system shows high steam reforming activity with complete model tar removal. Simultaneous high-temperature $H_2$/CO ratio adjustment by effective equilibration of the WGS reaction was demonstrated. Initial Co addition was proposed to reduce the formation of strongly deactivating encapsulating coke species by efficient removal of coke precursors at the expense of enhanced carbon filament formation. Lower Ni-Co ratios were shown to effectively reduce deactivation and coke formation at the expense of the higher initial activity of the high Ni-Co ratio system. Restructuring of extensive carbon filament clusters was proposed as an additional route to encapsulating coke species with potential long-term deactivation effects. The Ni-Co ratio was shown to affect the carbon filament formation rates and filament diameter distributions. The effects on coke formation were proposed to depend on complex interactions of metal particle size and Ni-Co alloy ratio. The results contribute to the understanding of the highly attractive resistance towards deactivation by coke formation of Ni-Co catalyst systems.

## 1. Introduction

Renewable aviation fuels can be produced in a biomass-to-liquid process, coupling biomass gasification and Fischer-Tropsch synthesis (Huber et al., 2006). Biomass gasification involves thermal decomposition of biomass feedstocks, forming mainly $H_2$, CO, $CO_2$, $CH_4$ and $H_2O$ (Giuliano et al., 2020). The product gas also contains tar impurities (condensable aromatic hydrocarbons) causing downstream condensation, coking and corrosion issues (Li et al., 2015). Tar elimination has been put forth as the greatest challenge in commercialization of such technologies. Steam reforming is an attractive tar removal approach, increasing process efficiency compared to physical separation and thermal cracking strategies. Li et al. (2015) reviewed the development of catalysts for such applications, calling for further research on bi-metallic Ni-Co systems, targeting low-cost, high-performance alloy catalysts with increased coke formation resistance. Hydrotalcite-based Ni-Co/Mg(Al)O catalysts have to the best of our knowledge never been reported for tar removal at relevant operating conditions. The goal of the present work was to study the effects of Ni-Co ratio on reforming activity and stability of such systems. The coke characterization approach provides further understanding of coke formation dynamics in Ni-Co catalysts.

## 2. Experimental

The catalyst synthesis was based on previous literature (He et al., 2009). All chemicals were acquired from Sigma-Aldrich or VWR Chemicals. Reduced and passivated samples were prepared by reduction at 670 °C for 16 hours in $H_2$ (200 NmL/min) and He (100 NmL/min). The samples were cooled in He (100 NmL/min) and passivation in 1 mol% $O_2$ in $N_2$ (100 NmL/min) for 2 hours.

Paper Received: 11 February 2022; Revised: 12 March 2022; Accepted: 5 May 2022
Please cite this article as: Lysne A., Madsen K.O., Antony J., Rout K.R., Blekkan E.A., 2022, Effects of Ni-Co Ratio on Deactivation and Coke Formation in Steam Reforming of Hydrocarbon Impurities from Biomass Gasification with Ni-Co/Mg(Al)O Catalysts, Chemical Engineering Transactions, 92, 37-42 DOI:10.3303/CET2292007

### 2.1 Catalyst characterization

ICP-MS was performed by SINTEF. The calcined precursors were decomposed in parallel with HCl and $HNO_3$ at 250 °C for 10 minutes in a Milestone UltraWAVE microwave oven and analyzed with an Agilent 8800 Triple Quadrupole ICP-MS equipped with an SPS 4 Autosampler. The samples were diluted in 5% $HNO_3$ and added $^{115}In$ as internal standard. Quantification was performed with respect to standards from Inorganic Ventures. Powder XRD was conducted with a Bruker D8 A25 DaVinci X-ray Diffractometer. TPR was performed with an Altamira BenchCat Hybrid 1000HP. The samples were pre-dried at 200 °C for 30 minutes in Ar (50 NmL/min) and cooled to 50 °C before heating to 900-1000 °C in 7 mol% $H_2$ in Ar (50 NmL/min). $N_2$-physisorption was carried out with a Micromeritics TriStar 3000 Surface Area and Porosity Analyzer. The samples (280 mg) were degassed in vacuum for 1 hour at room temperature and overnight at 100 °C. Adsorption/desorption isotherms were recorded at -196 °C. $H_2$-chemisorption was performed with a Micrometrics ASAP 2020 instrument. The calcined samples (150 mg) were evacuated for 1 hour at 30 °C and reduced in $H_2$ at 670 °C for 16 hours. The system was evacuated for 0.5 hours at 670 °C and 1.5 hours at 35 °C before recording the adsorption isotherms.

### 2.2 Steam reforming experiments

The experimental setup is shown in Figure 1. Reforming experiments were performed with a fixed-bed quartz reactor (6 mm inner diameter) with catalyst samples (10.0 mg, 75-150 µm) diluted with α-$Al_2O_3$ (400.0 mg). Reaction temperatures were measured with a thermocouple in a reactor center heat-pocket in contact with the top of the catalyst bed. All gasses were fed by Bronkhorst MFCs. The model syngas contained 10/35/25/25 mol% $CH_4/H_2/CO/CO_2$ with 5 mol% $N_2$ as internal standard. The steam was provided with a vaporizer consisting of an MFC feeding $H_2O$ through a heating furnace (250 °C, Ar carrier gas) from a pressurized water-tank. All lines downstream of the vaporizer were heated to avoid condensation. The catalysts were reduced in 50 mol% $H_2$ (100 NmL/min) in Ar (100 NmL/min) for 16 hours at 670 °C. The reactant flow was stabilized in a reactor bypass before directing the flow to the catalyst. The syngas flow (400 NmL/min), GHSV (85000 NmL/$g_{cat}$min), pressure (atmospheric) and S/C ratio of 3.0 (molar hydrocarbon basis) were kept constants for all experiments.

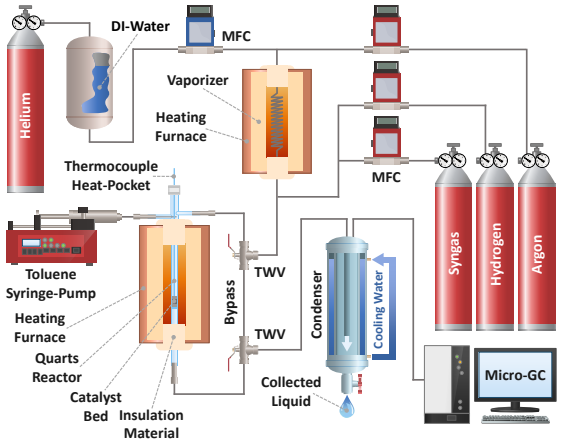


*Figure 1: Simplified experimental setup. Syngas: 400 NmL/min, toluene: 10.0 g/Nm³ (dry syngas basis), GHSV: 85000 NmL/$g_{cat}$min, temperature: 650-800 °C, S/C ratio: 3.0 (molar hydrocarbon basis).*

Initial empty-reactor tests were performed at the same conditions. Initial SMR temperature screening was carried out at 650-800 °C. The catalyst stability during SMR operation was studied for 8 hours at 700 °C. The stability during hydrocarbon steam reforming in a tar model environment was studied by injection of 10.0 g/Nm³ toluene (dry syngas basis) into the reactor with an NE-1000 syringe-pump (50 mL SS syringe, KD Scientific). Condensable liquids were removed before gas composition analysis ($CH_4$, $H_2$, CO, $CO_2$ and $N_2$) with an Agilent 490 Micro-GC system (CP-COX column). Spent catalysts were cooled to room temperature in Ar (100 NmL/min) and isolated from the dilution material by magnetic separation. Condenser samples were extracted (n-pentane) and analyzed with an Agilent 7820A GC-FID system (HP-5 column). Peak identification was achieved with an Agilent 7820A GC-MS system. All applied gases were supplied by Linde/AGA. Equilibrium compositions were calculated in Aspen Plus V9 (Peng-Robinson cubic equation of state).

### 2.3 Coke characterization

TGA-TPO was performed with an Linseis STA PT1600 instrument, heating the spent catalysts (5-10 mg) from 150 to 800 °C (5 °C/min) in synthetic air (21 mol% $O_2$ in $N_2$, 140 NmL/min) and Ar (60 NmL/min) after 1 hour of pre-drying at 150 °C in Ar (200 NmL/min). The coke combustion was monitored by $CO_2$ formation with an MS detector (m/z = 44). Raman spectroscopy was carried out with a Horiba Jobin Yvon LabRAM HR800 system (633 nm laser). SEM/EDS was performed with an ultra-high resolution Hitachi SU9000 STEM instrument. The spent samples were dispersed in ethanol and drop-casted onto plasma cleaned diced silicon wafers. Elemental mapping was performed with an Oxford Ultim Extreme EDS detector.

## 3. Results and discussion

Initial empty-reactor tests showed negligible SMR and WGS activity within the inaccuracy of the measurements. Ideal plug-flow conditions and elimination of mass-transfer limitations were acquired by preliminary calculations recommended by the EUROKIN project. Initial temperature screening gave linear Arrhenius plots at lower temperatures (650-700 °C) as expected in the kinetic regime. Further tests were conducted at 700 °C to study deactivation of intrinsic kinetics. The $CH_4$ conversion was far from thermodynamic equilibrium in all experiments. The carbon mass balance was 99.0±0.9% for all data, indicating high quality feed and product analysis control.

### 3.1 Catalyst characterization

XRD and TPR results were in accordance with previously reported data (He et al., 2009). Key ICP-MS data is shown in Table 1. The bulk Ni/Co ratios were generally slightly higher than target values. This was in accordance with previous literature relating the effect to restricted integration of Co into the hydrotalcite structure (compared to Ni) due to the larger atomic radius (He et al., 2009).

*Table 1: Key ICP-MS data (average from two samples).*

| Sample | Ni (%) | Co (%) | Mg (%) | Al (%) | Ni/Co ratio (a.u.) |
|---|---|---|---|---|---|
| 40 wt% Ni | 35.5 | - | 38.5 | 26.0 | - |
| 30-10 wt% Ni-Co | 27.4 | 8.9 | 36.1 | 27.6 | 3.08 |
| 20-20 wt% Ni-Co | 18.4 | 17.6 | 37.0 | 27.0 | 1.05 |
| 10-30 wt% Ni-Co | 9.5 | 26.2 | 36.2 | 28.1 | 0.36 |
| 40 wt% Co | - | 34.8 | 38.7 | 26.5 | - |

XRD patterns after reduction and passivation (Figure 2a) showed complete reduction of spinel-type structures leaving only the MgO-like support and metallic Ni and Co. Figure 2b shows an observed shift in d-spacing towards higher values with increasing Co content due to the larger atomic radius.

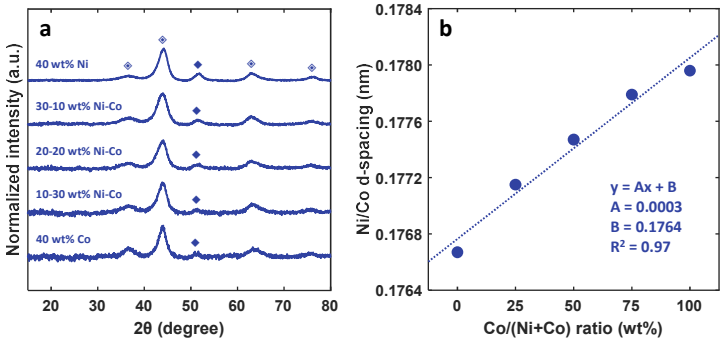


*Figure 2: XRD patterns (a) after reduction and passivation with MgO-like mixed oxide supports (◈) and metallic Ni-Co particles (◆). (b) Shifted Ni-Co crystal plane d-spacing.*

The close to linear relation suggested effective formation of Ni-Co alloy particles. Efficient Ni-Co alloy formation was confirmed by SEM/EDS elemental mapping showing clear co-location of Ni/Co in metal particles. EDS point scans (20 particles) gave Ni/Co ratios of 4.3±0.5, 1.1±0.1 and 0.42±0.04 for the 30-10, 20-20 and 10-30 wt%

Ni-Co samples, somewhat higher than ICP-MS bulk ratios. Key $N_2$-physisorption and $H_2$-chemisorption data is shown in Table 2. The highest BET surface areas and metal dispersions were obtained at higher Ni-Co ratios.

*Table 2: Key $N_2$-physisorption (average from two samples) and $H_2$-chemisorption data.*

| Sample | BET surface area ($m^2/g$) | Metal dispersion (%) | Metal particle diameter (nm) |
|---|---|---|---|
| 40 wt% Ni | 175 | 8.1 | 12.6 |
| 30-10 wt% Ni-Co | 184 | 8.6 | 11.8 |
| 20-20 wt% Ni-Co | 162 | 6.5 | 15.4 |
| 10-30 wt% Ni-Co | 151 | 4.8 | 20.7 |
| 40 wt% Co | 118 | 5.4 | 18.5 |

### 3.2 Catalyst deactivation

Catalyst reforming activity was monitored by $CH_4$ conversion with and without tar model (toluene) presence. Typical conversion profiles are shown in Figure 3a with simple linear decay functions in the pure syngas. Tar model presence gave initial rapid exponential deactivation followed by further linear decay. An expected toluene addition delay (20-30 min) from the tubing between the syringe-pump and the reactor was observed. No toluene or other byproducts were found in the condenser samples. Standard analysis indicated toluene conversions well above 99.5% (equilibrium = 100%). Initial and final (TOS = 8 hours) $CH_4$ conversions are shown in Figure 3b.

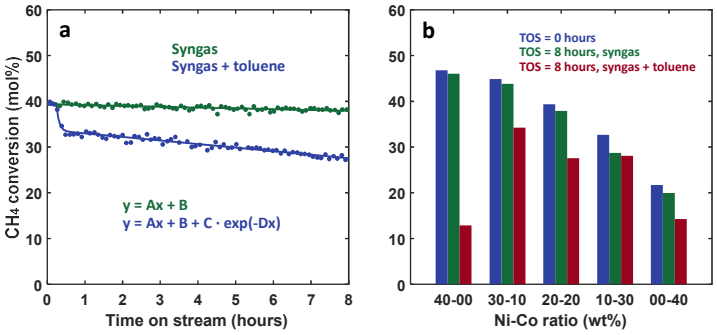


*Figure 3: $CH_4$ conversion profiles (a) in pure syngas and tar model (toluene) environment (20-20 wt% Ni-Co). (b) Initial and final (TOS = 8 hours) $CH_4$ conversion with different Ni-Co ratios.*

The reforming activity was fairly stable for all samples in the pure syngas. Interestingly, the 30-10 wt% Ni-Co and 40 wt% Ni samples showed similar high initial activities, but with considerably reduced deactivation in the bi-metallic system. Figure 3b shows how the final reforming activity of the lower Ni-Co ratio samples is limited by the decreasing initial activity upon Co addition. Similar effluent $H_2$/CO ratios (1.77-1.91) were obtained for all samples throughout the experiments despite the changing $CH_4$ conversion. Such behavior is expected in the case of effective equilibration of the WGS reaction. The $H_2$/CO ratios were close to calculated equilibrium values (1.65-1.75). Only the highly deactivated 40 wt% Ni sample showed some WGS activity loss by a small $H_2$/CO ratio decrease (final value of 1.57) in the tar model environment.

### 3.3 Coke characterization

Figure 4a shows coke amounts and combustion $CO_2$ signals from TGA-TPO after operation in the tar model environment. The Raman spectra for the same samples are shown in Figure 4b. Interestingly, the highest coke amount was found for the 30-10 wt% Ni-Co sample. Such high coke amounts despite a lower overall deactivation can be explained by carbon filament formation without active site blockage. Chen et al. (2005) studied filament growth in Ni catalysts, observing rapid deactivation of smaller metal particle samples. The present work similarly shows rapid deactivation of the 40 wt% Ni catalyst with small metal particles (12.6 nm). The deactivation of smaller particles was explained by a reduced carbon diffusion driving force (bulk diffusion model) increasing carbon surface coverage, carbon polymerization rates and the formation of strongly deactivating encapsulating coke (Chen et al., 2005). This model was in accordance with the high-temperature coke combustion shift observed for the 40 wt% Ni sample. Higher temperature coke combustion is generally associated with a higher

degree of encapsulation since available active metal sites also catalyze combustion reactions. These results suggest that the 30-10 wt% Ni-Co sample forms less encapsulating coke compared to the 40 wt% Ni catalyst. The effect is however proposed to result from effective removal of coke precursors from the particle surface at the expense of enhanced filament growth. The altered coke formation for the two catalysts with similar metal particle size (11.8-12.6 nm), suggested some additional Ni-Co synergy effects beyond metal particle size alone. The lower coke amounts upon further Co addition indicated reduced filament growth despite the metal particle size increase (15.4-20.7 nm). The Raman spectra showed the expected D and G bands (1350 and 1580 $cm^{-1}$) attributed to the presence of disordered/defective carbon and ordered graphitic structures respectively. No detectable coke was found by TGA-TPO or Raman spectroscopy for any samples after tar free operation.

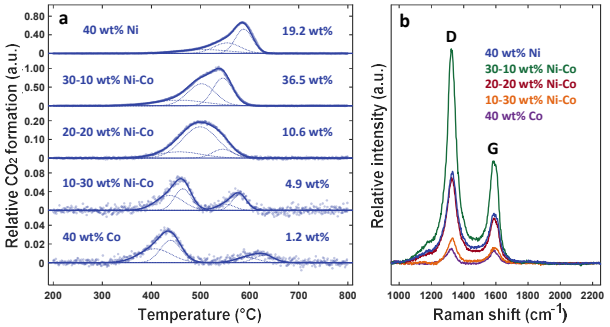


*Figure 4: (a) $CO_2$ formation (coke combustion) during TGA-TPO after operation in tar model (toluene) presence (note individual y-axis scaling). Estimated coke amounts indicated. (b) Raman spectra for the same samples.*

Figure 5a shows regions with encapsulating coke particularly prominent in the 40 wt% Ni sample. Figure 5b shows regions with less encapsulation frequently observed at lower Ni-Co ratios. This suggested the highly encapsulating coke species to be less developed in these samples in accordance with TGA-TPO results. Figure 5c shows carbon filament clusters found in all samples, confirming the previous indications of filament formation. Figure 5d shows what appeared to be fused filament clusters. Such filament aging is described in previous literature with potential long-term blocking of catalyst pores and metal sites (Montero et al., 2015). Figure 5e shows normalized filament diameter distributions (1000 filaments). Interestingly, the 30-10 and 20-20 wt% Ni-Co showed shifted filament distributions towards larger diameters (10-60 nm). These samples also showed considerably higher linear decay components (A = 0.0130 and 0.0134) in the tar model environment compared to the other catalysts (A = 0.0015 to 0.0057). It is reasonable to believe that the broader filament diameter selectivity can be related to enhanced filament growth and the TGA-TPO peaks around 500 °C with the highest intensities in the same samples. The higher linear decay is proposed to result from filament restructuring mechanisms. Further Co addition limits filament formation to smaller diameters (5-35 nm). It is reasonable to believe that the lower coke amounts at low Ni-Co ratios can be related to a reduced filament growth following the shifted diameter selectivity. The filament diameter is generally considered to reflect the size of the metal particle from which the filament grows. Figure 5e shows the metal particle size distribution (1000 particles) for the 20-20 wt% Ni-Co sample, with the filament distribution covering the lower particle size range. The selectivity towards smaller particles with higher surface area and density of steps is not unexpected. In a bulk diffusion model the shorter diffusion length and higher diffusion flux area of smaller particles is also expected to enhance filament growth. However, Chen et al. (2005) showed that smaller particles give higher filament saturation concentrations, reducing the bulk diffusion driving force. The net particle size effect on filament growth rates will depend on the compensation of these factors. The enhanced filament formation in the 30-10 wt% Ni-Co sample compared to the 40 wt% Ni catalyst with similar metal particle size suggests the net particle size effect to be altered upon Co addition. Steady-state filament growth rates are commonly considered to reflect carbon bulk diffusion rates. The lower carbon diffusion coefficient in Co ($8.17 \cdot 10^{-14}$ $m^2/s$) compared to Ni ($3.03 \cdot 10^{-13}$ $m^2/s$) at 700 °C (Yokoyama et al., 1998) could hereby explain the reduced filament formation at lower Ni-Co ratios. The low formation of encapsulating coke in these samples can be explained by enhanced coke gasification, or simply by lower carbon surface concentrations due to the lower reforming activity.

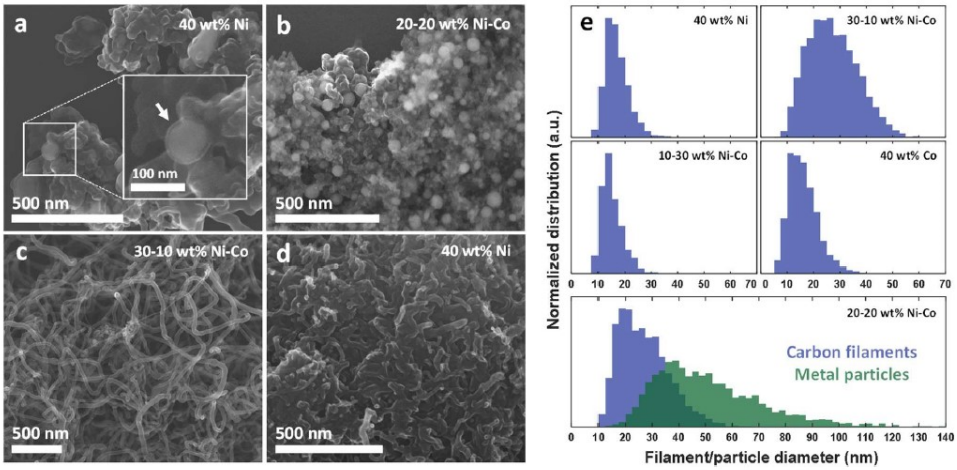


*Figure 5: SEM images of (a) encapsulating coke, (b) less encapsulated regions, (c) carbon filament clusters and (d) fused filaments. (e) Normalized filament/metal particle diameter distributions.*

## 4. Conclusions

The Co addition effectively reduced the formation of strongly deactivating encapsulating coke species compared to the mono-metallic Ni catalyst. The effect was attributed to efficient removal of surface carbon at the expense of enhanced carbon filament formation. The performance of low Ni-Co ratio catalysts was limited by the lower initial reforming activity. Filament growth and diameter selectivities were proposed to depend on complex metal particle size and Ni-Co ratio interactions. These results contribute to the understanding of the highly attractive resistance towards deactivation by coke formation of Ni-Co reforming catalysts.

**Acknowledgments**

The project is funded by the Norwegian Research Council (no. 257622) through the Centre for Environment-friendly Energy Research (FME) Bio4Fuels. The Norwegian Research Council is also acknowledged for the support to the Norwegian Micro- and Nano-Fabrication Facility, NorFab (no. 295864).

**References**

Chen D., Christensen K.O., Ochoa-Fernández E., Yu Z., Tøtdal B., Latorre N., Monzón A., Holmen A., 2005, Synthesis of carbon nanofibers: effects of Ni crystal size during methane decomposition, Journal of Catalysis, 229, 82-96.

Giuliano A., Freda C., Catizzone, E., 2020, Techno-Economic Assessment of Bio-Syngas Production for Methanol Synthesis: A Focus on the Water-Gas Shift and Carbon Capture Sections, Bioengineering, 7, 70.

He L., Berntsen H., Ochoa-Fernández E., Walmsley J.C., Blekkan E.A., Chen D., 2009, Co-Ni Catalysts Derived from Hydrotalcite-Like Materials for Hydrogen Production by Ethanol Steam Reforming, Topics in Catalysis, 52, 206-217.

Huber G.W., Iborra S., Corma A., 2006, Synthesis of Transportation Fuels from Biomass: Chemistry, Catalysts, and Engineering, Chemical Reviews, 106, 4044-4098.

Li D., Tamura M., Nakagawa Y., Tomishige K., 2015, Metal catalysts for steam reforming of tar derived from the gasification of lignocellulosic biomass, Bioresource Technology, 178, 53-64.

Montero C., Ochoa A., Castaño P., Bilbao J., Gayubo A.G., 2015, Monitoring $Ni^0$ and coke evolution during the deactivation of a Ni/$La_2O_3$-α$Al_2O_3$ catalyst in ethanol steam reforming in a fluidized bed, Journal of Catalysis, 331, 181-192.

Yokoyama H., Numakura H., Koiwa M., 1998, The Solubility and Diffusion of Carbon in Palladium, Acta Materialia, 46, 2823-2830.

# Appendix B

## Paper II: Steam reforming of bio-syngas tar impurities with Ni-Co/Mg(Al)O catalysts - Operating parameter effects

Ask Lysne, Ida Saxrud, Kristin Ø. Madsen and Edd A. Blekkan

Manuscript submitted to *Appl. Catal. B: Environ.* (2024).

# Appendix C

## Paper III: Nobel metal (Pt, Pd and Rh) promoted Ni-Co/Mg(Al)O catalysts for steam reforming of biomass gasification tar impurities

Ask Lysne, Ida Saxrud, Rémi L. G. Snidaro and Edd A. Blekkan

Manuscript submitted to *J. Catal.* (2024).

# Appendix D

## Paper IV: Continuous coke management with Ni and Ni-Co catalysts for bio-syngas tar steam reforming - The Switch-SRCG unit

Ask Lysne and Edd A. Blekkan

Manuscript submitted to *Catal. Commun.* (2024).

This paper is awaiting publication and is not included in NTNU Open

ISBN 978-82-326-7750-4 (printed ver.)
ISBN 978-82-326-7749-8 (electronic ver.)
ISSN 1503-8181 (printed ver.)
ISSN 2703-8084 (online ver.)



NTNU
Norwegian University of
Science and Technology